The adaptive time-dependent density-matrix renormalization-group method: development and applications

Von der Fakultät für Mathematik, Informatik und Naturwissenschaften
der Rheinisch-Westfälischen Technischen Hochschule Aachen
zur Erlangung des akademischen Grades
einer Doktorin der Naturwissenschaften genehmigte Dissertation

vorgelegt von
Diplom-Physikerin
Corinna Kollath B.Sc.
aus Stirling (Großbritannien)

Berichter: Universitätsprofessor Dr. Ulrich Schollwöck
Universitätsprofessor Dr. Walter Hofstetter

Tag der mündlichen Prüfung: 4. Juli 2005

Diese Dissertation ist auf den Internetseiten
der Hochschulbibliothek online verfügbar.

Contents

Zusammenfassung **7**

1. Introduction **11**

2. The adaptive time-dependent density-matrix renormalization-group method **14**
2.1. Can DMRG be applied to time-dependent phenomena? 14
2.2. 'Original' density-matrix renormalization-group method 16
2.2.1. Density-matrix projection 17
2.2.2. DMRG algorithm 20
2.3. Simulation of time-dependent quantum phenomena using DMRG 23
2.4. Matrix-product states 29
2.5. TEBD simulation algorithm 31
2.6. DMRG and matrix-product states 36
2.7. Adaptive t-DMRG 39
2.8. Case study: time-dependent Bose-Hubbard model 40
2.9. Sources of error 44
2.10. Conclusion 45

3. Ultracold atoms in optical lattices **46**
3.1. From Bose-Einstein condensation to strongly interacting Bose gases 46
3.2. Theoretical description: Bose-Hubbard model 48
3.3. Quantum phase transition in homogeneous systems 51
3.3.1. Limit of weak interaction: superfluid phase 51
3.3.2. Limit of strong interaction: Mott-insulating phase 52
3.3.3. Quantum phase transitions 52
3.3.4. Gutzwiller approximation 54
3.4. Coexistence of phases in a trapping potential 56
3.5. Modifications to the finite DMRG treating confinement potentials 57
3.6. One-particle density-matrix 58
3.6.1. Scaled one-particle density-matrix 59
3.6.2. Comparison to the hydrodynamical approach 61
3.7. Connection to experiment 64
3.7.1. Interference pattern 64
3.7.2. Comparison to experiment 68
3.8. Conclusion 69

4. Evolution of density wave packets in ultracold bosons **71**
4.1. Perturbations: experiments and theoretical descriptions 71
4.2. Theoretical description of the density perturbation 72
4.3. Preparation of the density perturbation 73
4.4. Analytical approximations 73
4.5. Evolution of the wave packet 74
4.6. Decay of the amplitude 77
4.7. Sound velocity 77
4.8. Self-steepening 82
4.9. Experimental observation 82
4.10. Conclusion 85

5. Spin-charge separation in cold Fermi gases: a real time analysis **87**
5.1. Fascinating physics in one dimension 87
5.2. Hubbard model 88
5.3. Quantum phase diagram 88
5.4. Spin-charge separation 89
5.5. Preparation of the perturbation 90
5.6. Spin-charge separation: beyond small perturbations 91
5.7. Proposed experimental realization 95
5.8. Experimental parameters 97
5.9. Conclusions 98

6. Transport in spin-$1/2$ chains **99**
6.1. Introduction 99
6.2. Model and initial state 99
6.3. Accuracy of the adaptive t-DMRG 102
6.3.1. Error analysis for the XX-model 102
6.3.2. Optimal choice of DMRG parameters 108
6.4. Long-time properties of the time evolution 110
6.5. Conclusions 119

7. Conclusion and outlook **120**

A. Higher order Suzuki-Trotter decompositions **123**

B. Ultracold atoms confined in optical lattices **125**
B.1. Interaction of neutral atoms with light fields 125
B.2. Optical lattices 126
B.3. Theoretical description of bosons in optical lattices 128
B.3.1. Influence of periodic structures 128
B.3.2. Bose-Hubbard model 128

Bibliography **133**

Acknowledgement **145**

List of publications related to the thesis **147**

Curriculum vitae **149**

Zusammenfassung

Die theoretische Beschreibung zeitabhängiger Phänomene stellt nach wie vor eine große Herausforderung dar, zumal in den letzten Jahren deutliche Fortschritte bei Experimenten zur Nichtgleichgewichtsphysik erzielt wurden. In dieser Arbeit wird die numerische Methode der adaptiven zeitabhängigen Dichtematrix Renormalisierungsgruppe (adaptive t-DMRG) entwickelt, die uns die Möglichkeit eröffnet, zeitabhängige Phänomene in stark korrelierten eindimensionalen Quantensystemen zu untersuchen. Die neue Methode ist eine Zusammenführung der Ideen des 'finite-system DMRG' Algorithmus und des 'time evolving block-decimation' Algorithmus (TEBD). Sie beruht auf der Reduktion des Hilbertraumes auf geeignet gewählte Unterräume, die zur Beschreibung der zeitlichen Entwicklung schrittweise adaptiert werden.
Wir zeigen die Anwendbarkeit, Effizienz und Genauigkeit der adaptiven t-DMRG, indem wir die zeitliche Entwicklung drei verschiedener Systeme diskutieren: ein bosonisches, ein fermionisches und ein Spin-System. Wir benutzen die Existenz einer exakten Lösung für das XX-Modell einer Spin 1/2-Kette, um eine detaillierte Fehleranalyse durchzuführen. Der gesamte Fehler setzt sich aus zwei Beiträgen, dem 'truncation' Fehler und dem Suzuki-Trotter-Fehler zusammen. Die Anzahl der Zustände und die Größe des Suzuki-Trotter-Zeitschritts geben eine gute Kontrolle über die Genauigkeit der Methode. Für typische Werte dieser Parameter finden wir, daß der Suzuki-Trotter-Fehler bei kleinen Zeiten dominiert, wohingegen für lange Zeiten der akkumulierte 'truncation' Fehler überwiegt. Wir erwarten, daß dieses Verhalten sich auch auf andere Fälle übertragen läßt.
Die adaptive DMRG ist somit eine gut kontrollierbare und sehr effiziente Methode zur Behandlung zeitabhängiger Phänomene.
Die Ergebnisse der Anwendungen können wie folgt zusammengefaßt werden:

Ultrakalte Bosonen Motiviert durch die großen experimentellen Fortschritte, die kürzlich auf dem Gebiet der ultrakalten Atome in optischen Gittern erzielt wurden, haben wir die adaptive t-DMRG auf diese Systeme angewendet. Die Realisierung optischer Gitter eröffnet die Möglichkeit, Probleme aus der Festkörperphysik in einem System zu untersuchen, dessen Parameter besser vorgegeben und zeitlich variiert werden können. Zunächst untersuchen wir den Einfluß des in den quantenoptischen Systemen unvermeidlichen Einschlußpotentials. In einem solchen Potential können gleichzeitig eine superflüssige und Mott-isolierende Phase räumlich voneinander getrennt auftreten. Wir zeigen, daß eine Charakterisierung dieser Phasen durch die zuvor skalierte Einteilchen-Dichtematrix möglich ist. Die skalierte Einteilchen-Dichtematrix

zeigt, wie schon die Einteilchen-Dichtematrix im homogenen System, einen algebraischen Zerfall in der superflüssigen Phase und einen exponentiellen in der Mott-isolierenden Phase. Zur experimentellen Unterscheidung der beiden Phasen ist insbesondere eine Signatur in der Halbwertsbreite der Interferenzbilder geeignet. Diese wurde inzwischen durch Experimente bestätigt.
Als zeitabhängiges Phänomen untersuchen wir die Ausbreitung von Dichtestörungen. Insbesondere berechnen wir erstmalig die Schallgeschwindigkeit für beliebige Wechselwirkungsstärken der Bosonen und zeigen damit die Grenzen der Gültigkeitsbereiche existierender Näherungen. Aus den Rechnungen für Dichtestörungen von unterschiedlicher Stärke und Form können wir eine lineare Abhängigkeit der Geschwindigkeit von der Höhe der Störung ableiten. Diese Abhängigkeit hat Effekte wie Aufsteilung und Schockwellenformation zur Folge. Wir zeigen, daß diese Störungen schon mit den jetzigen experimentellen Mitteln mit Hilfe einer 'time-of-flight'-Messung detektiert werden können.

Ultrakalte Fermionen Eindimensionale Quantensysteme zeigen einige außergewöhnliche Phänomene als Konsequenz der starken Quantenfluktuationen. Eines davon ist die Spin-Ladungstrennung. Nach der Luttinger-Flüssigkeitstheorie entkoppeln Spin- und Ladungsanregungen in eindimensionalen wechselwirkenden Systemen bei niedrigen Energien und breiten sich mit unterschiedlichen Geschwindigkeiten aus. Wir untersuchen die Spin-Ladungstrennung anhand des 1D Hubbard Modells erstmals mit Realzeit-Rechnungen für Systeme, deren Größen den experimentellen entsprechen. Wir zeigen, daß die Spin-Ladungstrennung als charakteristische Eigenschaft eindimensionaler Systeme weit über den Bereich niedriger Energien hinaus erhalten bleibt. Auf diese Ergebnisse aufbauend, schlagen wir ein Experiment vor, das es erlaubt, die Spin-Ladungstrennung in ultrakalten Fermionen zu beobachten. Unser Vorschlag basiert auf der unterschiedlichen Ausbreitung von Spin- und Ladungsanregungen in der flüssigen und Mott-isolierenden Phase. Damit werden Probleme vermieden, die den heutigen experimentellen Vorschlägen anhaften. Ein experimenteller Aufbau dieser Art kann auch für die Unterscheidung eines Mott-Isolators von einem Bandisolator verwendet werden.

Spin-1/2 Kette Der Spintransport zwischen zwei spinpolarisierten Reservoiren ist eine Konfiguration von besonderem Interesse im Bereich der Spintronik. Wir modellieren dieses System durch eine Spinkette, die sich anfänglich in dem Zustand $\left| \uparrow \ldots \uparrow\downarrow \ldots \downarrow \right\rangle$ befindet. Die Kopplung beider Reservoire ist durch die Spinwechselwirkung auf der Kette gegeben. Wir interessieren uns insbesondere dafür, wie das Langzeitverhalten des Spintransports zwischen den beiden Reservoiren von den Eigenschaften des Systems abhängt. In dem Bereich schwacher S_zS_z-Wechselwirkung ist der Transport für lange Zeiten unabhängig von der Dimerisierung ballistisch, wie es schon für verschwindende Wechselwirkung und Dimerisierung bekannt war. Wir finden eine drastische Änderung im Langzeitverhalten in der Nähe des Phasenübergangs. Hier, für stärkere Wechselwirkungen ist der Magnetisierungstransport nicht mehr ballistisch, sondern oszilliert um einen konstanten Wert. Aus diesen Ergebnissen

können wir schließen, daß das Langzeitverhalten des Transports in diesem System nicht alleine durch Systemeigenschaften —Integrabilität, Kritikalität und Erhaltungsgrößen— bestimmt wird. Die abrupte Änderung des Verhaltens am Phasenübergang erklären wir durch die Ähnlichkeit des Anfangszustandes mit dem Grundzustand in der ferromagnetischen Phase.

Die guten Ergebnisse der in dieser Arbeit dargestellten Anwendungen lassen erwarten, daß mögliche Generalisierungen der adaptiven Methode geeignet sind, zukünftig weitere interessante Fragen der Festkörperphysik und der quantenoptischen Systeme im Wechselspiel beider Gebiete zu bearbeiten.

1. Introduction

In recent years an increasing number of experimental results on time-dependent phenomena has been achieved in condensed matter and quantum optical systems. In the area of condensed matter physics great experimental progress on the study of these phenomena has been made, e.g., in nanophysics and spintronics. It allowed to investigate the transport behaviour through low dimensional structures of various geometries such as quantum dots or quantum wires and the response of such systems to external potentials. In the area of quantum optics one prominent example for time-dependent phenomena is the realization of a driven quantum phase transition in ultracold bosons confined by an optical lattice [1]. Time-dependent variations of the optical lattice depth allowed to drive the transition between a superfluid (metallic) and a Mott-insulating regime.
Despite the recent progress on the experimental side the theoretical description of non-equilibrium phenomena is still lacking. In this work we develop a new numerical method, the adaptive time-dependent density-matrix renormalization-group (adaptive t-DMRG), which turns out to be very well suited to investigate time-dependent phenomena in one-dimensional strongly correlated systems. We show its applicability to different physical systems: bosonic, fermionic and spin chains.

Adaptive t-DMRG As for static phenomena, the fundamental problem for the treatment of time-dependent quantum phenomena is the large size of the Hilbert space required. In the case of low-energy equilibrium properties the invention of the density-matrix renormalization-group method (DMRG) brought decisive progress. It iteratively decimates the Hilbert space of a growing quantum system such that the state of interest, say the ground state, is approximated in a space of reduced dimension having a maximum overlap with the true state [2, 3, 4]. For time-dependent phenomena, very often a fixed reduced space of practical size cannot cover the whole time evolution of the system. The reduced space has to be adapted in time to give a good description of the time evolution of the state of interest. This was first realized in the time evolving block-decimation (TEBD) procedure by G. Vidal [5], an algorithm to simulate slightly entangled quantum systems. As it is best seen in the language of matrix-product states, the TEBD and the DMRG are closely related. Thus, as will be shown in chapter 2, generalizing the original DMRG can be generalized by incorporating the idea of the TEBD algorithm. This results in a very efficient algorithm, the adaptive t-DMRG [6, 7], which can treat time-dependent phenomena with remarkable success. This can be seen from the applications of the adaptive t-DMRG described in this thesis which are concerned with ultracold bosons, fermions and spin transport in one-dimensional chains.

Ultracold Bose gases in optical lattices The first application of the adaptive t-DMRG presented in this work is from the area of ultracold bosons. In recent years the experimental progress in these systems initiated a connection between quantum optics and condensed matter systems. The pioneering work was the experimental achievement of the Bose-Einstein condensate [8, 9, 10], which opened the way to numerous exciting experiments directly probing fundamental effects of quantum mechanics. Up until the last few years most phenomena experimentally exploited could be described theoretically by considering the dynamics of weakly interacting Bose gases in the framework of the Gross-Pitaevskii equation and the Bogoliubov theory [11, 12]. More recently a new regime, the regime of strong interaction, became experimentally accessible [13, 14, 15]. From the many-body point of view this is a more sophisticated regime, since interaction induced many-body effects have to be taken into account. The experiment which illustrated best the presence of 'real' many-body effects was that of Greiner et al. [1] in which they managed to realize the quantum phase transition from a superfluid to a Mott-insulating phase in a system of ultracold atoms confined to an optical lattice. This experiment has attracted a lot of attention, since it realizes of one of the most prominent phase transition in condensed matter systems, thereby showing the possibility to realize and clarify solid-state phenomena in a new context. In contrast to most condensed matter systems, these systems of ultracold atoms have the advantage that many parameters can be experimentally controlled very precisely and rapidly changed. Thereby, it opens up a whole new area of non-equilibrium phenomena, the theoretical description of which is very demanding.
In this thesis we show how the new adaptive t-DMRG allows us to study some of these phenomena. But before this, we discuss the consequences of the presence of an *external trapping potential* on the static properties of the system (chapter 3). The trapping potential is one of the main differences between the quantum optical systems and the condensed matter systems. One of the consequences is the possibility of the spatially separated coexistence of the superfluid and the Mott-insulating phases. The question arises which properties of their homogeneous counterparts survive in these coexisting states. We show that after a simple scaling procedure the one-particle density-matrix can be used to characterize the state of the system just as for homogeneous systems. We confirm the application of the widely used hydrodynamic approach for the system with the parabolic trap in the limit of weak interactions by comparing it to the DMRG results. Further we discuss how the different states can be distinguished experimentally. Hereby we present results for the interference pattern and point out that the experimental quantity which reveals most about the state of the system is the half width of the interference peak.
In chapter 4 we turn to *the evolution of density perturbations* in a gas of ultracold bosons subjected to an optical lattice. We investigate the propagation of density-wave packets in a Bose-Hubbard model using the adaptive t-DMRG. Until now the propagation had only been studied for the case of very broad and weak perturbations in the presence of weak interactions. In contrast, here we discuss the dependence of the velocity and of the decay of the amplitude on density, interaction strength and the extent and height of the perturbation in

a numerically exact way, covering a wide range of interaction and of perturbation strengths. By comparing our results for the sound velocity to theoretical predictions, we determine the limits of a Gross-Pitaevskii or Bogoliubov type description and the regime where repulsive one-dimensional Bose gases exhibit fermionic behaviour. In addition, we investigate the effect of self-steepening due to the amplitude dependence of the velocity and discuss the possibilities for an experimental detection of the moving wave packet in time-of-flight pictures.

Ultracold fermions As a second application of the adaptive t-DMRG, we investigate the phenomenon of *spin-charge separation* and propose an experimental setup for its observation in cold Fermi gases. The spin-charge separation – the complete decoupling of spin and charge excitations at low energies – is one of the key features of one-dimensional quantum physics. It is in striking contrast to Fermi-liquids, where elementary quasi-particles exist which carry both charge and spin. Using the adaptive t-DMRG for the 1D Hubbard model, the splitting of local perturbations into separate wave packets carrying charge and spin is calculated in real-time. We show the robustness of this separation beyond the low-energy regime by studying the time evolution of density wave packets of finite strength and at length scales down to a few lattice spacings. A striking signature of spin-charge separation is found in 1D cold Fermi gases in a harmonic trap using the different propagation properties of the liquid and Mott-insulating phases. We give quantitative estimates for an experimental observation of spin-charge separation in an array of atomic wires.

Spin transport The third application relates to the area of spintronics. A simplified model for the *magnetization transport* between two coupled reservoirs with opposite spin polarization is studied. This is done by calculating the transport properties of a spin-1/2 chain which is initially in the state $\left| \uparrow \ldots \uparrow\downarrow \ldots \downarrow \right\rangle$, with all spins pointing up in the left half of the system and all spins pointing down in the right half. Thus, each half of the system corresponds to one spin-polarized reservoir. The coupling within and between the reservoirs are both given by nearest-neighbour spin interactions. We focus our study on the long time behaviour of the system. In particular, we investigate whether a simple long time limit for the spin transport exists and if so, how it depends on the properties of the system such as integrability and criticality. Time-scales accessible to us are of the order of 100 units of time measured in $\hbar/J$ while maintaining insignificant error in the observables.
Additionally, we perform a detailed analysis of the error made by the adaptive t-DMRG using the fact that the evolution in the XX-model is known exactly. We find that the error at small times is dominated by the error made by the Suzuki-Trotter decomposition whereas for longer times the DMRG truncation error becomes the most important, with a very sharp crossover at some "runaway" time. Overall, errors are extremely small before the "runaway" time.

2. The adaptive time-dependent density-matrix renormalization-group method

2.1. Can DMRG be applied to time-dependent phenomena?

Over many decades the description of the physical properties of low-dimensional strongly correlated quantum systems has been one of the major tasks in theoretical condensed matter physics. In most cases the problem is that due to the large size of the Hilbert space no exact solution of the quantum systems is possible. In low dimensional systems, in general, this task is complicated further by the strong quantum fluctuations present in such systems which are usually modeled by minimal-model Hubbard or Heisenberg-style Hamiltonians. Despite the apparent simplicity of these Hamiltonians, few analytically exact solutions are available and most analytical approximations remain uncontrolled. Hence, numerical approaches have always been of particular interest, among them exact diagonalization and quantum Monte Carlo.

Decisive progress in the description of the low-energy equilibrium properties of one-dimensional strongly correlated quantum systems was achieved by the invention of the density-matrix renormalization-group method (DMRG) [2, 16]. It is concerned with the iterative decimation of the Hilbert space of a growing quantum system. The Hilbert space of this system would otherwise grow exponentially, when the system is enlarged linearly. The DMRG constructs a reduced space of fixed dimension and approximates the quantum state of interest, say the ground state, in that reduced space with a maximum of overlap with the true state.

While the DMRG method has yielded an enormous wealth of information on the static and dynamic equilibrium properties of one-dimensional systems [3, 4] and is one of the most powerful methods in the field, only few attempts have been made so far to determine the time evolution of the states of such systems, notably in a seminal paper by Cazalilla and Marston [17].

In the quite different context of quantum information science G. Vidal has recently developed an algorithm for the simulation of slightly entangled quantum computations [18] that can be used to simulate time evolutions of one-dimensional systems [5]. This new algorithm, henceforth referred to as the time-evolving block decimation (TEBD) algorithm, considers a small, dynamically updated subspace to efficiently represent the state of the system. It was originally developed in order to show that a large amount of entanglement is necessary to make quantum computations whereas any *quantum* evolution in-

volving only a "sufficiently restricted" amount of entanglement can be efficiently simulated in a *classical* computer using the TEBD algorithm. The above connection between the amount of entanglement and the complexity of simulating quantum systems by classical computers is of obvious practical interest in condensed matter physics. For instance, in one dimension the entanglement of most quantum systems happens to be "sufficiently restricted" precisely in the sense required for the TEBD algorithm to yield an efficient simulation.
In this thesis the TEBD algorithm is reexpressed in a language more familiar to the DMRG community than the one originally used in Refs. [5, 18], which made substantial use of the quantum information parlance. This reformulation turns out to be a rewarding task since, as we show, the conceptual and formal similarities between the TEBD and DMRG are extensive. Both algorithms search for an approximation of the true wave function within a restricted class of wave functions, which can be identified as matrix-product states [19], previously also proposed under the name of finitely-correlated states [20]. The great advantage of the TEBD algorithm lies in its flexibility to flow in time through the submanifold of matrix-product states whereas the original DMRG only constructs a fixed reduced space. In this chapter we show how the two algorithms can be integrated [6]. We will describe how the TEBD simulation algorithm can be incorporated into preexisting, quite widely used DMRG implementations, the so-called finite-system algorithm [16] using White's prediction algorithm [21]. The advantage of the new algorithm is that it uses well-known DMRG techniques, such as the handling of good quantum numbers. Therefore the net result is an extremely powerful "adaptive time-dependent DMRG" algorithm (adaptive t-DMRG).
The outline of this chapter is as follows: In section 2.2 the original DMRG algorithm is reviewed. Further details on the DMRG algorithm can be found for example in [3, 4, 22]. In section 2.3, the problems encountered in applying DMRG to the calculation of explicitly time-dependent quantum states are discussed. Section 2.4 reviews the language of matrix product states. Then both the TEBD simulation algorithm (section 2.5) and DMRG (section 2.6) are expressed in this language, revealing where both methods coincide, where they differ and how they can be combined. In section 2.7, the modifications to introduce the TEBD algorithm into standard DMRG to obtain the adaptive t-DMRG are pointed out. Section 2.8 we test the new algorithm at small bosonic systems and compare it to previous proposals. In section 2.9 the sources of errors are identified. A detailed error analysis is performed later in the context of spin-chains 6.3.

2.2. 'Original' density-matrix renormalization-group method

The density-matrix renormalization group (DMRG), which was developed by White in 1992 [2, 16], is one of the most precise numerical methods to study low-dimensional strongly correlated systems. Originally, it was introduced to compute the ground state and low-energy spectrum of a quantum system with short-range interactions.

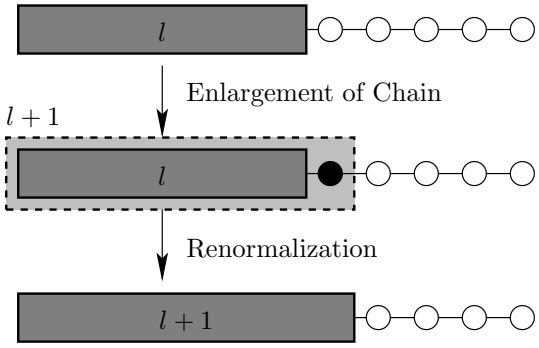

Figure 2.1.: Schematic plot of the real-space renormalization. [22]

The DMRG algorithm is based on the general concept of the 'renormalization methods'. Starting from some microscopic Hamiltonian, degrees of freedom are integrated out iteratively, such that an effective description of the system is obtained. Hereby the difficulty is to obtain an effective description which still covers the essential physics. The DMRG-algorithm starts with a quantum chain (also called "block") of length l, that is sufficiently small to be represented numerically on a computer (Fig. 2.1). Then, the chain is enlarged sequentially by one site to increase the system size. In order to reduce the with l exponentially growing dimension of the Hilbert space, after each enlargement step the system is projected onto a *fixed* number m of relevant Hilbert space states sketched in Fig. 2.1 by the block. All remaining states are cut off and neglected for the next iteration step. Obviously the crucial question arises which states are in that sense "relevant".

White and Noack [3] found that keeping only the lowest lying energy eigenstates, generally does not give a good decimation procedure. This can be understood considering the toy model of a single non-interacting particle hopping on a discrete one-dimensional lattice. If one starts with a small system, say block A in Fig. 2.2, the lowest lying eigenstates (dashed curves in Fig. 2.2) for the single particle in the box have nodes at the lattice end of block A. If the system is enlarged by doubling the system to obtain the compound block AA, the new lowest lying eigenstates have a maximum amplitude at the compound block center. Therefore it cannot be approximated well by a restricted number of block states, i.e. eigenstates of the two blocks which have nodes at the center

of the compound block[1]. To avoid imposing the wrong boundary conditions by considering separate blocks A, White [2] had the idea to embed the block A in some environment to mimic a larger system from the beginning.

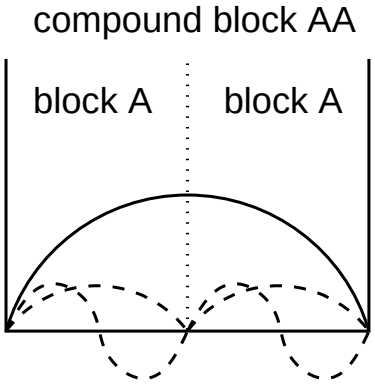

Figure 2.2.: Two blocks A are connected to form the compound block AA. The dashed lines are the lowest energy eigenstates of the separate blocks A, the solid line sketches the lowest energy eigenstate of the compound block AA.

The DMRG algorithm follows this idea using the so called density-matrix projection described in the next section as a procedure to select the relevant states [2, 16].

2.2.1. Density-matrix projection

The idea of the density-matrix projection is to embed a small system into a larger one to mimic a large system. Using the information given by the reduced density-matrix of the small system (S) the information of the 'environment' (E) is implicitly included to decide which are the relevant states to be chosen when enlarging the small systems up to the desired length L.

Let us describe this procedure in more detail. Assume that we have reached a chain of length l with an m-dimensional Hilbert space with states $\{|w^S_{m_l}\rangle\}$. To grow the system one new site is added, i.e. the basis of the new Hilbert space $\mathcal{H}_S$ is given by $\{|w^S_{m_l}\sigma^S\rangle\} = \{|w^S_{m_l}\rangle|\sigma^S\rangle\}$, where $|\sigma^S\rangle$ are the N_{site} local states of the new site. In order to avoid strong boundary effects the system (S) is embedded into an 'environment' (E) which was constructed in the same way. We denote its basis states by $\{|w^E_{m_l}\sigma^E\rangle\}$. We call the two parts the system and the environment block, and both together the 'superblock' (Fig. 2.3).

The aim of the density-matrix projection is to determine a small set of $m^S < k := \dim \mathcal{H}_S$ states $|w^S_{m_{l+1}}\rangle \in \mathcal{H}_S$ $(m_{l+1} = 1 \dots m^S)$ which are important to represent a certain state $|\psi\rangle$, e.g. the ground state, (also called *target state*) of

[1] Here we doubled the system size to make the point clear, whereas later on we only add several sites.

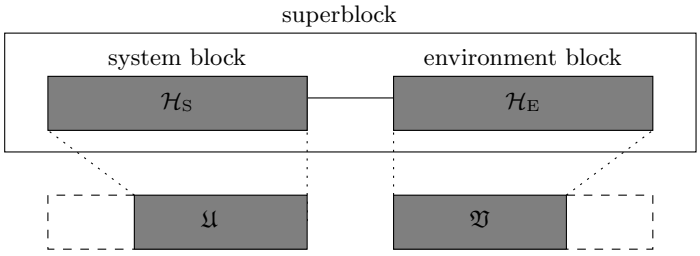

Figure 2.3.: Schematic diagram of the superblock, that consists of a system and environment block [22] and of the corresponding reduced spaces

the superblock

$$\begin{aligned} \big|\psi\big\rangle &= \sum_{m_l=1}^{m^S}\sum_{\sigma^S=1}^{N_{site}}\sum_{m_l'=1}^{m^E}\sum_{\sigma^E=1}^{N_{site}} \psi_{m_l\sigma^S m_l'\sigma^E}\big|w^S_{m_l}\sigma^S\big\rangle\big|w^E_{m_l'}\sigma^E\big\rangle \\ &\equiv \sum_{ij}\psi_{ij}\big|i\big\rangle_\mathrm{S}\otimes\big|j\big\rangle_\mathrm{E}. \end{aligned} \tag{2.2.1.1}$$

Here, we expanded $\big|\psi\big\rangle$ into the orthonormal bases $\big|i\big\rangle_\mathrm{S}$ $(i=1\ldots k)$ and $\big|j\big\rangle_E$ $(j=1\ldots k)$ of the system $\mathcal{H}_\mathrm{S}$ and environment $\mathcal{H}_\mathrm{E}$, respectively. The 'relevant' states $\big|w^S_{m_{l+1}}\big\rangle$ are the states which span the m^S-dimensional subspace $\mathfrak{U}\subset\mathcal{H}_S$, such that the vector

$$\big|\tilde\psi\big\rangle = \sum_{m_{l+1},j}\tilde\psi_{m_{l+1}j}\big|w^S_{m_{l+1}}\big\rangle\otimes\big|j\big\rangle_\mathrm{E}\in\mathfrak{U}\otimes\mathcal{H}_E, \tag{2.2.1.2}$$

minimizes the functional of the quadratic deviation

$$S\big(\big|\tilde\psi\big\rangle\big) := \Big\|\big|\psi\big\rangle-\big|\tilde\psi\big\rangle\Big\|^2 . \tag{2.2.1.3}$$

In the following it is shown that the 'relevant' states $\big|w^S_{m_{l+1}}\big\rangle$ are given by the eigenvectors to the leading eigenvalues of the reduced density-matrix

$$\hat\rho_S := \mathrm{Tr}_E\,\big|\psi\big\rangle\big\langle\psi\big| , \tag{2.2.1.4}$$

where $\mathrm{Tr}_E := \mathrm{id}_\mathrm{S}\otimes\mathrm{tr}_\mathrm{E}$ labels the partial trace over the environment block. We interpret the coefficients ψ_{ij} and $\tilde\psi_{ij}$ as $k\times k$ matrices $\psi=(\psi_{ij})_{ij}$ and $\tilde\psi=(\tilde\psi_{ij})_{ij}$ (where $\mathrm{rank}\left(\tilde\psi\right)\le m^S$), respectively. Then, the density-matrix $\hat\rho_S$ can be written as $\rho_S=\psi\psi^\dagger$ and the functional $S\left(\big|\tilde\psi\big\rangle\right)$ can be expressed as

$$S(\tilde\psi) = \mathrm{tr}\,(\psi-\tilde\psi)^\dagger(\psi-\tilde\psi) . \tag{2.2.1.5}$$

The functional S can be related to the eigenvalues of the reduced density-matrix by using the *singular value decomposition* theorem. According to this theorem there exist two orthogonal matrices U and V of dimension $k\times k$ such that

$$\psi = UDV^\dagger , \quad \text{where} \quad D=\mathrm{diag}(\lambda_1,\ldots,\lambda_k). \tag{2.2.1.6}$$

The so-called *singular values* λ_i are the square roots of the eigenvalues of ρ_S, since we can write

$$\rho_S = UDD^\dagger U^\dagger = UD^2U^\dagger \ . \tag{2.2.1.7}$$

Inserting (2.2.1.6) into (2.2.1.5) and using the cyclic invariance of the trace, we obtain

$$S(\tilde{\psi}) = \mathrm{tr}\,(D-\tilde{D})^\dagger(D-\tilde{D}) \ . \tag{2.2.1.8}$$

with $\tilde{D} := U^\dagger\tilde{\psi}V$. In this form it can be seen that S is minimized, if $\tilde{D}$ is a diagonal matrix of rank m^S, whose diagonal elements are given by the leading singular values, i.e.

$$\tilde{D} = \mathrm{diag}(\lambda_1,\ldots,\lambda_{m^S},0,\ldots,0) \ . \tag{2.2.1.9}$$

Without loss of generality the λ_i were assumed to be sorted: $\lambda_1 \geq \lambda_2 \geq \cdots \geq \lambda_k$. We can explicitly construct $\big|\tilde{\psi}\big\rangle$ which minimizes S using the eigenvectors $\big|w^S_{m_{l+1}}\big\rangle$ to the leading m eigenvalues of $\hat{\rho}_S$:

$$\begin{aligned}
\big|\tilde{\psi}\big\rangle &= \sum_{ij}(U\tilde{D}V^\dagger)_{ij}\big|i\big\rangle_{\mathrm{S}}\otimes\big|j\big\rangle_{\mathrm{E}} \\
&= \sum_{m_{l+1}}\tilde{D}_{m_{l+1},m_{l+1}}\Big(\underbrace{\sum_i U_{im_{l+1}}\big|i\big\rangle_{\mathrm{S}}}_{\big|w^S_{m_{l+1}}\big\rangle}\Big)\otimes\Big(\underbrace{\sum_j V^*_{jm_{l+1}}\big|j\big\rangle_{\mathrm{E}}}_{\big|w^E_{m_{l+1}}\big\rangle}\Big) \\
&= \sum_{m_{l+1}=1}^{m}\lambda_{m_{l+1}}\big|w^S_{m_{l+1}}\big\rangle\otimes\big|w^E_{m_{l+1}}\big\rangle
\end{aligned} \tag{2.2.1.10}$$

Note, that the same number of states has to be kept for the system and the environment block, i.e. $m := m^S = m^E$. If the same projection is performed interchanging the system and environment block, one finds that both reduced density-matrices have the same non-zero eigenvalues even if system and environment were different. This is also reflected in the guaranteed existence of the so-called Schmidt decomposition of the wave function [23],

$$\big|\psi\big\rangle = \sum_\alpha \lambda_\alpha\big|w^S_\alpha\big\rangle\big|w^E_\alpha\big\rangle, \quad \lambda_\alpha \geq 0, \tag{2.2.1.11}$$

which plays a key-role in the connection between the TEBD and DMRG. The number of positive λ_α is bounded by the dimension of the smaller of the bases of system and environment.

To summarize, we have proven that the relevant states of the system block to represent the target state, e.g. the ground state, of a larger quantum chain including the environment are optimally given by the leading m eigenvectors of the reduced density-matrix ρ_S.

The performance of the method depends critically on the decay of the eigenvalues of the reduced density-matrix. Some insight into the quality of the truncation approximation made by the projection can be gained by the so-called

truncated weight

$$P := 1 - \sum_{i=1}^{m} \lambda_i^2 \tag{2.2.1.12}$$

which measures how much of the norm of $|\psi\rangle$ is lost. However, due to the additional sources of 'environmental' errors — errors by the only approximate similarity of the environment block to the 'real' environment— the total error in the observables calculated are often much larger than the truncated weight. A good control over the total error can in most cases be obtained by a careful convergence analysis in the number m of states kept.

More information about the limits of the DMRG was obtained by [24, 25, 26, 27, 28, 29] by studying the ability of the DMRG decimation procedure to preserve the entanglement of $|\psi\rangle$ between system and environment in the context of quantum information science [23, 30]. By this a better understanding of the reasons of the breakdown of the DMRG in two-dimensional systems has been obtained in terms of the growth of bipartite entanglement in such systems [27, 29].

More specifically, in quantum information the entanglement of $|\psi\rangle$ between system and environment is quantified by the von Neumann entropy of $\hat{\rho}_S$ (equivalently, of $\hat{\rho}_E$),

$$\mathcal{S}(\hat{\rho}_S) = -\sum \lambda_\alpha^2 \log_2 \lambda_\alpha^2, \tag{2.2.1.13}$$

a quantity that imposes a useful (information theoretical) bound $m \geq 2^{\mathcal{S}}$ on the minimal number m of states to be kept during the DMRG decimation process if the truncated state is to be similar to $|\psi\rangle$. Still more insight into the power of the DMRG comes from arguments from field theory which imply that, at zero temperature, strongly correlated quantum systems are in some sense only slightly entangled in $d = 1$ dimension but significantly more entangled in $d > 1$ dimensions: In particular, in $d = 1$ a block corresponding to l sites of a gapped infinite-length chain has an entropy $\mathcal{S}_l$ that stays finite even in the thermodynamical limit $l \to \infty$, while at criticality $\mathcal{S}_l$ only grows logarithmically with l. It is this saturation or, at most, moderate growth of $\mathcal{S}_l$ that ultimately accounts for the success of DMRG in $d = 1$. In the general d-dimensional case the entropy of bipartite entanglement for a block of linear dimension l scales as $\mathcal{S}_l \sim l^{d-1}$. Thus, in $d = 2$ dimensions the DMRG algorithm should keep a number m of states that grows exponentially with l, and the simulation becomes inefficient for large l (while still feasible for small l).

2.2.2. DMRG algorithm

In this section the two DMRG algorithms, the so-called *infinite-system* and the *finite-system* algorithm [16] are introduced. Often, a combination of both algorithms is applied to obtain an increased accuracy of the numerical results.

Infinite-system algorithm

The infinite-system algorithm is designed for computing the ground state (or low-energy spectrum) of a quantum chain in the thermodynamic limit ($L \to \infty$, where L is the desired length of the system). It contains the following iterative steps:

1. Construct a system of size l with the Hilbert space $\mathcal{H}^S = \{|w^S_{m_l}\rangle\}$ with dimension m^S which is small enough to be treated exactly. The operators used, including the Hamiltonian, are known in this basis. In the same way construct the environment block.

2. Enlarge the system block by one site 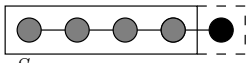 , i.e. the Hilbert space becomes of dimension $N^S = m^S N_{site}$ and is formed by the states $\{|w^S_{m_l}\sigma^S\rangle\}$.
   The environment block is enlarged, similarly. The added sites are often called 'free' or 'active' sites.

3. Join the two blocks to form the superblock of length $2l + 2$ (Fig. 2.3). The dimension of the Hilbert space of the superblock is given by $N^S N^E$.

4. Determine the target state. If the target state is the ground state this is done by determining the ground state of the Hamiltonian of the superblock for example by the Lanczos algorithm [31].

5. Perform the density-matrix projection for the system, i.e. determine from the reduced density-matrix $\hat{\rho}_S$ as in Eq. (2.2.1.4), the eigenvalues, ordered by their values, and the corresponding eigenstates. Form a new reduced basis by taking only the m^S eigenstates $|w^S_{m_{l+1}}\rangle$ corresponding to the largest eigenvalues. Repeat this step to construct the reduced basis and the projection matrix for the environment.

6. Project the operators of interest acting on the system and the environment block, including the Hamiltonian, onto the new basis of the system and the environment block, respectively. The projection matrix $T^{S/E}$ of dimension $N^{S/E} \times m^{S/E}$ is given by taking the eigenvectors as columns. Repeat step (2) to (6) until the desired final length L of the system is reached.

7. Calculate the physical quantities of interest, like expectation values for the ground state energy, from the effective state obtained.

Obviously, the chain length l grows successively by each iteration step until it reaches the desired length, whereas the dimensions m of the system and the environment block stay constant. By this infinite-system analysis, highly precise estimates of various properties of the infinitely large quantum chain are possible.
The scheme given above is only a rough sketch of the DMRG algorithm. An implementation of a DMRG program generally facilitates various numerical know-how to increase the performance and to save computer memory. E.g. if some quantum numbers are conserved, the fact can be utilized to reduce

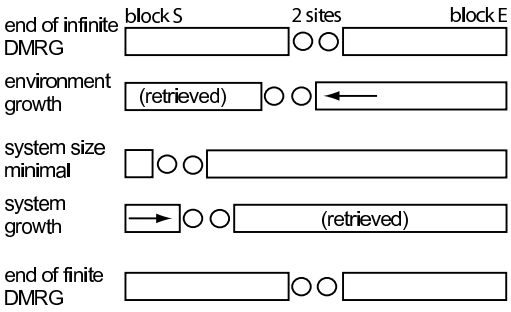

Figure 2.4.: Finite-system DMRG algorithm. Block growth and shrinkage.

operators to a block structure, such that vanishing matrix elements do not have to be stored. The most time consuming part of the algorithm is found in the computation of the ground state, step (4). Here, the Davidson [32] or Lanczos [31] algorithm are typically used due to their high performance.

Finite-system algorithm

The infinite-system algorithm does not give satisfactory results in all cases of interest. Problems arise if the environment in the early growing of the chain does not resemble the system of final length closely enough, for example, if the system is inhomogeneous. Then the states retained in the early stage do not have to be important for the desired final state. Here the finite-system algorithm helps out. The idea is to optimize the chosen basis for a system of fixed length L by shifting the 'free' sites through the system. To do this the system is built up to a desired length L with the infinite-system algorithm, but in subsequent steps one of the blocks grows to the cost of the other block shrinking (see Fig. 2.4). In each step the reduced basis transformation is only performed for the growing block.
Assume the system block grows and the environment block shrinks. Then as before in the infinite-system algorithm one site is added to the system block, but at the same time one site is removed from the environment block, i.e. one has to use the previously stored basis of the smaller block. When the environment block approaches the end of the chain it becomes at some step exactly describable and the role of the shrinking and growing blocks are interchanged. A complete shrinkage and growth sequence for both blocks is called a 'sweep'. The advantage of this algorithm is that the system has reached its final length L and the chosen basis states can be optimized taking its full length into account. Usually the finite-system algorithm finds the best approximation to the ground state, and only very rarely it is trapped into some metastable state. Some of the problems encountered in inhomogeneous systems will be discussed in section 3.5, when the Bose-Hubbard model is investigated with an external parabolic trapping potential.

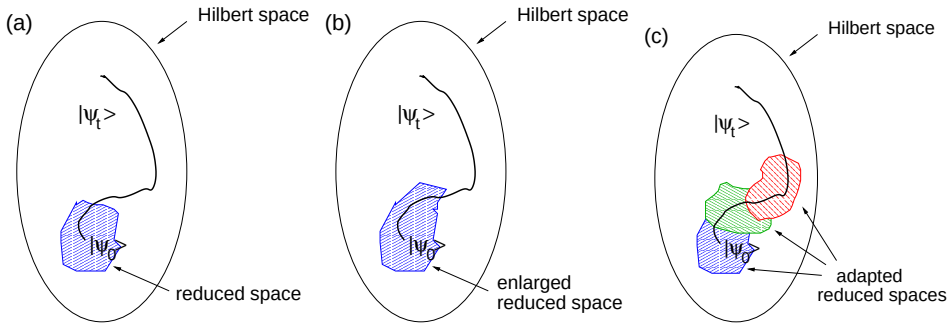

Figure 2.5.: Sketch of the different approaches to determine the time evolution of a state $|\psi_0\rangle$: (a) the time evolution is performed in the fixed reduced space obtained by the initial DMRG run, (b) the time evolution is performed in an enlarged fixed reduced space, and (c) the reduced space is adapted in time, while the state evolves. The line sketches the 'real' time evolution of the state $|\psi_0\rangle$, i.e. the time-evolution taking the full Hilbert space into account.

2.3. Simulation of time-dependent quantum phenomena using DMRG

For the calculation of the time evolution of a quantum state using DMRG, we have compared several possible approaches, schematically shown in Fig. 2.5 including our new adaptive t-DMRG [Fig. 2.5 (c)]. The first attempt to simulate the time evolution of quantum states using DMRG is due to Cazalilla and Marston [17]. Their idea was to determine the time evolution of a state $|\psi_0\rangle$ in a reduced effective space constructed using the DMRG. It is sketched in Fig. 2.5 (a). To do this they represented the initial state $|\psi_0\rangle$, say the ground state of some Hamiltonian $\hat{H}(t=0)$, in an effective reduced space obtained by a DMRG run. Then they calculated the time evolution of this state $|\psi_0\rangle$ subjected to a Hamiltonian $\hat{H}(t) = \hat{H}(0) + \hat{V}(t)$ in the same reduced space by projecting the time-dependent Schrödinger equation onto the effective space and integrated it forward in time numerically. Hereby the Hamiltonian is built by $\hat{H}_{\text{eff}}(t) = \hat{H}_{\text{eff}}(0) + \hat{V}_{\text{eff}}(t)$, where $\hat{H}_{\text{eff}}(0)$ is taken as the Hamiltonian approximating $\hat{H}(0)$ in the truncated Hilbert space generated by DMRG. $\hat{V}_{\text{eff}}(t)$ as an approximation to $\hat{V}(t)$ is built using the representations of operators in the block bases obtained in the standard DMRG calculation of the $t = 0$ state. The projected time-dependent Schrödinger equation reads

$$i\frac{\partial}{\partial t}|\psi_{\text{eff}}(t)\rangle = [\hat{H}_{\text{eff}}(0) - E_0 + \hat{V}_{\text{eff}}(t)]|\psi_{\text{eff}}(t)\rangle, \tag{2.3.0.1}$$

where the time-dependence of the initial state $|\psi_0\rangle$ resulting of the initial Hamiltonian $\hat{H}(0)$ has been transformed away.
Sources of errors in this approach are twofold, due to the approximations involved in numerically carrying out the time evolution, and to the fact that the evolution is projected onto a fixed reduced Hilbert space. We have investigated

these two error sources in some detail and found that in most cases the first error (i) can be well controlled whereas the error introduced by the single reduced space (ii) causes the breakdown of the method after a relatively short time.
(i) To minimize the *errors induced by the forward integration in time*, we compared two different algorithms: the adaptive Runge-Kutta and the Crank-Nicolson algorithm (see [33] and references therein).
The first order Runge-Kutta integration is based on the infinitesimal time evolution operator

$$\big|\psi(t+\mathrm{d}t)\big\rangle \approx (1-\mathrm{i}\hat{H}(t)\mathrm{d}t)\big|\psi(t)\big\rangle, \tag{2.3.0.2}$$

where the subscript is dropped denoting that we are dealing with effective Hamiltonians acting on the reduced space only. As a first approach the fourth-order adaptive size Runge-Kutta algorithm [33] was applied. Hereby unphysical asymmetries with respect to reflection about the center were generated in a system with reflection symmetry. We have obtained a conceptually simple improvement concerning the time evolution by replacing the explicitly non-unitary time-evolution of the Runge-Kutta algorithm [see Eq. (2.3.0.2)] by the unitary Crank-Nicolson time evolution

$$\big|\psi(t+\mathrm{d}t)\big\rangle \approx \frac{1-\mathrm{i}\hat{H}(t)\mathrm{d}t/2}{1+\mathrm{i}\hat{H}(t)\mathrm{d}t/2}\big|\psi(t)\big\rangle. \tag{2.3.0.3}$$

To implement the Crank-Nicolson time evolution efficiently we have used a (non-Hermitian) biconjugate gradient method to calculate the denominator of Eq. (2.3.0.3). Comparing the Runge-Kutta and the Crank-Nicolson algorithm, already the first-order Crank-Nicolson (with time steps of $\mathrm{d}t = 5 \times 10^{-5}\hbar/J$) was found to be numerically preferable over the fourth-order adaptive Runge-Kutta algorithm and well controlled by the parameter $\mathrm{d}t$. In particular, the occurrence of asymmetries with respect to reflection in the results decreased. Therefore, all static (non-adaptive) time-dependent DMRG calculations shown here have been carried out using the Crank-Nicolson approach.
(ii) However, the *the error induced by the truncation* leads to more severe consequences. The key assumption underlying the approach of Cazalilla and Marston is that the effective fixed Hilbert space created in the preliminary DMRG run is sufficiently large that $\big|\psi(t)\big\rangle$ can be well approximated within that Hilbert space for all times, such that

$$\epsilon(t) = 1 - |\langle\psi(t)|\psi_{\mathrm{exact}}(t)\rangle| \tag{2.3.0.4}$$

remains small as t grows. At the momentarily available computer resources this, in general, will only be true for relatively short times. A simple picture for the breakdown is given in Fig. 2.5 (a), where the real time evolution of the state leaves the reduced space at some time, such that it cannot be approximated well in the reduced space anymore.
A variety of modifications that should extend the applicability of the fixed Hilbert space in time can be imagined. The underlying idea is to enlarge the reduced space 'along' the path of the time evolution [as sketched in Fig. 2.5 (b)].

Typically these enlargements rest on the DMRG practice of "targeting" several states: to construct a reduced effective space optimized to represent not only one but several target states. To obtain this space the reduced density-matrix is built out of a mixture of a small number of states, i.e.

$$\hat{\rho}_S = \mathrm{Tr}_E \big|\psi\big\rangle\big\langle\psi\big| \rightarrow \hat{\rho}_S = \mathrm{Tr}_E \sum_i \alpha_i \big|\psi_i\big\rangle\big\langle\psi_i\big|. \tag{2.3.0.5}$$

The reduced effective space is constructed as before by keeping only the m eigenvectors with the highest weight. A simple choice uses the targeting of $\hat{H}^n\big|\psi_0\big\rangle$, for n less than 10 or so, approximating the short-time evolution, which we have found to substantially improve the quality of results for non-adiabatic switching of Hamiltonian parameters in time: convergence in m is faster and more consistent with the new adaptive t-DMRG method (see below).
Similarly, we have found that for adiabatic changes of Hamiltonian parameters results improve if one targets the ground states of both the initial and final Hamiltonian.
A more elaborate, but also much more time-consuming improvement still within the framework of a fixed Hilbert space was proposed by Luo, Xiang and Wang [34, 35]. Additional to the ground state a finite number of quantum states at various discrete times should be targeted using a bootstrap procedure starting from the time evolution of smaller systems that are iteratively grown to the desired final size.
To illustrate the previous approaches and to test the quality of the performance of the different algorithms, we show results for the Bose-Hubbard Hamiltonian,

$$\hat{H}_{BH}(t) = -J \sum_{i=1}^{L-1} \left(b_{i+1}^\dagger b_i + b_i^\dagger b_{i+1} \right) + \frac{U(t)}{2} \sum_{i=1}^{L} n_i(n_i - 1), \tag{2.3.0.6}$$

where the (repulsive) onsite interaction $U > 0$ is taken to be time-dependent. This model exhibits for commensurate filling a Kosterlitz-Thouless-like quantum phase transition from a superfluid phase for $u < u_c$ (with $u = U/J$) to a Mott-insulating phase for $u > u_c$. For more details on the physics of the Bose-Hubbard model see section 3.3. In the present section the instantaneous switching from $U_1 = 2$ in the superfluid phase to $U_2 = 40$ in the Mott phase at $t = 0$ in a small Bose-Hubbard system with $L = 8$ and open boundary conditions, total particle number $N = 8$, $J = 1$ were used. We compare results for the nearest-neighbour correlation $\langle b_j^\dagger b_{j+1} \rangle$, a robust numerical quantity, between sites 2 and 3. Up to 8 bosons per site (i.e. $N_{\mathrm{site}} = 9$ states per site) were allowed to avoid cut-off effects in the bosonic occupation number in all calculations in this section. In the following all times are measured in units of $\hbar/J$ or $1/J$, setting $\hbar \equiv 1$.
First we compare the results for different choices of a fixed reduced space. To do this we target (i) just the superfluid ground state $\big|\psi_0\big\rangle$ for $U_1 = 2$ (Fig. 2.6), (ii) in addition to (i) also the Mott-insulating ground state $\big|\psi_0'\big\rangle$ for $U_2 = 40$ and $\hat{H}(t > 0)\big|\psi_0\big\rangle$ (Fig. 2.7), (iii) in addition to (i) and (ii) also $\hat{H}(t > 0)^2\big|\psi_0\big\rangle$ and $\hat{H}(t > 0)^3\big|\psi_0\big\rangle$ (Fig. 2.8). Time evolution is calculated in the Crank-Nicolson

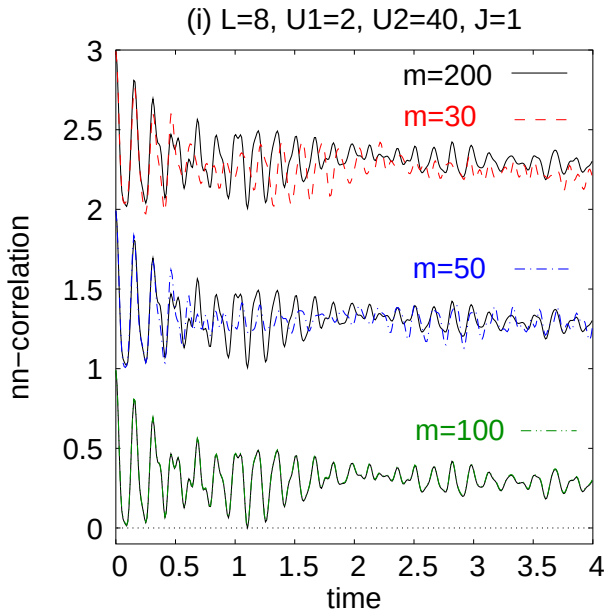

Figure 2.6.: Time evolution of the real part of the nearest-neighbour correlations in a Bose-Hubbard model ($L = 8$, $N = 8$) with instantaneous change of interaction strength at $t = 0$: superfluid state targeting only. The different curves for different m have been shifted by one.

approach using a step width $\mathrm{d}t = 5 \cdot 10^{-5}$. We keep up to $m = 200$ states to obtain converged results (meaning that we could observe no difference between the results for $m = 100$ and $m = 200$) for $t \leq 4$, corresponding to roughly 25 oscillations. The results for the cases (ii) and (iii) are almost converged for $m = 50$, whereas (i) shows still crude deviations.

A remarkable observation can be made if one compares the three $m = 200$ curves (Fig. 2.9), which by standard DMRG procedure (and for lack of a better criterion) would be considered the final, converged outcome, both amongst each other or to the result of the new adaptive t-DMRG algorithm which is discussed below: result (i) is clearly *not* quantitatively correct beyond very short times, whereas result (ii) agrees very well with the new algorithm, and result (iii) agrees almost (beside some small deviations at $t \approx 3$) with result (ii) and the new algorithm. Therefore we see that for case (i) the criterion of convergence in m does not give a good control to determine if the obtained results are correct. This raises as well doubts about the reliability of this criterion for cases (ii) and (iii).

The observation that even relatively robust numerical quantities such as nearest-neighbour correlations can be qualitatively and quantitatively improved by the additional targeting of states which merely share some fundamental characteristics with the true quantum state (as we will never reach the Mott-insulating ground state) or characterize only the very short-term time evolution indicates that it would be highly desirable to have a modified DMRG algorithm which, for each time t, selects Hilbert spaces of dimension m such that $\left|\psi(t)\right\rangle$ is represented optimally in the DMRG sense [compare Fig. 2.5 (c)], thus attaining at

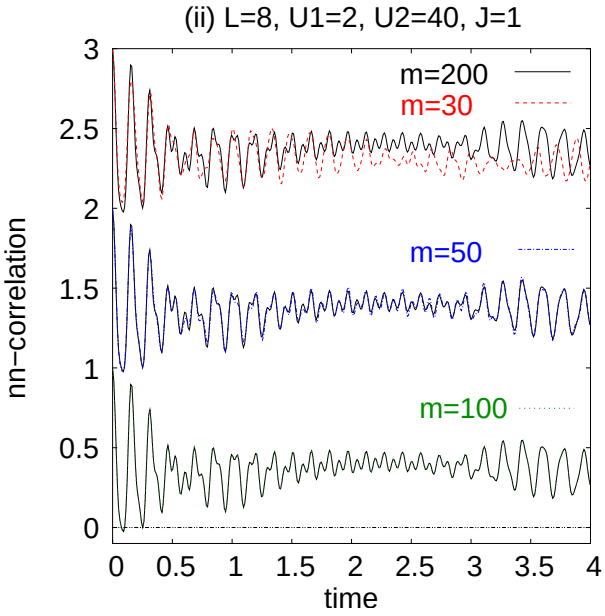

Figure 2.7.: Time evolution of the real part of the nearest-neighbour correlations in a Bose-Hubbard model with instantaneous change of interaction strength at $t = 0$: targeting of the initial superfluid ground state, Mott-insulating ground state and *one* additional state (see text). The different curves for different m have been shifted by one.

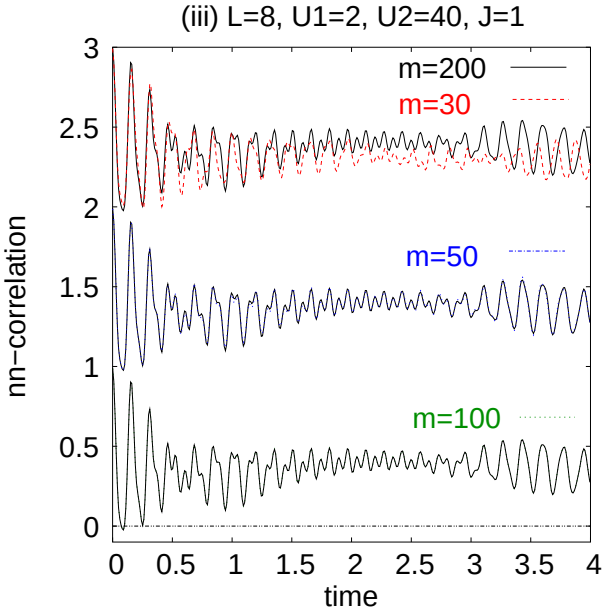

Figure 2.8.: Time evolution of the real part of the nearest-neighbour correlations in a Bose-Hubbard model with instantaneous change of interaction strength at $t = 0$: targeting of the initial superfluid ground state, Mott-insulating ground state and *three* additional states (see text). The different curves for different m have been shifted by one.

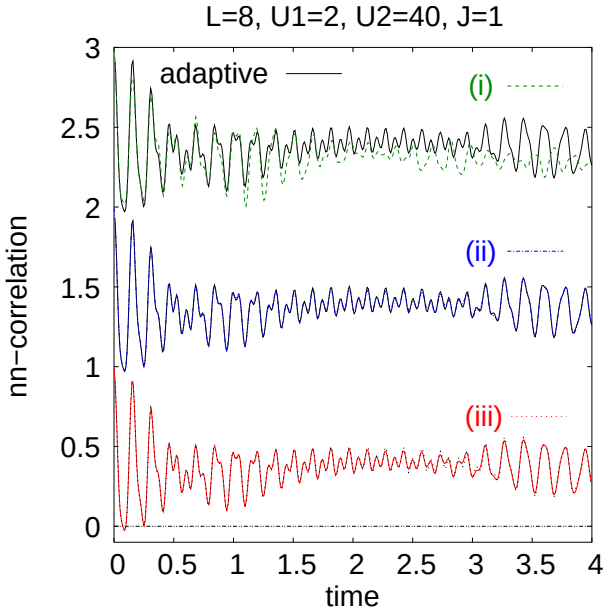

Figure 2.9.: Comparison of the three $m = 200$ Crank-Nicolson calculations to adaptive t-DMRG at $m = 50$: we target (i) just the superfluid ground state $|\psi_0\rangle$ for $U_1 = 2$ (Fig. 2.6), (ii) in addition to (i) also the Mott-insulating ground state $|\psi_0'\rangle$ for $U_2 = 40$ and $\hat{H}(t > 0)|\psi_0\rangle$ (Fig. 2.7), (iii) in addition to (i) and (ii) also $\hat{H}(t > 0)^2|\psi_0\rangle$ and $\hat{H}(t > 0)^3|\psi_0\rangle$ (Fig. 2.8. The different curves have been shifted by one.

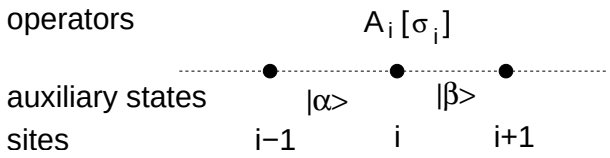

Figure 2.10.: Visualization the components of the matrix product states.

all times the typical DMRG precision for m retained states. The presentation of such an algorithm is the purpose of the following sections.

2.4. Matrix-product states

As both the TEBD simulation algorithm and DMRG can be neatly expressed in the language of matrix-product states, we briefly review the properties of these states also known as finitely-correlated states [20, 19].
Consider a one-dimensional system of size L, divided up into sites which each have a local Hilbert space, $\mathcal{H}_i$. For simplicity the same dimension N_{site} is taken at all sites. The Hilbert space $\mathcal{H}$ of the whole system is $\mathcal{H} = \otimes_{j=1}^{L}\mathcal{H}_j$, with dimension $(N_{\text{site}})^L$. We can express a general state of the whole system as

$$\begin{aligned} \big|\psi\big\rangle &= \sum_{\sigma_1,\ldots,\sigma_L} \psi_{\sigma_1,\ldots,\sigma_L}\big|\sigma_1\big\rangle \otimes \big|\sigma_2\big\rangle \otimes \ldots \otimes \big|\sigma_L\big\rangle \\ &\equiv \sum_{\boldsymbol{\sigma}} \psi_{\boldsymbol{\sigma}}\big|\boldsymbol{\sigma}\big\rangle, \end{aligned} \tag{2.4.0.7}$$

where $\big|\sigma_j\big\rangle$ denote the basis states on site j. A matrix-product state is now formed by only using a specific set of expansion coefficients $\psi_{\boldsymbol{\sigma}}$. This set is constructed in the following. To do this we define operators $\hat{A}_i[\sigma_i]$ which correspond to a local basis state $\big|\sigma_i\big\rangle$ at site i of the original system, but which act on auxiliary spaces of dimension m, i.e.,

$$\hat{A}_i[\sigma_i] = \sum_{\alpha,\beta} A^i_{\alpha\beta}[\sigma_i]\big|\alpha\big\rangle\big\langle\beta\big|, \tag{2.4.0.8}$$

where $\big|\alpha\big\rangle$ and $\big|\beta\big\rangle$ are orthonormal basis states in auxiliary spaces. There is no a priori significance to be attached to the states in the auxiliary state spaces. For visualization (Fig. 2.10), we imagine the auxiliary state spaces to be located on the bonds next to site i. If we label the bond linking sites i and $i+1$ by i, we say that the states $\big|\beta\big\rangle$ live on bond i and the states $\big|\alpha\big\rangle$ on bond $i-1$. The operators $\hat{A}_i[\sigma_i]$ hence act as transfer operators past site i depending on the local state on site i.
On the first and last site, which will need special attention later, this picture involves bond 0 to the left of site 1 and bond L to the right of site L respectively. These bonds have no physical meaning for open boundary conditions. They are identical and link sites 1 and L as one physical bond for periodic boundary conditions. In general, the operators $\hat{A}_i$ corresponding to different sites can be different. If this is the case the resulting matrix-product state to be introduced

is referred to as a position-dependent matrix-product state. We also impose the condition

$$\sum_{\sigma_i} \hat{A}_i[\sigma_i]\hat{A}_i^\dagger[\sigma_i] = \mathcal{I}, \tag{2.4.0.9}$$

which we will see to be related to orthonormality properties of bases later. An unnormalized matrix-product state in a form that will be found useful for Hamiltonians with open boundary conditions is now defined as

$$|\tilde{\psi}\rangle = \sum_{\boldsymbol{\sigma}} \left(\langle \phi_L | \prod_{i=1}^{L} \hat{A}_i[\sigma_i] | \phi_R \rangle \right) |\boldsymbol{\sigma}\rangle, \tag{2.4.0.10}$$

where $|\phi_L\rangle$ and $|\phi_R\rangle$ are the left and right boundary states in the auxiliary spaces on bonds 0 and L. They act on the product of the operators $\hat{A}_i$ to produce scalar coefficients

$$\tilde{\psi}_{\boldsymbol{\sigma}} = \langle \phi_L | \prod_{i=1}^{L} \hat{A}_i[\sigma_i] | \phi_R \rangle \tag{2.4.0.11}$$

for the expansion of $|\tilde{\psi}\rangle$ (compare Eq. 2.4.0.7).
Several remarks are in order. It should be emphasized that the set of states obeying Eq. (2.4.0.10) is an submanifold of the full boundary-condition independent Hilbert space of the quantum many-body problem on L sites that is hoped to yield good approximations to the true quantum states for Hamiltonians with open boundary conditions. If the dimension m of the auxiliary spaces is made sufficiently large then any general state of the system can, in principle, be represented exactly in this form (provided that $|\phi_L\rangle$ and $|\phi_R\rangle$ are chosen appropriately), simply because the $O(N_{\text{site}}Lm^2)$ degrees of freedom to choose the expansion coefficients will exceed N_{site}^L. This is, of course, purely academic. The practical relevance of the matrix-product states even for computationally manageable values of m is shown by the success of DMRG, which is known [36, 37] to produce matrix-product states of auxiliary state space dimension m, in determining energies and correlators at very high precision for moderate values of m. In fact, some very important quantum states in one dimension, such as the valence-bond-solid (VBS) ground state of the Affleck-Kennedy-Lieb-Tasaki (AKLT) model [38, 39, 40], can be described exactly by matrix product states using very small m ($m = 2$ for the AKLT model).
We now formulate a Schmidt decomposition for matrix-product states since we will use it later on. An unnormalized state $|\tilde{\psi}\rangle$ of the matrix-product form of Eq. (2.4.0.10) with auxiliary space dimension m can be written as

$$|\tilde{\psi}\rangle = \sum_{\alpha=1}^{m} |\tilde{w}_\alpha^S\rangle |\tilde{w}_\alpha^E\rangle, \tag{2.4.0.12}$$

where we have arbitrarily cut the chain into S on the left and E on the right with

$$|\tilde{w}_\alpha^S\rangle = \sum_{\{\boldsymbol{\sigma}^S\}} \left[\langle \phi_L | \prod_{i \in S} \hat{A}_i[\sigma_i] | \alpha \rangle \right] |\boldsymbol{\sigma}^S\rangle, \tag{2.4.0.13}$$

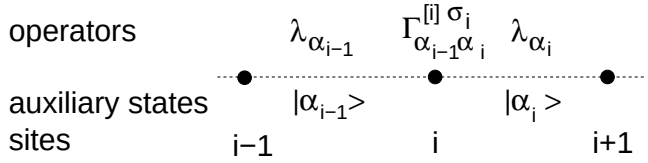

Figure 2.11.: Visualization the components of the states used in the TEBD algorithm.

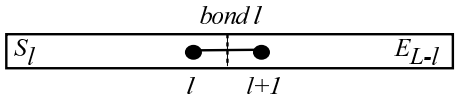

Figure 2.12.: Bipartitioning by cutting bond l between sites l and $l+1$.

and similarly $\big|\tilde{w}^E_\alpha\big\rangle$, where $\{\big|\alpha\big\rangle\}$ are the states spanning the auxiliary state space on the cut bond. Normalizing the states $\big|\tilde{\psi}\big\rangle$, $\big|\tilde{w}^S_\alpha\big\rangle$ and $\big|\tilde{w}^E_\alpha\big\rangle$ we obtain the representation

$$\big|\psi\big\rangle = \sum_{\alpha=1}^{m} \lambda_\alpha \big|w^S_\alpha\big\rangle \big|w^E_\alpha\big\rangle \tag{2.4.0.14}$$

where in λ_α the factors resulting from the normalization are absorbed. The relationship to reduced density-matrices is as detailed in section 2.6.

2.5. TEBD simulation algorithm

We now express the TEBD simulation algorithm in the language of the previous section. In the original exposition of the algorithm [18], one starts from a representation of a quantum state (Eq. 2.4.0.7) where the coefficients for the states are decomposed as a product of tensors,

$$\psi_{\sigma_1,\ldots,\sigma_L} = \sum_{\alpha_1,\ldots,\alpha_{L-1}} \Gamma^{[1]\sigma_1}_{\alpha_1} \lambda^{[1]}_{\alpha_1} \Gamma^{[2]\sigma_2}_{\alpha_1\alpha_2} \lambda^{[2]}_{\alpha_2} \Gamma^{[3]\sigma_3}_{\alpha_2\alpha_3} \cdots \Gamma^{[L]\sigma_L}_{\alpha_{L-1}}. \tag{2.5.0.15}$$

It is of no immediate concern to us how the Γ and λ tensors are constructed explicitly for a given physical situation. We assume here that they have been determined such that they approximate the true wave function close to the optimum obtainable within the class of wave functions having such coefficients. In fact, this can be done within the framework of DMRG, or by a continuous imaginary time evolution from some simple product state, as discussed in Ref. [5].

A visualization is attempted in the following (Fig. 2.11); the (diagonal) tensors $\lambda^{[i]}$, $i = 1,\ldots,L-1$ are associated with the bonds i, whereas $\Gamma^{[i]}$, $i = 2,\ldots,L-1$ links (transfers) from bond i to bond $i-1$ across site i. Note that at the boundaries ($i = 1, L$) the structure of the Γ is different. Each of the sums runs over m states $\big|\alpha_i\big\rangle$ living in auxiliary state spaces on bond i. A priori, these states have no physical meaning here.

The Γ and λ tensors are constructed such that for an arbitrary cut of the system into a part S_l of length l and a part E_{L-l} of length $L-l$ at bond l, the Schmidt decomposition for this bipartite splitting reads

$$|\psi\rangle = \sum_{\alpha_l} \lambda^{[l]}_{\alpha_l} |w^{S_l}_{\alpha_l}\rangle |w^{E_{L-l}}_{\alpha_l}\rangle, \tag{2.5.0.16}$$

with

$$|w^{S_l}_{\alpha_l}\rangle = \sum_{\alpha_1,\ldots,\alpha_{l-1}} \sum_{\sigma_1,\ldots,\sigma_l} \Gamma^{[1]\sigma_1}_{\alpha_1} \lambda^{[1]}_{\alpha_1} \cdots \Gamma^{[l]\sigma_l}_{\alpha_{l-1}\alpha_l} |\sigma_1\rangle \otimes \cdots \otimes |\sigma_l\rangle, \tag{2.5.0.17}$$

and

$$\begin{aligned} |w^{E_{L-l}}_{\alpha_l}\rangle &= \sum_{\alpha_{l+1},\ldots,\alpha_{L-1}} \sum_{\sigma_{l+1},\ldots,\sigma_L} \Gamma^{[l+1]\sigma_{l+1}}_{\alpha_l\alpha_{l+1}} \lambda^{[l+1]}_{\alpha_{l+1}} \cdots \Gamma^{[L]\sigma_L}_{\alpha_{L-1}} \times \\ & |\sigma_{l+1}\rangle \otimes \cdots \otimes |\sigma_L\rangle, \end{aligned} \tag{2.5.0.18}$$

where $|\psi\rangle$ is normalized and the sets of $\{|w^{S_l}_{\alpha_l}\rangle\}$ and $\{|w^{E_{L-l}}_{\alpha_l}\rangle\}$ are orthonormal. This implies, for example, that

$$\sum_{\alpha_l} (\lambda^{[l]}_{\alpha_l})^2 = 1. \tag{2.5.0.19}$$

We can see that (leaving aside normalization considerations for the moment) this representation may be expressed as a matrix-product state (compare Fig.2.10) if we choose for $\hat{A}_i[\sigma_i] = \sum_{\alpha,\beta} A^i_{\alpha\beta}[\sigma_i] |\alpha\rangle\langle\beta|$

$$A^i_{\alpha\beta}[\sigma_i] = \Gamma^{[i]\sigma_i}_{\alpha\beta} \lambda^{[i]}_{\beta}, \tag{2.5.0.20}$$

except for $i = 1$, where we choose

$$A^1_{\alpha\beta}[\sigma_1] = f_\alpha \Gamma^{[1]\sigma_1}_{\beta} \lambda^{[1]}_{\beta}, \tag{2.5.0.21}$$

and for $i = L$, where we choose

$$A^L_{\alpha\beta}[\sigma_L] = \Gamma^{[L]\sigma_L}_{\alpha} g_\beta. \tag{2.5.0.22}$$

The vectors f_α and g_β are normalized vectors which must be chosen in conjunction with the boundary states $|\phi_L\rangle$ and $|\phi_R\rangle$ so as to produce the expansion (2.5.0.15) from this choice of the $\hat{A}_i$. Specifically, we require

$$|\phi_L\rangle = \sum_\alpha f_\alpha |\alpha\rangle \tag{2.5.0.23}$$

$$|\phi_R\rangle = \sum_\beta g^*_\beta |\beta\rangle, \tag{2.5.0.24}$$

where $|\alpha\rangle$ and $|\beta\rangle$ are the states forming the same orthonormal basis in the auxiliary spaces on bonds 0 and L used to express $A^i_{\alpha\beta}$. In typical implementations of the algorithm it is common to take $f_\alpha = g_\alpha = \delta_{\alpha,1}$. Throughout the

rest of this section we take this as the definition for g_α and f_α, as this allows us to treat the operators on the boundary identically to the other operators. For the same reason we define a vector $\lambda_\alpha^{[0]} = \delta_{\alpha,1}$.
In the above expressions (2.5.0.17-2.5.0.22) we have grouped Γ and λ such that the λ reside on the *right* of the two bonds linked by Γ. There is another valid choice for the $\hat{A}_i$, which will produce identical states in the original system, and essentially the same procedure for the algorithm. If we set

$$\tilde{A}^i_{\alpha\beta}[\sigma_i] = \lambda_\alpha^{[i-1]}\Gamma^{[i]\sigma_i}_{\alpha\beta}, \tag{2.5.0.25}$$

except for $i = 1$, where we choose

$$\tilde{A}^1_{\alpha\beta}[\sigma_1] = f_\alpha\Gamma^{[1]\sigma_1}_{\beta}, \tag{2.5.0.26}$$

and for $i = L$, where we choose

$$\tilde{A}^L_{\alpha\beta}[\sigma_L] = \lambda_\alpha^{[L-1]}\Gamma^{[L]\sigma_L}_{\alpha}g_\beta, \tag{2.5.0.27}$$

then the same choice of boundary states produces the correct coefficients. Here we have grouped Γ and λ such that the λ reside on the *left* of the two bonds linked by Γ. It is also important to note that any valid choice of f_α and g_β that produces the expansion (2.5.0.15) specifically *excludes* the use of periodic boundary conditions. While generalizations are feasible, they will not be pursued here.
To conclude the identification of states, we consider normalization issues. The condition (2.4.0.9) is indeed fulfilled for our choice of $A_i[\sigma_i]$, because we have from (2.5.0.18) for a splitting at $l-1$ that

$$\begin{aligned} \big|w_{\alpha_{l-1}}^{E_{L-(l-1)}}\big\rangle &= \sum_{\alpha_l\sigma_l}\Gamma^{[l]\sigma_l}_{\alpha_{l-1}\alpha_l}\lambda^{[l]}_{\alpha_l}\big|\sigma_l\big\rangle\otimes\big|w_{\alpha_l}^{E_{L-l}}\big\rangle \\ &= \sum_{\alpha_l\sigma_l}A^l_{\alpha_{l-1}\alpha_l}[\sigma_l]\big|\sigma_l\big\rangle\otimes\big|w_{\alpha_l}^{E_{L-l}}\big\rangle, \end{aligned} \tag{2.5.0.28}$$

so that from the orthonormality of the sets of states $\{\big|w_\alpha^{E_{L-(l-1)}}\big\rangle\}_{\alpha=1}^m$, $\{\big|\sigma_l\big\rangle\}_{\sigma_l=1}^{N_{\text{site}}}$ and $\{\big|w_\gamma^{E_{L-l}}\big\rangle\}_{\gamma=1}^m$,

$$\begin{aligned} \sum_{\sigma_l}\hat{A}_l[\sigma_l]\hat{A}_l^\dagger[\sigma_l] &= \sum_{\alpha\beta\gamma}\sum_{\sigma_l}A^l_{\alpha\gamma}[\sigma_l](A^l_{\beta\gamma}[\sigma_l])^*\big|\alpha\big\rangle\big\langle\beta\big| \\ &= \sum_{\alpha\beta}\big\langle w_\beta^{E_{L-(l-1)}}\big|w_\alpha^{E_{L-(l-1)}}\big\rangle\big|\alpha\big\rangle\big\langle\beta\big| \\ &= \sum_{\alpha\beta}\mathrm{d}_{\alpha\beta}\big|\alpha\big\rangle\big\langle\beta\big| = \mathcal{I}. \end{aligned} \tag{2.5.0.29}$$

After introducing the notation of matrix-product states we can now consider the time evolution for a typical (possibly time-dependent) Hamiltonian in strongly correlated systems that contains for simplicity only short-ranged interactions:

$$\hat{H} = \sum_{i\,\text{odd}}\hat{F}_{i,i+1} + \sum_{j\,\text{even}}\hat{G}_{j,j+1}, \tag{2.5.0.30}$$

$F_{i,i+1}$ and $G_{j,j+1}$ are the local Hamiltonians on the odd bonds linking i and $i+1$, and the even bonds linking j and $j+1$. While all F and G terms commute among each other, F and G terms do in general not commute if they share one site. The time evolution operator for a time step $\mathrm{d}t$ may be approximately represented by a (first order) Suzuki-Trotter expansion as

$$\mathrm{e}^{-\mathrm{i}\hat{H}\mathrm{d}t} = \prod_{i\ \mathrm{odd}} \mathrm{e}^{-\mathrm{i}\hat{F}_{i,i+1}\mathrm{d}t} \prod_{j\ \mathrm{even}} \mathrm{e}^{-\mathrm{i}\hat{G}_{j,j+1}\mathrm{d}t} + \mathcal{O}(\mathrm{d}t^2), \tag{2.5.0.31}$$

and the time evolution of the state can be computed by repeated application of the two-site time evolution operators $\exp(-\mathrm{i}\hat{G}_{j,j+1}\mathrm{d}t)$ and $\exp(-\mathrm{i}\hat{F}_{i,i+1}\mathrm{d}t)$. This is a well-known procedure in particular in Quantum Monte Carlo [41] where it serves to carry out imaginary time evolutions (checkerboard decomposition). The TEBD simulation algorithm now runs as follows [5, 18]:

1. Perform the following two steps for all even bonds (order does not matter):
   (i) Apply $\exp(-\mathrm{i}\hat{G}_{l,l+1}\mathrm{d}t)$ to $\big|\psi(t)\big\rangle$. For each local time update, a new wave function is obtained. The number of degrees of freedom on the "active" bond thereby increases, as will be detailed below.
   (ii) Carry out a Schmidt decomposition cutting this bond and retain as in DMRG only those m degrees of freedom with the highest weight in the decomposition.
2. Repeat this two-step procedure for all *odd* bonds, applying $\exp(-\mathrm{i}\hat{F}_{l,l+1}\mathrm{d}t)$.
3. This completes one Suzuki-Trotter time step. One may now evaluate expectation values at selected time steps, and continue the algorithm from step 1.

After sketching the procedure we now consider its computational details.
(i) Consider a local time evolution operator acting on bond l, i.e. sites l and $l+1$, for a state $\big|\psi\big\rangle$. The Schmidt decomposition of $\big|\psi\big\rangle$ after partitioning by cutting bond l reads

$$\big|\psi\big\rangle = \sum_{\alpha_l=1}^{m} \lambda_{\alpha_l}^{[l]} \big|w_{\alpha_l}^{S_l}\big\rangle \big|w_{\alpha_l}^{E_{L-l}}\big\rangle. \tag{2.5.0.32}$$

Using Eqs. (2.5.0.17), (2.5.0.18) and (2.5.0.28), we find

$$\begin{aligned} \big|\psi\big\rangle \;=\; & \sum_{\alpha_{l-1}\alpha_l\alpha_{l+1}} \sum_{\sigma_l\sigma_{l+1}} \lambda_{\alpha_{l-1}}^{[l-1]} A^{l}_{\alpha_{l-1}\alpha_l}[\sigma_l] A^{l+1}_{\alpha_l\alpha_{l+1}}[\sigma_{l+1}] \times \\ & \big|w_{\alpha_{l-1}}^{S_{l-1}}\big\rangle \big|\sigma_l\big\rangle \big|\sigma_{l+1}\big\rangle \big|w_{\alpha_{l+1}}^{E_{L-(l+1)}}\big\rangle. \end{aligned} \tag{2.5.0.33}$$

We note, that if we identify $\big|w_{\alpha_{l-1}}^{S_{l-1}}\big\rangle$ and $\big|w_{\alpha_{l+1}}^{E_{L-(l+1)}}\big\rangle$ with DMRG system and environment block states $\big|w_{m_{l-1}}^{S}\big\rangle$ and $\big|w_{m_{l+1}}^{E}\big\rangle$, we have a typical DMRG state for two blocks and two sites

$$\big|\psi\big\rangle = \sum_{m_{l-1}} \sum_{\sigma_l} \sum_{\sigma_{l+1}} \sum_{m_{l+1}} \psi_{m_{l-1}\sigma_l\sigma_{l+1}m_{l+1}} \big|w_{m_{l-1}}^{S}\big\rangle \big|\sigma_l\big\rangle \big|\sigma_{l+1}\big\rangle \big|w_{m_{l+1}}^{E}\big\rangle \tag{2.5.0.34}$$

with

$$\psi_{m_{l-1}\sigma_l\sigma_{l+1}m_{l+1}} = \sum_{\alpha_l} \lambda^{[l-1]}_{m_{l-1}} A^l_{m_{l-1}\alpha_l}[\sigma_l] A^{l+1}_{\alpha_l m_{l+1}}[\sigma_{l+1}]. \tag{2.5.0.35}$$

The local time evolution operator on site $l, l+1$ can be expanded as

$$\hat{U}_{l,l+1} = \sum_{\sigma_l\sigma_{l+1}} \sum_{\sigma'_l\sigma'_{l+1}} U^{\sigma'_l\sigma'_{l+1}}_{\sigma_l\sigma_{l+1}} \big|\sigma'_l\sigma'_{l+1}\big\rangle\big\langle\sigma_l\sigma_{l+1}\big| \tag{2.5.0.36}$$

and generates $\big|\psi'\big\rangle = \hat{U}_{l,l+1}\big|\psi\big\rangle$, where

$$\begin{aligned}\big|\psi'\big\rangle \;=\; & \sum_{\alpha_{l-1}\alpha_l\alpha_{l+1}} \sum_{\sigma_l\sigma_{l+1}} \sum_{\sigma'_l\sigma'_{l+1}} \\ & \lambda^{[l-1]}_{\alpha_{l-1}} A^l_{\alpha_{l-1}\alpha_l}[\sigma'_l] A^{l+1}_{\alpha_l\alpha_{l+1}}[\sigma'_{l+1}] U^{\sigma_l\sigma_{l+1}}_{\sigma'_l\sigma'_{l+1}} \big|w^{S_{l-1}}_{\alpha_{l-1}}\big\rangle\big|\sigma_l\big\rangle\big|\sigma_{l+1}\big\rangle\big|w^{E_{L-(l+1)}}_{\alpha_{l+1}}\big\rangle.\end{aligned}$$

This can also be written as

$$\big|\psi'\big\rangle = \sum_{\alpha_{l-1}\alpha_{l+1}} \sum_{\sigma_l\sigma_{l+1}} \Theta^{\sigma_l\sigma_{l+1}}_{\alpha_{l-1}\alpha_{l+1}} \big|w^{S_{l-1}}_{\alpha_{l-1}}\big\rangle\big|\sigma_l\big\rangle\big|\sigma_{l+1}\big\rangle\big|w^{E_{L-(l+1)}}_{\alpha_{l+1}}\big\rangle, \tag{2.5.0.37}$$

where

$$\Theta^{\sigma_l\sigma_{l+1}}_{\alpha_{l-1}\alpha_{l+1}} = \lambda^{[l-1]}_{\alpha_{l-1}} \sum_{\alpha_l\sigma'_l\sigma'_{l+1}} A^l_{\alpha_{l-1}\alpha_l}[\sigma'_l] A^{l+1}_{\alpha_l\alpha_{l+1}}[\sigma'_{l+1}] U^{\sigma_l\sigma_{l+1}}_{\sigma'_l\sigma'_{l+1}}. \tag{2.5.0.38}$$

(ii) Now a *new* Schmidt decomposition identical to that in DMRG can be carried out for $\big|\psi'\big\rangle$: cutting once again bond l, there are now mN_{site} states in each part of the system, leading to

$$\big|\psi'\big\rangle = \sum_{\alpha_l=1}^{mN_{\text{site}}} \tilde{\lambda}^{[l]}_{\alpha_l} \big|\tilde{w}^{S_l}_{\alpha_l}\big\rangle\big|\tilde{w}^{E_{L-l}}_{\alpha_l}\big\rangle. \tag{2.5.0.39}$$

In general the states and coefficients of the decomposition will have changed compared to the decomposition (2.5.0.32) previous to the time evolution, which means that the reduced Hilbert space has been *adapted* to the quantum state at this time [compare Fig. 2.5 (c)]. We indicate this by introducing a tilde for these states and coefficients. As in DMRG, if there are more than m non-zero eigenvalues, we now choose the m eigenvectors corresponding to the largest $\tilde{\lambda}^{[l]}_{\alpha_l}$ to use in these expressions. The error in the final state produced as a result is proportional to the sum of the magnitudes of the discarded eigenvalues. After normalization, to allow for the discarded weight, the state reads

$$\big|\psi'\big\rangle = \sum_{\alpha_l=1}^{m} \lambda^{[l]}_{\alpha_l} \big|w^{S_l}_{\alpha_l}\big\rangle\big|w^{E_{L-l}}_{\alpha_l}\big\rangle. \tag{2.5.0.40}$$

Note again that the states and coefficients in this superposition are in general different from those in Eq. (2.5.0.32); we have now dropped the tildes again, as

this superposition will be the starting point for the next time evolution (state adaption) step.
To obtain the Schmidt decomposition reduced density-matrices are formed, e.g.

$$\begin{aligned}\hat{\rho}_E &= \mathrm{Tr}_S |\psi'\rangle\langle\psi'| \\ &= \sum_{\sigma_{l+1}\sigma'_{l+1}\alpha_{l+1}\alpha'_{l+1}} |\sigma_{l+1}\rangle|w_{\alpha_{l+1}}\rangle\langle w_{\alpha'_{l+1}}|\langle\sigma'_{l+1}| \\ &\quad \times \left(\sum_{\alpha_{l-1}\sigma_l} \Theta^{\sigma_l\sigma_{l+1}}_{\alpha_{l-1}\alpha_{l+1}} \left(\Theta^{\sigma_l\sigma'_{l+1}}_{\alpha_{l-1}\alpha'_{l+1}}\right)^* \right). \end{aligned} \tag{2.5.0.41}$$

If we now diagonalize $\hat{\rho}_E$, we can read off the new values of $A^{l+1}_{\alpha_l\alpha_{l+1}}[\sigma_{l+1}]$ because the eigenvectors $|w^{E_{L-l}}_{\alpha_l}\rangle$ obey

$$|w^{E_{L-l}}_{\alpha_l}\rangle = \sum_{\sigma_{l+1}\alpha_{l+1}} A^{l+1}_{\alpha_l\alpha_{l+1}}[\sigma_{l+1}]|\sigma_{l+1}\rangle|w^{E_{L-(l+1)}}_{\alpha_{l+1}}\rangle. \tag{2.5.0.42}$$

We also obtain the eigenvalues, $(\lambda^{[l]}_{\alpha_l})^2$. Due to the asymmetric grouping of Γ and λ into A discussed above, a short calculation shows that the new values for $A^l_{\alpha_{l-1}\alpha_l}[\sigma_l]$ can be read off from the slightly more complicated expression

$$\lambda^{[l]}_{\alpha_l}|w^{S_l}_{\alpha_l}\rangle = \sum_{\alpha_{l-1}\sigma_l} \lambda^{[l-1]}_{\alpha_{l-1}} A^l_{\alpha_{l-1}\alpha_l}[\sigma_l]|w^{S_{l-1}}_{\alpha_{l-1}}\rangle|\sigma_l\rangle. \tag{2.5.0.43}$$

The states $|w^{S_l}_{\alpha_l}\rangle$ are the normalized eigenvectors of $\hat{\rho}_S$ formed in analogy to $\hat{\rho}_E$.
The key point about the TEBD simulation algorithm is that a DMRG-style truncation keeping the most relevant density-matrix eigenstates (or the maximum amount of entanglement) is carried out for each local update *at each time step.* This is in contrast with time-dependent DMRG methods described in section 2.3, where the basis states were chosen before the time evolution is performed, and did not "adapt" to optimally represent the time-evolved state.

2.6. DMRG and matrix-product states

Typical normalized DMRG states for the combination of two blocks S and E and two single sites (Fig. 2.13) have the form

$$|\psi\rangle = \sum_{m_{l-1}}\sum_{\sigma_l}\sum_{\sigma_{l+1}}\sum_{m_{l+1}} \psi_{m_{l-1}\sigma_l\sigma_{l+1}m_{l+1}}|w^S_{m_{l-1}}\rangle|\sigma_l\rangle|\sigma_{l+1}\rangle|w^E_{m_{l+1}}\rangle \tag{2.6.0.44}$$

which can be Schmidt decomposed as

$$|\psi\rangle = \sum_{m_l} \lambda^{[l]}_{m_l}|w^S_{m_l}\rangle|w^E_{m_l}\rangle. \tag{2.6.0.45}$$

Figure 2.13.: Typical two-block two-site setup of DMRG as used here.

It has been known for some time [36, 37] that a DMRG calculation retaining m block states approximates $\big|\psi\big\rangle$ by $m \times m$ matrix-product states. Consider the reduced basis transformation to obtain the states of DMRG block S that terminates on bond l from those of the block terminating on bond $l-1$ and those on a single site l,

$$\langle w^S_{m_{l-1}} \sigma_l | w^S_{m_l} \rangle \equiv A^l_{m_{l-1} m_l}[\sigma_l], \tag{2.6.0.46}$$

such that

$$\big|w^S_{m_l}\big\rangle = \sum_{m_{l-1}\sigma_l} A^l_{m_{l-1}m_l}[\sigma_l] \big|w^S_{m_{l-1}}\big\rangle \otimes \big|\sigma_l\big\rangle. \tag{2.6.0.47}$$

The reduced basis transformation matrices $A^l[\sigma_l]$ automatically obey Eq. (2.4.0.9), which here ensures that $\{\big|w^S_{m_l}\big\rangle\}$ is an orthonormal set provided $\{\big|w^S_{m_{l-1}}\big\rangle\}$ is one. We may now use Eq. (2.6.0.47) for a backward recursion to express $\big|w^S_{m_{l-1}}\big\rangle$ via $\big|w^S_{m_{l-2}}\big\rangle$ and so forth. There is a complication as the number of block states for very short blocks is less than m. For simplicity, we assume that m is chosen such that we have exactly $N^{\tilde{N}}_{\text{site}} = m$. If we stop the recursion at the shortest block of size $\tilde{N}$ that has m states we obtain

$$\begin{aligned} \big|w^S_{m_l}\big\rangle \;=\; & \sum_{m_{\tilde{N}} \ldots m_{l-1}} \sum_{\sigma_1 \ldots \sigma_l} \\ & A^{\tilde{N}+1}_{m_{\tilde{N}} m_{\tilde{N}+1}}[\sigma_{\tilde{N}+1}] \ldots A^l_{m_{l-1}m_l}[\sigma_l] \big|\sigma_1 \ldots \sigma_l\big\rangle, \end{aligned} \tag{2.6.0.48}$$

where we have indexed the boundary-site states by $m_{\tilde{N}} \equiv \{\sigma_1 \ldots \sigma_{\tilde{N}}\}$ on the first $\tilde{N}$ sites. Similarly, for the DMRG block E we have

$$\langle w^E_{m_{l+1}} \sigma_{l+1} | w^E_{m_l} \rangle \equiv A^{l+1}_{m_l m_{l+1}}[\sigma_{l+1}], \tag{2.6.0.49}$$

such that (again having $\tilde{N}$ boundary sites) a recursion gives

$$\begin{aligned} \big|w^E_{m_l}\big\rangle \;=\; & \sum_{m_{l+1} \ldots m_{L-\tilde{N}}} \sum_{\sigma_{l+1} \ldots \sigma_L} \\ & A^{l+1}_{m_l m_{l+1}}[\sigma_{l+1}] \ldots A^{L-\tilde{N}}_{m_{L-\tilde{N}-1} m_{L-\tilde{N}}}[\sigma_{L-\tilde{N}}] \big|\sigma_{l+1} \ldots \sigma_L\big\rangle, \end{aligned} \tag{2.6.0.50}$$

where the boundary-site states are indexed by $m_{L-\tilde{N}} \equiv \{\sigma_{L-\tilde{N}+1} \ldots \sigma_L\}$ on the last $\tilde{N}$ sites. A comparison with Eqs. (2.4.0.10), (2.4.0.12) and (2.4.0.13) shows that DMRG generates position-dependent $m \times m$ matrix-product states as block states for a reduced Hilbert space of m states; the auxiliary state space to a bond is given by the Hilbert space of the block at whose end the bond sits. This physical meaning attached to the auxiliary state spaces and

the fact that for the shortest block the states can be labeled by good quantum numbers (if available) ensures through (2.6.0.46) and (2.6.0.49) that they carry good quantum numbers for *all* block sizes. The big advantage is that using good quantum numbers allows us to exclude a large amount of wave function coefficients as being 0, drastically speeding up all calculations by at least one, and often two orders of magnitude.
In this language the effect of the finite-system DMRG algorithm (see section 2.2.2) is to shift the two free sites through the chain, growing and shrinking the blocks S and E as illustrated in Fig. 2.4. At each step, the ground state is redetermined and a new Schmidt decomposition carried out in which the system is cut between the two free sites, leading to a new truncation and new reduced basis transformations (two matrices A adjacent to this bond). It is thus a sequence of *local* optimization steps of the wave function oriented towards an optimal representation of the ground state. Typically, after some "sweeps" of the free sites from left to right and back, physical quantities evaluated for this state converge. While comparison of DMRG results to exact results shows that one often comes extremely close to an optimal representation within the matrix state space (which justifies the usage of the DMRG algorithm to obtain them), it has been pointed out and numerically demonstrated [37, 42] that finite-system DMRG results can be further improved and better matrix-product states be produced by switching, after convergence is reached, from the S••E scheme (with two free sites) to an S•E scheme (with one free site) and to carry out some more sweeps. This point is not pursued further here, it just serves to illustrate that finite-system DMRG for all practical purposes comes close to an optimal matrix-product state, while not strictly reaching the optimum.
We will outline the calculation for shifting the active bond by one site to the left since it will be used in the adaptive t-DMRG.
Starting from the wavefunction represented in the S••E scheme,

$$|\psi\rangle = \sum_{m_{l-1}} \sum_{\sigma_l} \sum_{\sigma_{l+1}} \sum_{m_{l+1}} \psi_{m_{l-1}\sigma_l\sigma_{l+1}m_{l+1}} |w^S_{m_{l-1}}\rangle|\sigma_l\rangle|\sigma_{l+1}\rangle|w^E_{m_{l+1}}\rangle, \tag{2.6.0.51}$$

one inserts the identity $\sum_{m_l} |w^E_{m_l}\rangle\langle w^E_{m_l}|$ to obtain

$$|\psi\rangle = \sum_{m_{l-1}} \sum_{\sigma_l} \sum_{m_l} \psi_{m_{l-1}\sigma_l m_l} |w^S_{m_{l-1}}\rangle|\sigma_l\rangle|w^E_{m_l}\rangle, \tag{2.6.0.52}$$

where

$$\psi_{m_{l-1}\sigma_l m_l} = \sum_{m_{l+1}} \sum_{\sigma_{l+1}} \psi_{m_{l-1}\sigma_l\sigma_{l+1}m_{l+1}} A^{l+1}_{m_l m_{l+1}}[\sigma_{l+1}]. \tag{2.6.0.53}$$

After inserting in a second step the identity $\sum_{m_{l-2}\sigma_{l-1}} |w^S_{m_{l-2}}\sigma_{l-1}\rangle\langle w^S_{m_{l-2}}\sigma_{l-1}|$, one ends up with the wave function in the shifted bond representation:

$$|\psi\rangle = \sum_{m_{l-2}} \sum_{\sigma_{l-1}} \sum_{\sigma_l} \sum_{m_l} \psi_{m_{l-2}\sigma_{l-1}\sigma_l m_l} |w^S_{m_{l-2}}\rangle|\sigma_{l-1}\rangle|\sigma_l\rangle|w^E_{m_l}\rangle, \tag{2.6.0.54}$$

where

$$\psi_{m_{l-2}\sigma_{l-1}\sigma_l m_l} = \sum_{m_{l-1}} \psi_{m_{l-1}\sigma_l m_l} A^{l-1}_{m_{l-2}m_{l-1}}[\sigma_{l-1}]. \tag{2.6.0.55}$$

2.7. Adaptive t-DMRG

As the actual decomposition and truncation procedure in DMRG and the TEBD simulation algorithm are identical, the idea of the TEBD algorithm can be carried over to generalize the DMRG to give a very effective method, the adaptive t-DMRG, to study time-dependent phenomena in strongly correlated quasi-one dimensional systems. In the adaptive t-DMRG the finite-system algorithm is used to carry out the sequence of local time evolutions after the initial state has been determined. During each such a local time evolution the local evolution operator is applied to the wave function $|\psi\rangle$ in a two-block two-site configuration such that the bond that is currently updated consists of the two free sites. Then new block states — best adapted to a state at any given point in the time evolution (hence adaptive block states)— are constructed by Schmidt decomposition and truncation as in the TEBD algorithm, while maintaining the computational efficiency of DMRG. Then to apply the next local evolution operator the wave function $|\psi\rangle$ has to be transformed between different two-block two-site configurations. In finite-system DMRG such a transformation, which was first implemented by White [21] ("state prediction") is routinely used to predict the outcome of large sparse matrix diagonalizations, which no longer occur during time evolution. Here, it merely serves as a transformation to the reduced basis.
The adaptive t-DMRG algorithm using the first order Suzuki-Trotter decomposition which incorporates the TEBD simulation algorithm in the DMRG framework is now set up as follows:

0. Set up a conventional finite-system DMRG algorithm with state prediction using the Hamiltonian at time $t = 0$, $\hat{H}(0)$, to determine the ground state of some system of length L using effective block Hilbert spaces of dimension m. At the end of this stage of the algorithm, we have for blocks of all sizes l reduced orthonormal bases spanned by states $|m_l\rangle$, which are characterized by good quantum numbers. Also, we have all reduced basis transformations, corresponding to the matrices A.

1. For each Suzuki-Trotter time step, use the finite-system DMRG algorithm to run one sweep with the following modifications:

   i) For each even bond apply the local time evolution $\hat{U}$ at the bond formed by the free sites to $|\psi\rangle$. This is a very fast operation compared to determining the ground state, which is usually done instead in the finite-system algorithm.

   ii) As always, perform a DMRG truncation at each step of the finite-system algorithm, hence $O(L)$ times.

   (iii) Use White's prediction method to shift the free sites by two.

2. In the reverse direction, apply step (i) to all odd bonds.

3. As in standard finite-system DMRG evaluate operators when desired at the end of a time step. Note, that there is no need to generate these operators at all those time steps where no operator evaluation is desired.

The calculation time of adaptive t-DMRG scales linearly in L, as opposed to the non-adaptive time-dependent DMRG which only depends on L indirectly. The diagonalization of the density-matrices (Schmidt decomposition) scales as $N_{\text{site}}^3 m^3$; the preparation of the local time evolution operator as N_{site}^6, but this may have to be done only rarely e.g. for discontinuous changes of interaction parameters. Carrying out the local time evolution scales as $N_{\text{site}}^4 m^2$; the basis transformation scales as $N_{\text{site}}^2 m^3$. As $m \gg N_{\text{site}}$ typically, the algorithm is of order $O(L N_{\text{site}}^3 m^3)$ at each time step. In most cases a speeding up of the algorithm can be obtained using higher order Suzuki-Trotter decompositions given in appendix A. In the applications presented in this work the second-order and fourth-order Suzuki-Trotter decomposition are used.

2.8. Case study: time-dependent Bose-Hubbard model

Before we discuss the sources of error in the next section, we would like to compare the new adaptive algorithm to the non-adaptive methods described in section 2.3. To do this we present some results of calculations on the Bose-Hubbard Hamiltonian introduced in section 2.3 which have been carried out using modest computational resources and an unoptimized code (this concerns in particular the operations on complex matrices and vectors). In the following, Suzuki-Trotter time steps down to $\mathrm{d}t = 5 \times 10^{-4}$ in units of $1/J$ were chosen. Applications to systems of realistic size are shown in the following chapters. Comparing the results of the adaptive t-DMRG for the Bose-Hubbard model with the parameters chosen as in section 2.3 with the static time-dependent DMRG we find that the convergence in m of the adaptive algorithm is much faster than for the static algorithm. For the nearest neighbour correlations it sets in at about $m = 40$ (Fig. 2.14) for the adaptive algorithm compared to $m = 100$ for the static method (Fig. 2.6-2.8).

This faster convergence in m enables us to study larger systems than would be accessible with non-adaptive time-dependent DMRG (Fig. 2.15). In the $L = 32$ system considered here, we encountered severe convergence problems using non-adaptive time-dependent DMRG. By contrast, in the new approach convergence sets in for m well below 100, which is easily accessible numerically. Let us remark that the number m of states which have to be kept does certainly vary with the exact parameters chosen, depending on whether the state can be approximated well by matrix-product states of a low dimension. At least in the case studied here, we found that this dependence is quite weak. We expect (also from studying the time evolution of density-matrix spectra) that the system dependence of m is roughly similar as in the static case.

Similar observations are made both for local occupancy (a simpler quantity than nearest-neighbour correlations) and longer-ranged correlations (where we expect less precision). Moving back to the parameter set of section 2.3, we find as expected that the result for the local occupancy (Fig. 2.16) has converged for the same m leading to convergence in the nearest-neighbour correlations. In contrast, if we consider the correlation $\langle b^\dagger b \rangle$ between sites further apart from each other the numerical results converge more slowly under an increase of m

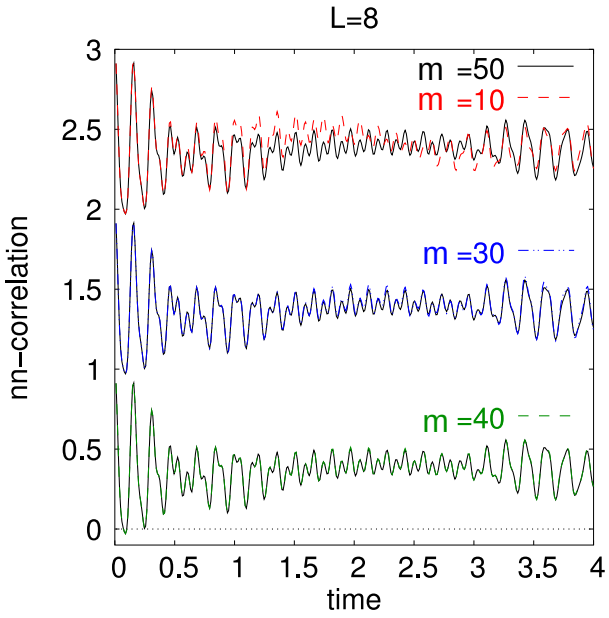

Figure 2.14.: Time evolution of the real part of nearest-neighbour correlations in a Bose-Hubbard model with instantaneous change of interaction strength using the adaptive t-DMRG. The different curves for different m are shifted by one (parameters as in section 2.3).

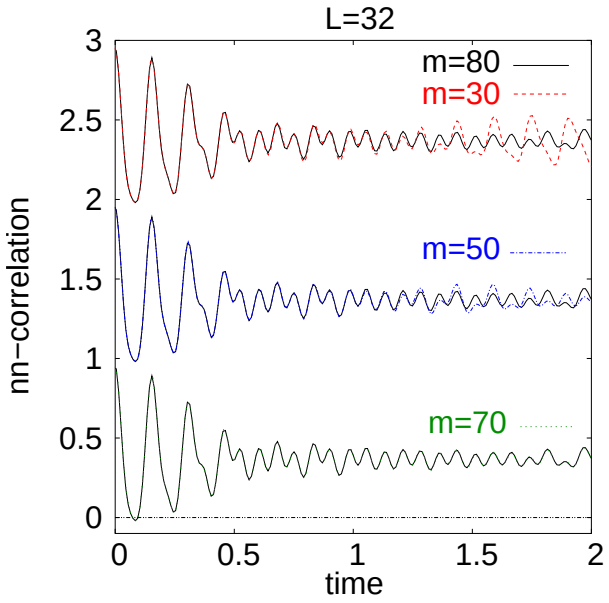

Figure 2.15.: Time evolution of the real part of nearest-neighbour correlations in a Bose-Hubbard model with instantaneous change of interaction strength using the adaptive t-DMRG but for a larger system $L = 32$ with $N = 32$ bosons and remaining parameters chosen as in section 2.3. The different curves for different m are shifted by one.

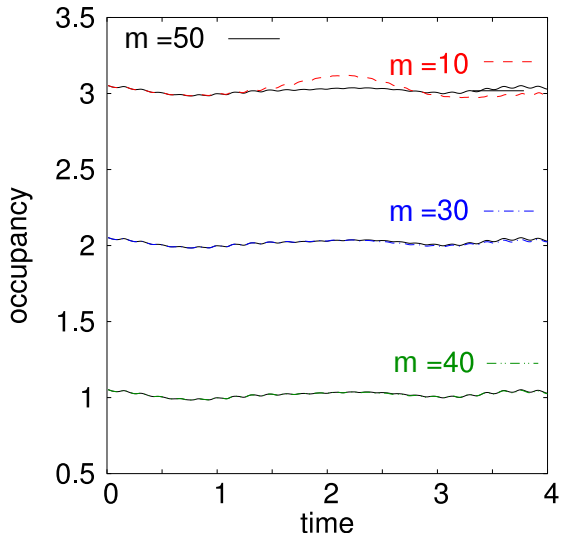

Figure 2.16.: Time evolution of the occupancy of the second site. Parameters as used in section 2.3 ($L = 8$, $N = 8$). The different curves for different m are shifted.

than the almost local quantities. This can be seen in Fig. 2.17 where the results for $m = 40$ and $m = 50$ still differ a bit for times larger than $t \approx 2/J$.

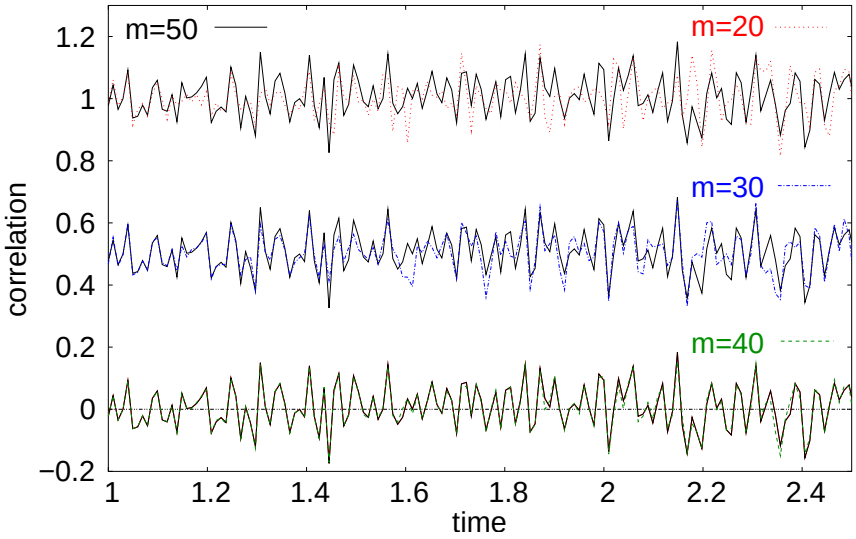

Figure 2.17.: Time evolution of the real part of the correlation between site 2 and 7. Parameters as used in section 2.3 with $N = 8$ particles. The different curves for different m are shifted. Note that the plot starts at $t = 1$ (parameters were changed at $t = 0$), since the different curves agree for $t = 0$ to $t = 1$.

2.9. Sources of error

After we have seen in the previous chapter that the developed algorithm performs very well in describing time-dependent phenomena, let us discuss here the approximations involved. Two main sources of error occur in the adaptive t-DMRG:
(i) The *Suzuki-Trotter error* due to the Suzuki-Trotter decomposition. For an nth-order Suzuki-Trotter decomposition [41], the error made in one time step $\mathrm{d}t$ is of order $\mathrm{d}t^{n+1}$. To reach a given time t one has to perform $t/\mathrm{d}t$ time-steps, such that in the worst case the error grows linearly in time t such that the resulting error is of order $(\mathrm{d}t)^n t$. In our setup of the Suzuki-Trotter decomposition, the error is expected to scale linearly with system size L for a generic state, and overall it is of order $(\mathrm{d}t)^n Lt$ for the times of interest. (Eventually, the error generally saturates at a finite value, as measured quantities are typically bound.)
(ii) The DMRG *truncation error* due to the representation of the time-evolving quantum state in reduced (albeit "optimally" chosen) Hilbert spaces and due to the repeated transformations between different truncated basis sets. While the truncation error ϵ that sets the scale of the error of the wave function and operators is typically very small, here it will strongly accumulate in time as $O(Lt/\mathrm{d}t)$ truncations are carried out up to time t. This is due to the fact that the truncated DMRG wave function has norm less than one and is renormalized at each truncation by a factor of $(1-\epsilon)^{-1} > 1$. Truncation errors should therefore accumulate roughly exponentially with an exponent of $\epsilon Lt/\mathrm{d}t$, such that eventually the adaptive t-DMRG will break down at too long times. A partial compensation of errors in observables may slow down the error growth. The accumulated truncation error should decrease considerably with an increasing number of kept DMRG states m. For a fixed time t, it should decrease as the Suzuki-Trotter time step $\mathrm{d}t$ is increased, since the number of truncations decreases with the number of time steps $t/\mathrm{d}t$.
At this point, it is worthwhile to mention that the error arising should also be pertinent to the very closely related time evolution algorithm introduced by Verstraete *et al.* [43], which differs from ours for the present purpose in one major point: In our algorithm a basis truncation is performed after each *local* application of $\hat{U}_{l,l+1}$. In their more time-consuming algorithm truncations are performed after all local time evolutions have been carried out, i.e. after a *global* time evolution using $\hat{U} = \prod_l \hat{U}_{l,l+1}$. In our iterative procedure, the wave function after such a full time evolution is not necessarily the *globally* optimal state representing the time-evolved state. However, for small $\mathrm{d}t$ the state update via the operators U_n is likely to be small. We expect the global optimum to be rather well approximated using the present algorithm, as seems to be borne out by direct comparisons between both approaches. Errors should therefore exhibit very similar behaviour.
A detailed error analysis of the influence of the Suzuki-Trotter error and the truncation error on the total error can be found in section 6.3, where we compare our DMRG results for the time evolution of an initial state in a spin-1/2 XX-model to exact results.

2.10. Conclusion

While exporting ideas from one field of knowledge to another may appear as an exciting and often fruitful enterprise, differences in language and background between researchers in so far separated fields can also often become a serious obstacle to the proper propagation and full assimilation of such ideas. In this chapter we have translated the TEBD algorithm into the language of matrix-product states. This language is a natural choice to express the DMRG algorithm – which, for over a decade, has dominated the simulation of one-dimensional quantum many-body systems. The translation of the TEBD algorithm to the DMRG language has made evident that the TEBD and the DMRG algorithms have a number of common features, a fact that was exploited in developing the new method presented here. We have performed the corresponding modification of existing finite-system DMRG codes to incorporate the TEBD leading to the new adaptive t-DMRG algorithm. Even without attempting to reach the computationally most efficient incorporation of the TEBD algorithm into DMRG implementations, the resulting code seems to perform systematically better than non-adaptive time-dependent DMRG codes at very reasonable numerical cost. The adaptive t-DMRG converges for much smaller state spaces, as they are adapted in time to track the actual state of the evolving system. The new code by application of existing conceptual ideas, is significantly more efficient than other existing embodiments of the TEBD, for instance thanks to the way DMRG exploits good quantum numbers.
While we have considered bosons in the example, also fermionic (see chapter 5) and spin (see chapter 6) systems present no fundamental difficulties. Some interesting topics which are best approached with the adaptive t-DMRG are presented in the following chapters to show the efficiency of the developed adaptive t-DMRG. In chapter 4 the evolution of a perturbation in a bosonic system, in chapter 5 the spin-charge separation in one-dimensional fermionic systems with two species, and in chapter 6 a simplified model for spin transport between two spin polarized reservoirs are discussed.

3. Ultracold atoms in optical lattices

3.1. From Bose-Einstein condensation to strongly interacting Bose gases

In 1995, the first experimental realizations of a Bose-Einstein condensation (BEC) were achieved in rubidium [8], sodium [9] and lithium vapors [10]. This was long after the theoretical prediction of this effect by Einstein 1924, who investigated the ideal Bose gas based on the statistics introduced by Bose. The main problem in the experimental realization of Bose-Einstein condensation was that the cloud of atoms had to be cooled to ultra low temperatures in the nano-Kelvin regime. To reach these low temperatures became possible only after the development of laser and evaporative cooling techniques. In a Bose-Einstein condensate a macroscopic number of bosonic atoms collectively occupies the lowest energy state. Therefore, the Bose-Einstein condensates provide the possibility to explore quantum phenomena on a macroscopic scale. Examples are the interference between two condensates [44] or collective modes [45]. In a Bose-Einstein condensate the ratio between the interaction energy between the atoms and their kinetic energy is usually very low, of the order of $\frac{E_{\text{int}}}{E_{\text{kin}}} \approx 0.02$, and the theoretical description [12] of many properties is well understood in the framework of the Gross-Pitaevskii and Bogoliubov theories. From the viewpoint of many-particle physics the regime in which the interplay between the interaction and the kinetic energy becomes important is even more interesting than the weakly interacting regime. Fascinating many-body effects like the quantum phase transition between a superfluid and a Mott-insulting state occur. In this regime the Bose gas cannot be described by the Gross-Pitaevskii theory anymore, since correlations between the atoms induced by their interaction have to be taken into account. To reach this regime the interaction energy per atom has to be at least on the same order or larger than their kinetic energy. Experimentally this can be achieved either by increasing the interaction energy or by further lowering the kinetic energy. Since bosons usually interact via s-wave scattering, one way to achieve a strong coupling regime by increasing the interaction energy is to tune their s-wave scattering length to large values using a Feshbach resonance [11]. In ^{85}Rb for example the scattering length has been tuned over several orders of magnitude and collapse and explosion of the condensate have been observed [13, 14]. The problem with increasing the interaction to reach the strong coupling regime is that as the interaction increases the three-body loss rate becomes very large and the lifetime of the Bose cloud decreases drastically. The complementary approach was pursued in the experiments of Orzel et al. [15] and Greiner et al. [1]. Instead of increasing the interaction energy the kinetic energy of the atoms is lowered

to achieve a high ratio of the interaction to the kinetic energy. The quenching of the kinetic energy is realized by loading the Bose-Einstein condensate into an optical lattice potential. The condensate is split up into separated lattice sites and the motion of the atoms is frozen except for tunneling between neighbouring sites. In this setup the kinetic energy of the atoms can be varied over several orders of magnitude by tuning the height of the optical lattice potential and therewith changing the tunneling probability. Hence, the regime of strong coupling is reached without the problem of destabilizing the atom cloud by increasing the three-body loss rate. This opens up the possibility to investigate many problems from condensed matter physics in a new context. The advantage of the system of ultracold atoms in a lattice compared to condensed matter systems is its better tunability, in particular the rapid control of parameters in time by which a whole area of new non-equilibrium phenomena can be explored. Before we discuss some of these fascinating time-dependent phenomena in chapter 4-5, we start here by investigating static properties of ultracold bosons in an optical lattice. In the experiment of Greiner et al. [1] the quantum phase transition between a Mott-insulating and superfluid state was realized experimentally. However when analysing these experiments in contrast to condensed matter systems the presence of a parabolic trapping potential must be taken into account. This harmonic trapping potential causes a state in which the two phases coexist [46], though spatially separated. Due to this inhomogeneity of the system the usual characterization of the superfluid and the Mott-insulating phase by the asymptotic behaviour of the one-particle density-matrix does not apply here. The following sections are devoted to analyse the observed phase transition and in particular to establish a characteristic to distinguish the arising states experimentally.
We start in section 3.2 by introducing the theoretical description of the systems of ultracold atoms in an optical lattice by the Bose-Hubbard model. In section 3.3 we discuss the characteristics of the quantum phase transition in a homogeneous system. In section 3.4 coexistence between different phases in the harmonic trapping potential is shown. The application of the finite-system DMRG to such a system with parabolic confinement is not straightforward. In section 3.5 we point out the problems arising and how we overcome these. We discuss in section 3.6 the behaviour of the one-particle density-matrix in the system with a parabolic confinement in order to recover a characteristic for the different states and to test the results of the hydrodynamical approach. Finally in section 3.7, we present results for the Fourier transform of the one-particle density-matrix —the experimentally most accessible quantity— for both the system with and without parabolic potential and study the information it contains.

3.2. Theoretical description: Bose-Hubbard model

Optical lattice potentials have nowadays been used in various experiments with cold atoms (see [47] and references therein). These periodic structures can be achieved using standing wave interference pattern of two counter propagating laser beams. The atoms in such a system can be trapped in the intensity maxima or minima of the off-resonance light field via the optical dipole force (for details see appendix B and [48, 49]). In the experiments [1, 50] simple cubic lattices were created by superimposing three standing waves orthogonal to each other. The laser beams used were far red detuned. Additionally to the periodic potential, the Gaussian intensity profile of the red-detuned lasers create a trapping potential.

Let us discuss in the following how these systems can be described theoretically. Ultracold bosons with repulsive s-wave interaction can be described by the Hamiltonian

$$
\begin{aligned}
(3.2.0.1) \qquad H &= \int \mathrm{d}^3x\, \Psi^\dagger(x) \left(p^2 + V_{\mathrm{ext}}\right) \Psi(x) \\
&+ \frac{1}{2} \underbrace{\frac{4\pi a_s \hbar}{M}}_{=:g} \int \mathrm{d}^3x\, \Psi^\dagger(x)\Psi^\dagger(x)\Psi(x)\Psi(x).
\end{aligned}
$$

Here $\Psi(x)$ is the bosonic field operator for the atoms and M their mass. The first term contains the kinetic energy and the contribution of external potentials V_{ext}, like for example the lattice and trapping potentials. The second term originates from the interaction of the bosons with each other. In the case of ultracold bosons it is mostly well approximated by an isotropic short-range pseudopotential and its strength is proportional to the s-wave scattering length a_s. In the dilute gases without the lattice potential the ratio of the interaction energy and the kinetic energy is typically around $\gamma := \frac{E_{\mathrm{int}}}{E_{\mathrm{kin}}} \approx 0.02$, i.e. the Bose gases are only weakly interacting.

The presence of a periodic potential V_{lat} changes the situation drastically. The kinetic energy of the atoms is quenched, since their motion is frozen and only tunneling between neighbouring sites is possible. The ratio between the interaction energy and the kinetic energy increases by an immense amount which makes the strong coupling regime experimentally accessible (see [47, 51] and references therein).

In the case of a periodic potential an energy band structure emerges (appendix B.3.1) in which the gap between the lowest lying energy bands becomes larger as the lattice depth increases. At some lattice depth the energies involved in the dynamic of the system are smaller than this gap and the motion of the atoms is confined to the lowest energy band. In this regime it is favorable to work in the basis of Wannier functions w_0 of the lowest band neglecting higher bands. The Wannier functions are a set of orthonormal wave functions maximally localized at the lattice sites (appendix B.3.1). The bosonic field operators can be expanded in this basis and the continuous Hamiltonian (3.2.0.1) reduces to the

Bose-Hubbard Hamiltonian (see appendix B.3.2 for a derivation):

$$H = -\sum_j J_j(b_j^\dagger b_{j+1} + h.c.) + \frac{1}{2}\sum_j U_j \hat{n}_j(\hat{n}_j - 1) + \sum_j(-\mu + \varepsilon_j)\hat{n}_j, \tag{3.2.0.2}$$

where $b_j^\dagger$ and b_j are the bosonic creation and annihilation operators and $\hat{n}_j = b_j^\dagger b_j$ is the number operator on site j. The first term, the hopping term, describes the kinetic energy, the second term the interaction energy, and the third term models the chemical potential μ and external potential ε. This Hamiltonian is the simplest lattice Hamiltonian describing the interplay between the kinetic energy, which delocalizes the bosons, and the onsite interaction of the atoms, which has a localizing effect. At commensurate filling this interplay leads to a quantum phase transition between a superfluid and a Mott-insulating phase at some critical value $(U/J)_c =: u_c$ [52]. We discuss the properties of the phases in more detail below.
The Bose-Hubbard model was first considered in the seminal paper by Fisher et al. [52] in the context of condensed matter physics. It has been used in that area, for example, to study the adsorption of noble gases in nanotubes [53], or Cooper pairs in superconducting films with strong charging effects [54, 55, 56, 57].
In the systems of ultracold bosonic atoms the parameter J can be related to the height V_0 of the lattice potential for $V_0 \gg E_r$, $E_r = \frac{\hbar^2 k^2}{2M}$ is the recoil energy, (see appendix B.3.2, [51]) by

$$J/E_r \approx \frac{4}{\sqrt{\pi}}\left(\frac{V_0}{E_r}\right)^{\frac{3}{4}} \exp(-2\sqrt{V_0/E_r}). \tag{3.2.0.3}$$

Furthermore, in the same limit the interaction strength U can be approximated using a Gaussian form for the Wannier functions to obtain (see appendix B.3.2, [51])

$$U/E_r = \sqrt{\frac{8}{\pi}} k a_s \left(\frac{V_0}{E_r}\right)^{3/4}. \tag{3.2.0.4}$$

Although in a separable periodic potential the Wannier functions decay exponentially in all directions rather than in a Gaussian manner, the approximation is justified since one is mainly interested in the quotient $u := U/J$ and J varies exponentially with the lattice height, such that the small error introduced by taking Gaussian form for the wave function does not matter much.
In Fig. 3.1 the numerically determined exact dependence of the ratio u on the lattice height is shown for an isotropic three-dimensional lattice (dashed curve). If the optical lattice is very high in one or two dimensions, quasi-two and quasi-one dimensional systems can be experimentally realized [58, 59]. In Fig. 3.1 as well the numerically determined dependence of the ratio u for a lattice with a strong anisotropy in one direction is plotted (solid curve, marked 1d). The calculations show an exponential dependence between the experimental and theoretical parameters, the lattice height V_0 and the interaction parameter u which stems from the strong quenching of the kinetic energy by

the periodic potential. Due to this exponential dependence, the parameter u can be varied over several orders of magnitude by tuning the lattice depth V_0 in the experiment about one order of magnitude.

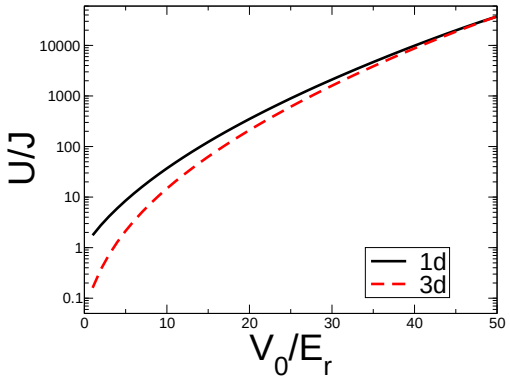

Figure 3.1.: The depth of the optical lattice V_0 measured in units of the recoil energy E_r in the experiments can be related by band structure calculations to the parameter u used in the Bose-Hubbard model (see appendix B.3 and [46, 47] for 3d). For the quasi-one dimensional case, the depth of the orthogonal lattice potentials is fixed to $50E_r$.

3.3. Quantum phase transition in homogeneous systems

3.3.1. Limit of weak interaction: superfluid phase

One limit which can be easily described theoretically is the limit of vanishing interaction. For vanishing interaction $U = 0$ the bosons become free bosons and the Hamiltonian (3.2.0.2) simplifies to the quadratic Hamiltonian:

$$H_{hop} = -\sum_j J_j(b_{j+1}^\dagger b_j + b_j^\dagger b_{j+1}) + (-\mu + \varepsilon_j)\hat{n}_j.$$

Assuming a homogeneous system, i.e. $\varepsilon_j = 0$ for all sites j, the Hamiltonian can be diagonalized by a transformation into Fourier-space. Here we consider a fixed number of particles and set $\mu = 0$. On a finite chain of L sites the single particle eigenstates of the Hamiltonian are the momentum states to the energy eigenvalues $E_q = -2J\cos(k_q)$. The discrete momentum k_q takes the values $k_q = \frac{\pi q}{L+1}$ with $q = -(L-1), .., L$. At temperature $T = 0$ the ground state of the Hamiltonian H_{hop} of a system with N bosons can be constructed from the single particle states by occupying N-times the lowest state. Therefore, the normalized ground state can be written as

$$\big|\psi_0\big\rangle = \frac{1}{N!}(b_{k_1}^\dagger)^N\big|0\big\rangle$$

where $\big|0\big\rangle$ is the vacuum state. For an infinite system the ground state reads $\big|\psi_0\big\rangle \propto (\sum_j b_j)^N\big|0\big\rangle$. All particles are in the same delocalized single particle state and hence the system can be described by a macroscopic wave function with a defined macroscopic phase, i.e. a Gross-Pitaevskii like description is recovered.
A trivial consequence is that the momentum distribution of the ground state is given by a high peak of weight N at the lowest possible momentum. Further the delocalization of the particles shows up in strong fluctuations of the particle number on each site, i.e. the variance of the particle number is of the order of the particle number itself $\big\langle n_j^2\big\rangle - \big\langle n_j\big\rangle^2 = \big\langle n_j\big\rangle + O(\frac{N}{L})$. In an infinite chain the excitation spectrum is gapless.
Even though interacting bosons behave often totally different from free bosons, some of the characteristics for non-interacting bosons on a lattice carry through to weak interactions ($U \to 0$ but $U \neq 0$). For example the number of atoms in the peak in the momentum distribution decreases, but stays macroscopically occupied for weakly interacting bosons and the number fluctuations are still of the order of the occupation itself. The spectrum of weakly interacting infinite one-dimensional Bose systems is still gapless, but the system exhibits a sound like mode with frequency $\omega(k) = v_s k$. The dependence of the sound velocity v_s on the system parameters will be studied in chapter 4.
In a one-dimensional Bose-system the superfluid phase shows several peculiarities due to the presence of strong quantum fluctuations in low dimensional systems. One example which we will meet in the following is the decay of the one-particle density-matrix $\big\langle b_i^\dagger b_{i+d}\big\rangle$: in an one-dimensional system it decays algebraically with the distance d in the superfluid phase, whereas in higher

dimension true long-range order exists, i.e. the one-particle density-matrix approaches a finite value for $d \to \infty$. We will discuss the consequences of the characteristic structure of the one-particle density-matrix on the time-of-flight images in chapter 3.7

3.3.2. Limit of strong interaction: Mott-insulating phase

In contrast to the delocalization in the case of weak interaction, for strong interaction fluctuations in the particle number become energetically costly and the atoms localize at single sites. This limit is also called the 'atomic' limit [52]. If only the interaction is present, i.e. $H_{\text{int}} = \frac{U}{2} \sum_j \hat{n}_j(\hat{n}_j - 1)$, the eigenstates of the system are given by the Fock states $\big|n_j\big\rangle$. Therefore, the single particle ground states are highly degenerate.
Assuming a system with commensurate filling, say $\bar{n}$, the ground state factorizes into single sites by $\big|\psi_0\big\rangle \propto \prod_{j=1}^{L} (b_j^\dagger)^{\bar{n}} \big|0\big\rangle$. In contrast to the superfluid limit, here the particle number on each site is exactly determined, no macroscopic phase coherence is prevalent in the system and the momentum distribution is a constant for all momenta. The first excited state is a particle-hole excitation with the energy $E_1 = U$, i.e. an energy gap exists in this limit. These characteristics carry through to finite but small hopping coefficient J, i.e. $u \gg 1$.
For non-commensurate filling no Mott-insulating phase exists at finite hopping. To understand this consider a system with filling $\bar{n} = 1$ in a Mott-insulating state and add an additional particle. The naive picture is that the additional particle delocalizes on top of a frozen Mott-insulating state to avoid the energy loss by interacting with a localized particle. Therefore, a fraction of the system remains superfluid for all interaction strengths. The true many-particle state will be more complicated than this simple picture, but will still show a remaining superfluid part.

3.3.3. Quantum phase transitions

If the strength of the interaction is increased one changes in the case of commensurate filling between two very different phases, the superfluid phase and the Mott-insulating phase. A quantum phase transition occurs at some critical value u_c. The quantum phase diagram for the homogeneous Bose-Hubbard model was first determined by a mean-field calculation by Fisher et al. [52]. Although there are considerable differences between the case of one, two, or three dimensions induced by strong quantum fluctuations for lower dimensions, the characteristic features are similar. A sketch of the phase diagram in a one-dimensional systems calculated using DMRG [60] and Quantum Monte Carlo [61] methods is shown in Fig. 3.2.
The phase diagram shows characteristic Mott-insulating lobes at small u^{-1} surrounded by the superfluid phase. In these lobes the particle number is locked to a certain integer value. In the superfluid phase different fillings can occur. Hence the Mott-insulating phase is incompressible, i.e. $\frac{\partial n}{\partial \mu} = 0$, whereas the superfluid phase is compressible. A signature to distinguish the phases is the decay of the one-particle density-matrix with the distance: in the Mott-insulating

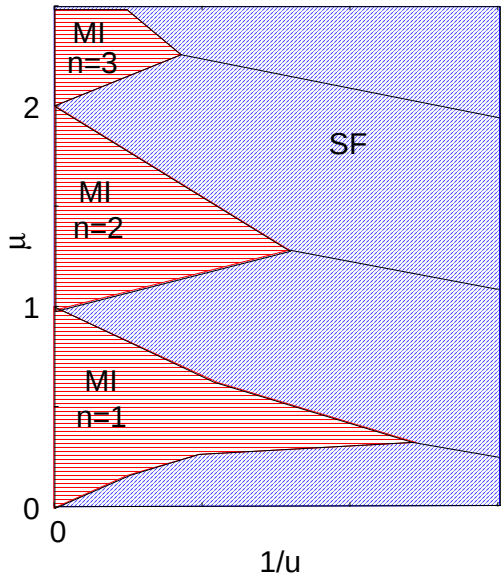

Figure 3.2.: The phase diagram (chemical potential μ versus inverse interaction strength $1/u$) of the one-dimensional Bose-Hubbard model is sketched [60]. MI and SF denote the Mott-insulating and superfluid phase, respectively. The lines out of the tips of the lobes are the lines of constant commensurate density.

phase it decays exponentially, whereas in the superfluid phase it decays algebraically (1D) or shows true long range order (3D). In the phase diagram two different phase transitions have to be distinguished: the incommensurate-commensurate transition, where the number of particles changes going from one phase to the other and the superfluid-Mott-insulating transition at commensurate filling, where the number of particles stays constant, i.e. the transition takes place at the tip of the lobes. By mean field approximations the tip of the lobes is found to be $u_c = 5.8z$ for $\bar{n} = 1$ and $u_c = 4z\bar{n}$ for $\bar{n} \gg 1$, where z is the coordination number of the lattice. Fluctuation corrections to these results have been considered for example by Freericks and Monien [62, 63]. In one dimension strong deviations from the mean field approximation occur: the superfluid-Mott-insulating transition at the tip of the Mott-lobes is of Kosterlitz-Thouless type and the critical value is found to be $u_c(\bar{n} = 1) \simeq 3.37$ according to a DMRG calculation [60].

3.3.4. Gutzwiller approximation

To get a feeling about the importance of 'real' many body effects in the Bose-Hubbard model, we compare results of the Gutzwiller approach [64], which is often used to tackle in particular the system with the trapping potential, to results of the DMRG [65]. The Gutzwiller ansatz is a variational ansatz which reduces the wave function to a product of single-site wave functions, $\big|\Psi_G\big\rangle = \Pi_{j=1}^{L}\big|\Phi_j\big\rangle$, where $\big|\Phi_j\big\rangle = \sum_{n=0}^{\infty} f_n^{(j)}\big|n\big\rangle$ and $f_n^{(j)}$ are constants. Such a product wave function does describe the case at $J = 0$ exactly, but it cannot describe well the remaining part of the one-dimensional Mott-insulator regime. This can be shown by a perturbative study of the Gutzwiller ansatz where the corrections of order $\mathcal{O}(J/U)$ are lost and all correlations become zero. However, this ansatz gives reasonable results in the superfluid regime even in one dimension, where the (quasi-) long-range order is well described by $\big|\Psi_G\big\rangle$. In Fig. 3.3 the numerical results of the DMRG for the ground state energy, the nearest-neighbour correlation, and variance of the particle number are compared to the results of the Gutzwiller ansatz. The results of these 'local' quantities agree quite well for small interaction strength well below the phase transition, but deviate considerably for strong interaction above the transition. In particular, the variance of the particle number and the nearest-neighbour correlations vanish above the critical value u_G in the Gutzwiller ansatz. Note, that the Gutzwiller ansatz cannot give the correct description for the one-particle density-matrix, since in the Gutzwiller approximation it has no spatial dependence at all. This shows how important it is in the treatment of these systems to capture the non-trivial correlations.

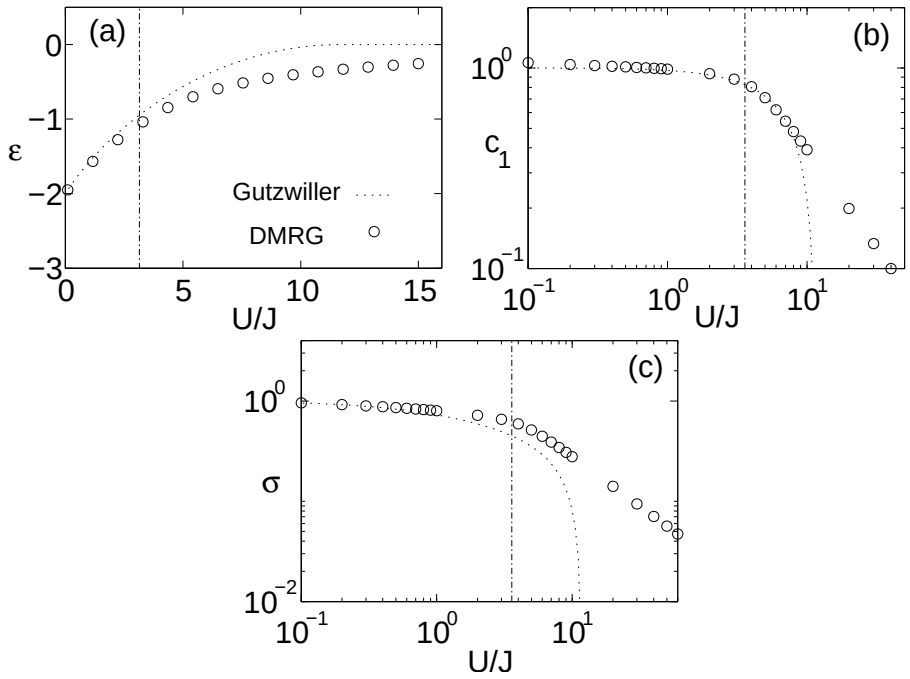

Figure 3.3.: (a) The ground state energy per site, ε, (b) nearest-neighbour correlation, $c_1 = \langle b_{j+1}^\dagger b_j \rangle$, and (c) variance of the number of atoms per site, defined by $\sigma^2 = \langle (n_j - \bar{n})^2 \rangle$. Plot (b) and (c) are in log-log scale. Using filling factor $\bar{n} = 1$, we show results for the Bose-Hubbard model using the Gutzwiller ansatz (dots) and DMRG (circles). Vertical dash-dot lines mark the approximate location of the phase transition according to [66].

3.4. Coexistence of phases in a trapping potential

In the remaining part of this chapter we present our results of DMRG calculations on the quantum phase transition in the presence of a confining potential [67]. The confining trap of the experiment [1] is approximately parabolic (B.2.0.4). It consists of the magnetic trap and the confining component of the laser which generates the optical lattice is approximately parabolic (cf. B.2.0.4). In the following the trap is modeled by setting $\varepsilon_j = V^0_{\text{trap}} (aj - aj_0)^2$ in Eq. (3.2.0.2). Here a is the lattice constant, j the lattice site, and j_0 the central site of the lattice. We choose the strength of the trap proportional to the onsite interaction, i.e. $V^0_{\text{trap}} = v_0 U$, to reproduce the experimental setup. It guarantees that when the optical lattice depth, corresponding to the parameter u in the Bose-Hubbard model, is changed, the size of the atom cloud does not vary much for a fixed particle number as observed in the experiment.
In the presence of a parabolic trap at average filling of approximately one particle per site, one can distinguish three states of the system (see [46, 68]):

(a) $u < u_{c1}$: the particle distribution is incommensurate over the whole system;

(b) $u_{c1} < u < u_{c2}$: regions with incommensurate and commensurate occupancy coexist; and

(c) $u > u_{c2}$: the main part of the system is locked to commensurate filling and only at the boundaries small incommensurate regions exist.

A sketch of the state diagram for $v_0 = 4/64^2 \approx 9.8 \cdot 10^{-4}$ is presented in Fig. 3.4 (A). The insets show the characteristic shape of the particle distribution for the three states. Note, that the critical values u_{c1} and u_{c2} depend on the filling of the system and that for small particle numbers state (b) does not occur. A simple picture of a system with a parabolic trapping potential can be gained by relating it to the situation in a homogeneous system by regarding the chemical potential μ to be space-dependent. For a parabolic confining potential the chemical potential μ must then be inversely parabolic. The vertical lines in Fig. 3.4 (B) indicate for three different parameters u how μ would vary as the trap is traversed from one side through the center to the other side. The symbols in (A) and (B) mark corresponding points. For example, moving from one edge of the trap through the center to the other edge [going from hexagon to ellipse to hexagon in Fig. 3.4 (A) for state (b)], corresponds to increasing μ [going from hexagon to ellipse in Fig. 3.4 (B) for state (b)] and lowering μ again [going back to hexagon in Fig. 3.4 (B) for state (b)]. The regions of locked density correspond to being in the Mott-insulating region of the phase diagram. The exact locations of the interface between the commensurate and the incommensurate regions are difficult to determine. A good qualitative insight can be gained using the picture of the spatially varying chemical potential and determining the critical chemical potential with perturbation theory for the homogeneous system [69]. The difficulty in the exact location of the interfaces is due to the fact that these sites correspond, using terminology appropriate for a

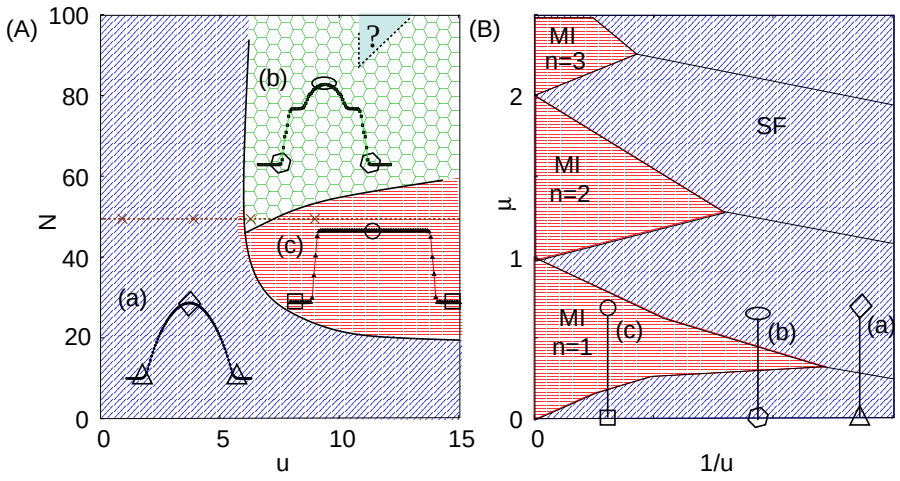

Figure 3.4.: (A) Sketch of the state diagram for $v_0 = 9.8 \cdot 10^{-4}$. The insets sketch the shape of the density distribution in the states. The question mark stands for states with Mott-insulating regions at higher filling. The crosses on the dotted horizontal line mark the parameters chosen in Fig. 3.5. (B) Sketch of the phase diagram of the homogeneous system: chemical potential μ versus $1/u$. The different symbols in (B) mark the locations of the chemical potential values in the local density approximation that correspond to the locations in the density profiles marked in (A).

homogeneous system, to the critical parameter regimes at the phase transition, where strong fluctuations and extreme sensibility to boundary conditions make an investigation very demanding.

3.5. Modifications to the finite DMRG treating confinement potentials

To treat an inhomogeneous system with the DMRG –here the system with the parabolic trap–, it is essential not only to use the infinite-system DMRG algorithm, but the finite-system algorithm (see section 2.2.2). This gives the effective description of the system the possibility to improve further under the sweeps described in section 2.2.2 after the final length L of the system is reached. For a confining potential additional problems arise at the boundaries since there, due to the sparse filling, the information contained in the density matrix can become insufficient for selecting the suitable reduced space. Assume for example a chain of length L, on which the particles are confined to the central region of length $M < L$. In the finite-system algorithm one block grows towards the boundary, while the other block is shrinking at the same time. If now one block becomes so large, that it contains all particles, no particles are left in the shrinking block. The only state in the shrinking block similar to the desired ground state is the state with zero particles, so that this state has almost unit

weight in the calculations in the reduced density matrix (deviations from unity stem from numerical inaccuracies). The other eigenstates are more or less random and do not resemble the ground state of the system. If one does not take care one would loose the information about the state by keeping some of these random states. We overcome this loss of information close to the boundaries by filling up the subspace by retaining states of the previous steps transformed to the new basis. We further adapt the number of states allowed on a site to the expected occupation number of the latter. This is done by using for the number of bosonic states allowed for a site the occupation expected from either the Thomas-Fermi distribution in the case of low interaction and a constant distribution plus an additional offset for strong interaction. The numerical results were tested to be convergent in the cut-off used for the length of the system, the number of states kept for the reduced space, and the number of states allowed per site. The numerical uncertainties given below were determined by comparing data obtained for different parameter sets.

3.6. One-particle density-matrix

To get a better understanding of the three types of states (a)-(c) (cf. section 3.4), we study the properties of the one-particle density-matrix $\rho(i,j) = \langle b_i^\dagger b_j \rangle$, where i and j stand for the sites on the chain and $\langle\rangle$ denotes the expectation value with respect to the ground state. Recall that for the homogeneous system a signature of the superfluid and Mott-insulating phase is given by the decay of the one-particle density matrix for long distances: it decays exponentially in the Mott-insulating phase, $\rho(j, j+d) \propto \exp(-d/\xi)$, and algebraically in the superfluid phase, $\rho(j, j+d) \propto d^{-K/2}$. We have calculated the values of the matrix elements of the one-particle density-matrix for different interaction strengths u and $N = 50$ bosons. The results are shown in Fig. 3.5. In addition, Fig. 3.6 shows the occupancy of the particles $n_j = \rho(j,j)$ and cuts for a particular site i of the data of Fig. 3.5. For the coexistence region in Fig. 3.6 we took a shallower trap $v_0 = 1.8 \cdot 10^{-4}$, such that the different regions are larger and therefore better distinguishable.

For weak interaction (Fig. 3.5 and Fig. 3.6, $u = 1$) the values of most elements of the one-particle density-matrix are relatively large, similar to the superfluid phase in a homogeneous system. In fact the decay of $\rho(i,j)$ with increasing $|i-j|$ is dominated mainly by the trivial reduction of the density n_i and n_j as the outer regions of the trap are approached. Indeed, note that in Fig. 3.6 the occupancy $n_j = \rho(j,j)$ (triangles down) acts as envelope for the decay with the distance of the elements of the one-particle density-matrix and thus seems to determine their long range decay. When the interaction strength is increased (Fig. 3.5, $u = 4$) the off-diagonal elements become smaller, i.e. the decay of the correlations with the distance between the sites becomes faster, while the occupancy (values at $i = j$) remains incommensurate over the whole system. A further increase of the interaction, such that $u_{c1} < u < u_{c2}$, favours the formation of regions where the density is locked to commensurate filling (Fig. 3.5, $u = 6$ and Fig. 3.6, $u = 10$). In these regions the correlations decay faster

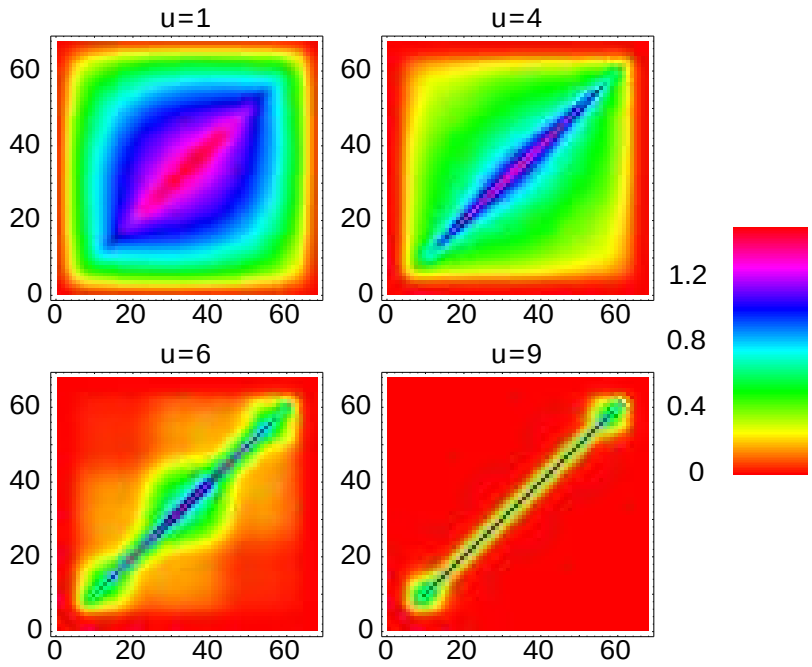

Figure 3.5.: The one-particle density-matrix $\rho(i,j)$ is shown in a system with trap $v_0 = 9.8 \cdot 10^{-4}$ and $N = 50$ bosons. (Site j is plotted on the x-axis, site i on the y-axis, i.e. the diagonal from bottom left to top right corresponds to the particle density. The absolute uncertainty for the data is about 10^{-5}.) The crosses on the dotted horizontal line at $N = 50$ in the state diagram Fig. 3.4 (A) mark the position of the parameters chosen here.

than in the rest of the system. For strong interaction $u > u_{c2}$ the occupancy in the system (except at the boundaries) becomes locked and the correlations in the bulk decay rapidly (Fig. 3.5 and Fig. 3.6, $u = 9$) similar to the Mott-insulating phase in the homogeneous system.

3.6.1. Scaled one-particle density-matrix

We now analyse the behaviour of the one-particle density-matrix for the system with trap in more detail. Since we saw in Fig. 3.6 that it is strongly influenced by the occupation, we focus on the scaled correlation functions:

$$C_i(r) = \left\langle b_i^\dagger b_{i+r} \right\rangle / \sqrt{n_i n_{i+r}}, \tag{3.6.1.1}$$

in order to divide out the leading density dependence of $b_i \propto \sqrt{n_i}$. (Note that for the state in which the occupancy is locked to $n_i = 1$, this scaling is trivial.) In the absence of density fluctuations $C_j(r)$ is just the pure phase correlation function $\left\langle \mathrm{e}^{\mathrm{i}\phi_j} \mathrm{e}^{-\mathrm{i}\phi_{j+r}} \right\rangle$. At the two particle level, the step equivalent to the scaling is going from the two-particle density $\rho^{(2)}(x_1, x_2)$ to the dimensionless two particle distribution function $g^{(2)}(x_1, x_2) = \rho^{(2)}(x_1, x_2)/[\rho^{(1)}(x_1)\rho^{(1)}(x_2)]$.

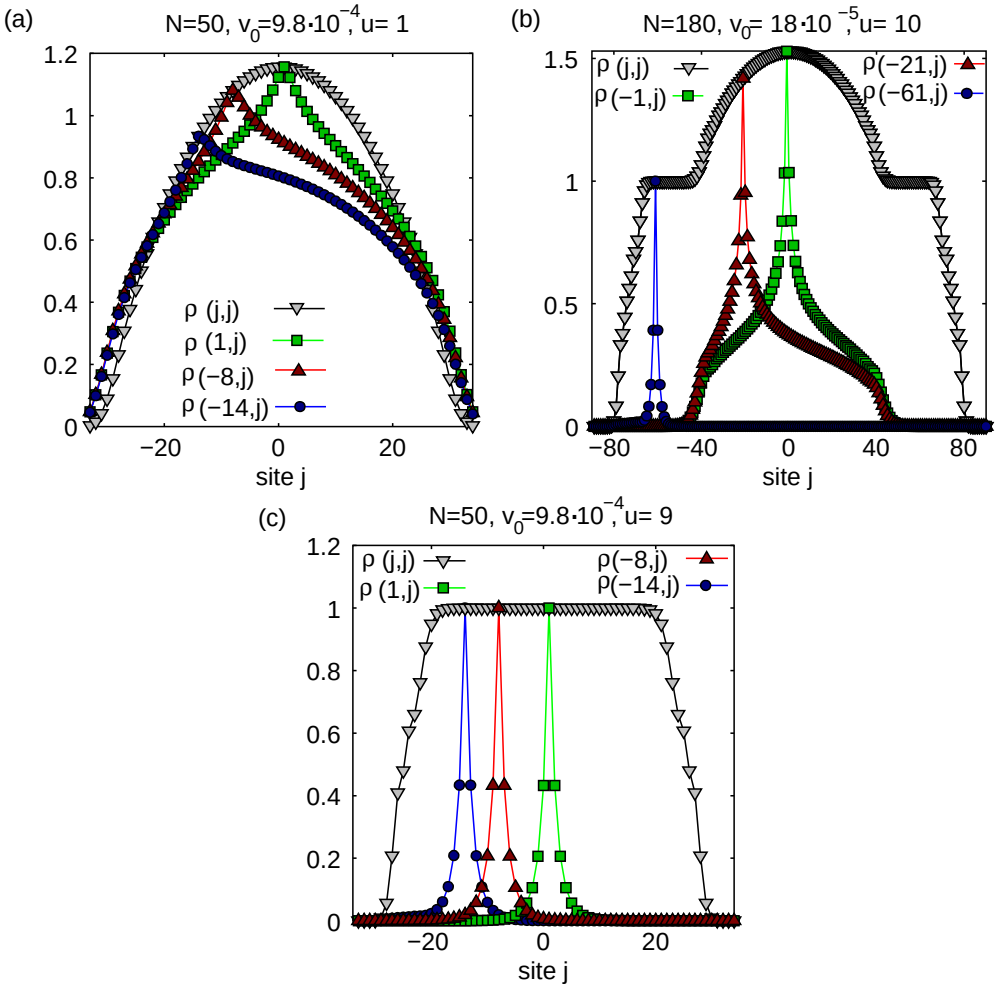

Figure 3.6.: Different matrix elements of the one particle density matrix $\rho(i,j)$ are shown. In (a) and (c) the same parameters as in Fig. 3.5 are used. In (b) we use the trapping strength $v_0 = 1.8 \cdot 10^{-4}$ and $N = 180$. The curve $n_j = \rho(j,j)$ shows the occupancy of the particles, whereas the other curves give the correlations between one fixed site i and a varying site j. (The absolute uncertainty for the data is about 10^{-5}.)

Remarkably, we find that by this simple scaling the signatures of the superfluid and Mott-insulating phases in the homogeneous system, namely the algebraic $C_i(r) \propto A\,|r|^{-K/2}$ and the exponential $C_i(r) \propto A\mathrm{e}^{-|r|/\xi}$ decay, can be recovered approximately even in the presence of a parabolic confining potential. This is illustrated in Fig. 3.7, which shows the scaled correlations $C_i(r)$ for three different choices of site i for three different interaction strengths. For weak interactions [Fig. 3.7 (a)], i.e. $u \leq u_{c1}$, they decay approximately algebraically with distance r (neglecting the boundary regions). In the intermediate regime, $u_{c1} < u < u_{c2}$ [Fig. 3.7 (b)], the decay in the regions where the density is incommensurate is still algebraic ($N = 70, 90$), whereas in the regions where the density is locked, it shows an exponential behaviour ($N = 21$). Increasing the interaction further ($u \geq u_{c2}$) [Fig. 3.7 (c)] the incommensurate regions disappear and the correlations decay exponentially in the bulk.
In Fig. 3.8 we compare fits of the unscaled ρ versus the scaled correlations C. We see that as the trap becomes more shallow [(a) to (b)] the unscaled correlations show the algebraic decay over longer distances, such that in the limit of a homogeneous system their algebraic decay (except at the boundaries) is recovered.

3.6.2. Comparison to the hydrodynamical approach

It is instructive to compare the numerically exact DMRG results to a hydrodynamical treatment of the interacting 1D Bose gas [70] combined with a local density approximation. In the hydrodynamical approach the low-energy fluctuations of the system are described by two conjugate fields, the phase fluctuations $\phi(x)$ and the density fluctuations $\theta(x)$. In a homogeneous system the density fluctuations are chosen around the constant density. This approach can be generalized to the case of inhomogeneous systems [71] by taking the density fluctuations around a smooth, spatially dependent density profile $n(x)$. [1] The Hamiltonian becomes

$$H = \frac{\hbar}{2\pi}\int dx\left\{v_J(x)(\partial_x\phi)^2 + v_N(x)[\partial_x\theta - \pi n(x)]^2\right\},$$

precisely of the structure as in the homogeneous case, except that $n(x)$, and therefore $v_J(x) = \pi\hbar n(x)/M$ and $v_N(x) = (\pi\hbar)^{-1}(\frac{\partial\mu}{\partial n})|_{n=n(x)}$, now depend on x. To account for the inhomogeneity, the local density approximation $\mu[n(x)] + V(x) = \mu[n(0)]$ was used to obtain the mean density profile [73]. In the case of weak interaction i.e. $\gamma = \frac{Mg}{\hbar^2 n(x)} \ll 1$ it gives:

$$n(x) = n_0(1 - (x/R)^2), \tag{3.6.2.1}$$

where R is the Thomas-Fermi radius. Based on this approximation Gangardt and Shlyapnikov [71] have shown that the normalized matrix elements of the one-particle density matrix are given by:

$$C(x) := \frac{\langle b^\dagger(x)b(-x)\rangle}{\sqrt{n(x)n(-x)}} = \left(\frac{|2x|}{l_c(x)}\right)^{-K(x)/2}, \tag{3.6.2.2}$$

[1] An equivalent procedure was used for 1D Fermionic gases by Recati et al. [72].

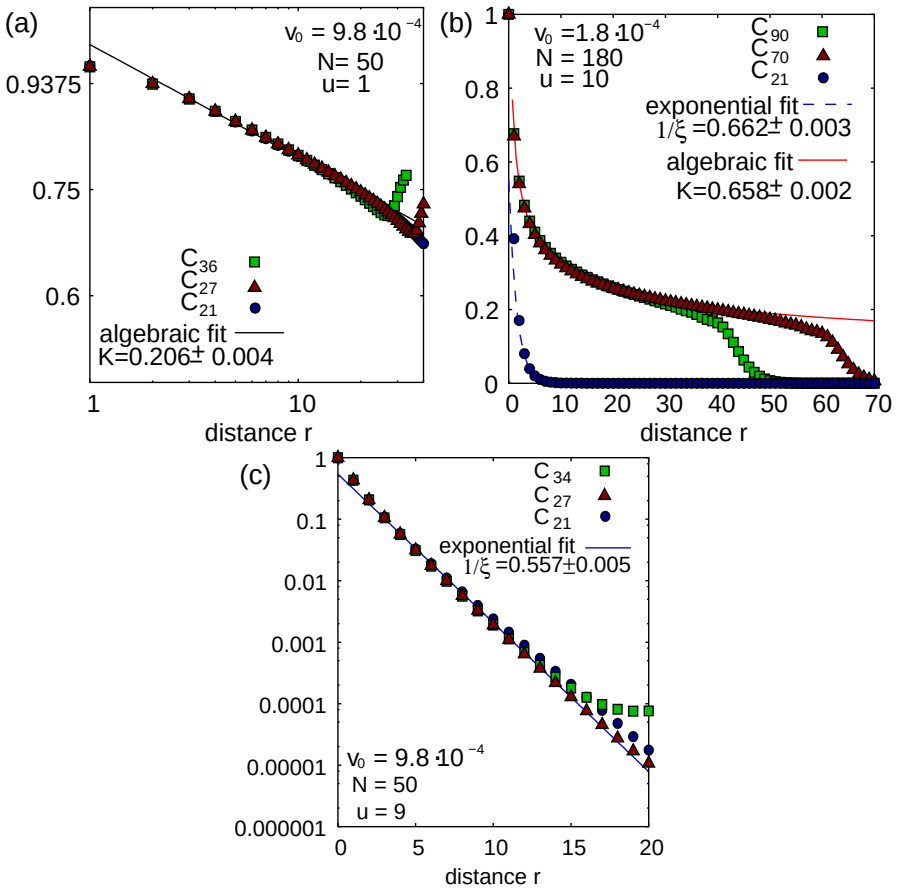

Figure 3.7.: Scaled correlations $C_j(r)$ [Eq. 3.6.1.1] for different fixed sites j are plotted as a function of the distance r for different values of u. For the coexistence region (b) a shallower trapping potential is chosen, such that the extents of both the incommensurate and the commensurate region are large enough to allow identification of the algebraic and exponential behaviour.

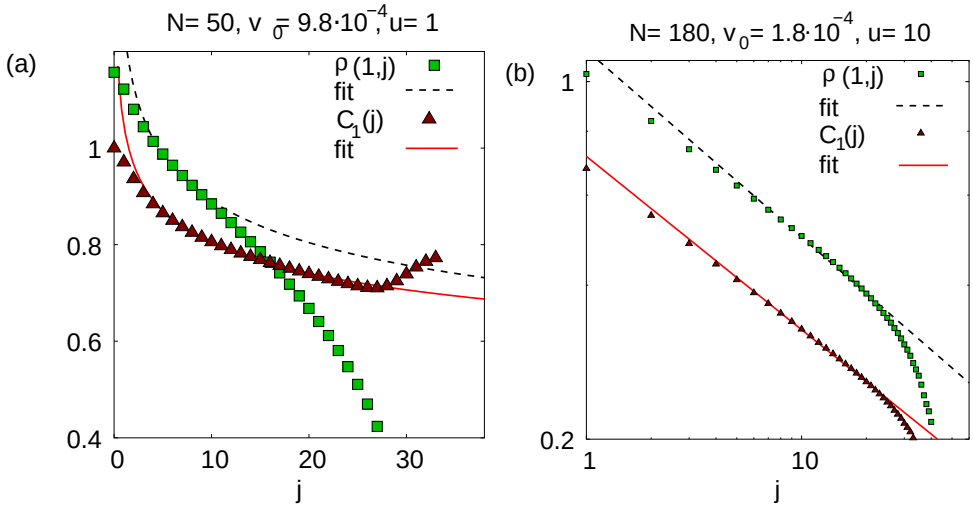

Figure 3.8.: The decay of the unscaled and the scaled correlations and corresponding algebraic fits. One can see that for the steeper potential (a) the unscaled correlations show the algebraic decay only for intermediate distances. When the potential becomes more shallow the behaviour of scaled and unscaled becomes more and more similar also for longer distances.

where K is the parameter corresponding to the Luttinger parameter and l_c the longitudinal correlation length. Eq. (3.6.2.2) is derived assuming $|2x| \gg l_c$. Specializing to weak interaction, i.e. $\gamma \equiv 1/dn \ll 1$, the approximations $l_c(x) \approx \sqrt{\frac{d}{n(x)}}$ and $K(x) \approx 1/\left(\pi\sqrt{dn(x)}\right)$ hold, where $d \propto a_\perp^2/a_s$ is the characteristic length of the interaction. d depends on the 3D scattering length a_s and the amplitude $a_\perp$ of the transverse zero point oscillation. The condition $|2x| \gg l_c$ generally is fulfilled, but breaks down at the boundaries, where $n(x)$ vanishes causing a divergence in $l_c(x)$.

Comparing Eq. (3.6.2.2) to the quasi-exact results of DMRG, we show that the local density approach describes very well the scaled correlations in the inhomogeneous systems for $\gamma \leq 2$. To this end we fitted the function $C(x)$, Eq. (3.6.2.2), to the corresponding DMRG results $\frac{\langle b^\dagger(j)b(-j)\rangle}{\sqrt{n(j)n(-j)}}$, using only d as fitting parameter [Fig. 3.9]. We find very good agreement in the bulk of the superfluid regions in both, the purely superfluid state [Fig. 3.9 (a)] and the coexistence state [Fig. 3.9 (b)]. The quality of the agreement is somewhat surprising, because the pure state ($\gamma = 0.6$) and the coexistence state ($\gamma = 1.7$) are in an intermediate regime between the Thomas-Fermi limit ($\gamma \ll 1$) and the Tonks gas ($\gamma \gg 1$), where the density profile is no longer parabolic [73].

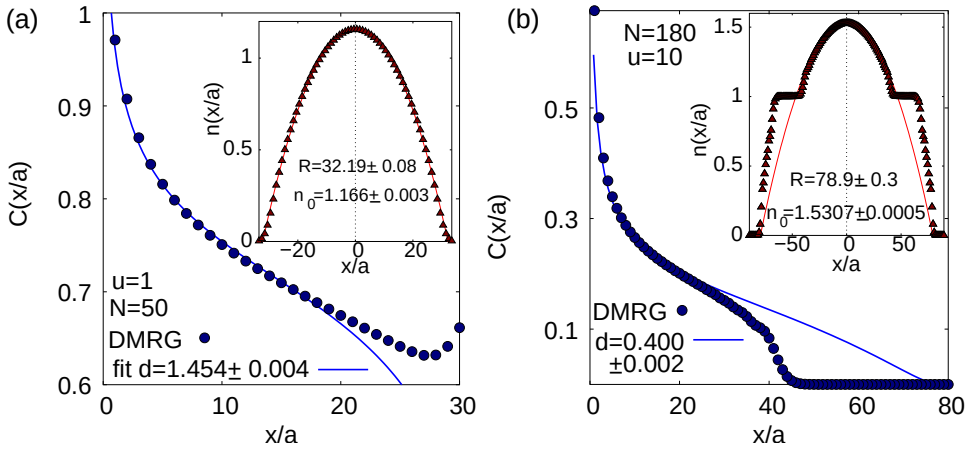

Figure 3.9.: Quasi-exact DMRG results for $C(j)$ (symbols) are compared to equation (3.6.2.2) obtained by the hydrodynamical approach [71] (lines). We used $n(x) = n_0(1 - (x/R)^2)$, where n_0 and R are determined by fitting to the DMRG results (see insets). The uncertainties are obtained by varying the fit range in the sensible region away from the boundaries.

3.7. Connection to experiment

3.7.1. Interference pattern

In the experiments with ultracold atoms measurements are often performed by taking time-of-flight images. To do this the atoms are released suddenly from all external trapping potentials and evolve freely for a certain time, the so called time-of-flight. After this time the column integrated density of the expanding cloud is measured by light absorption imaging. In many cases of interest the interaction between the atoms can be neglected after switching off the external potentials and the density of the evolving cloud is given by [74, 75]

$$\langle \hat{n}(r) \rangle_t = \langle \phi | U_0^\dagger(t) \Psi^\dagger(r) \Psi(r) U_0(t) | \phi \rangle.$$

Here $|\phi\rangle$ is the state of the system before it was released from the trapping potentials and $U_0(t)$ is the free propagator. After a long time of flight the density distribution becomes proportional to the momentum distribution in the system before it was released, i.e. $\langle \hat{n}(r) \rangle_t \approx (M/ht) \langle \hat{n}_{q(r)} \rangle$, where the correspondence between the momentum in the trap and the position in the evolving cloud is given by $q(r) = Mr/(\hbar t)$. Therefore, the measured distribution can as well be expressed in the creation and annihilation operators of the lattice model

$$\begin{aligned} I(k) &\propto |w(k)|^2 \rho(k), \\ \text{with} \quad \rho(k) &= \frac{1}{N} \sum_{j,j'=1}^{L} \mathrm{e}^{\mathrm{i}(j-j')ak} \langle b_j^\dagger b_{j'} \rangle, \end{aligned} \tag{3.7.1.1}$$

where L is the number of sites in the chain and N the total number of particles. The function $w(k)$ is the Fourier transformation of the associated Wannier

function which varies only slowly in momentum space due to its localization in space. Hence, the factor $|w(k)|^2$ gives a slowly varying envelope. Therefore the long-wavelength dependence of the interference pattern is mainly determined by the function $\rho(k)$ which we identify with the interference pattern in the following. The measured distribution contains direct information about the many-body state of the atoms before they are released from the trap. Let us now investigate how information about the state of the system, in particular if it is superfluid or Mott-insulating, can be extracted from the interference pattern and how the interference pattern is influenced by the confining potential. For the parameters studied here, the approximation of a negligible contribution of the interaction energy to the time-of-flight images is valid for all momenta in the second or in higher Brillouin-zones. Indeed, these momenta are of order $2\hbar\pi q/L$, where $q \in \mathbb{Z}$ and $|q| > L$. Thus the ratio of the energies after switching off the confining potentials is very small given by $\frac{E_{\rm int}}{E_{\rm kin}} \propto \frac{n_{3D}(4\pi\hbar^2 a_s)/M}{(\pi\hbar q/L)^2/(2M)} \propto \frac{a_s}{a} \approx 10^{-2}$ for $n_{3D} < 1.5/a^3$ and a_s/a like in the experiment of Greiner et al. [1]. The function $\rho(k)$ has been studied for very small systems numerically [76], with the hydrodynamical approach [77] for a 1D homogeneous system and for the confined system in 3D [74] and 1D [78]. In Fig. 3.10 we plot the DMRG results (symbols) for the function $\rho(k)$ for several values of the parameter u, comparing the homogeneous system ($\varepsilon_i = 0$) with open boundary conditions (A) to the parabolic system (B). For the homogeneous system the chosen parameters correspond to the superfluid regime $u = 2 < u_c$, close to the transition $u = 3.5 \approx u_c$, and the Mott-insulating regime $u = 10 > u_c$. Additionally, in Fig. 3.11 special properties of the interference pattern are plotted versus the interaction strength. In the homogeneous system with commensurate filling, $\bar{n} = N/L$=1 [Fig. 3.10 (A)] we find a very sharp peak at small momenta for $u < u_c$. If u is increased the peak height decreases smoothly [Fig. 3.11 (A)] and the background increases [Fig. 3.11 (B)] smoothly until they both saturate at the filling factor for $u \to \infty$. The half width w [Fig. 3.11 (C)], however, shows a clear upturn. This upturn signifies a phase transition, since it stems from the behaviour of the correlation length ξ ($\propto w^{-1}$), which diverges in the superfluid phase ($\xi \propto L$) and becomes finite in the Mott-insulating phase ($\xi \propto \Delta^{-1}$, where Δ is the energy gap).

For the parabolic system [Fig. 3.10 (B)], the interference pattern for small and large u is similar to the interference pattern in the homogeneous system. In the intermediate regime, however, it has a more complex behaviour, which is most clearly evident in the half width w [Fig. 3.11 (C)]. For small particle numbers ($N = 40$), the half width w is very small for $u \lesssim u_{c1}$ and rises continuously for $u > u_{c1}$ similar to the behaviour for a homogeneous system in the superfluid and Mott-insulating phases, respectively. In contrast, for larger particle numbers ($N = 50$) three different regimes corresponding to the three different states shown in Fig. 3.4 are observed: (a) for $u < u_{c1}$, w is very small, (b) for $u_{c1} < u < u_{c2}$, w rises slowly, until at $u \sim u_{c2}$ it shows a sudden jump-like increase, (c) for $u > u_{c2}$, it continues to rise strongly. That means that in the superfluid (a) and the Mott-insulating (c) state the behaviour of w resembles that of the homogeneous system. This is as expected, since the scaled correla-

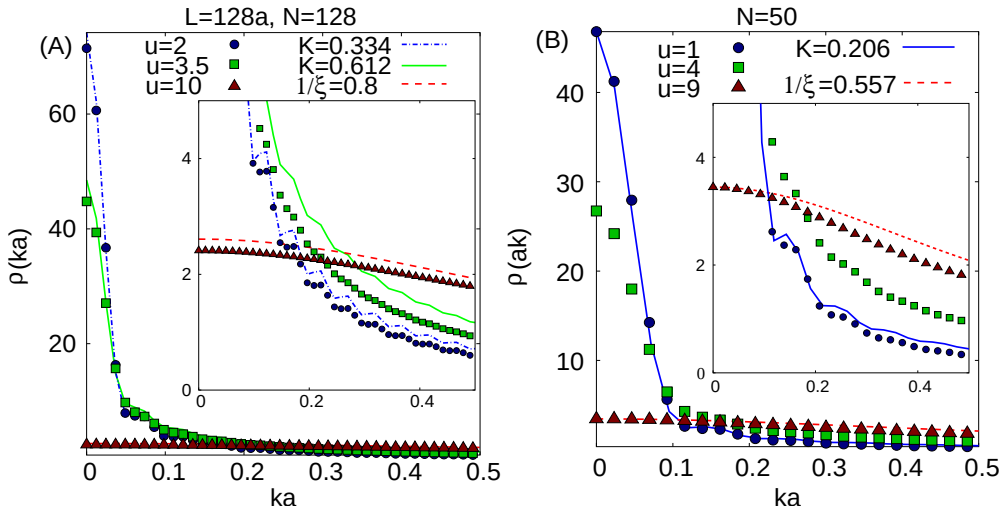

Figure 3.10.: Interference pattern for the system with (A) open boundaries and with (B) parabolic trap for different values of u. Symbols are the results of the DMRG (maximal uncertainty 0.1) and lines the results of the approximations explained in the text. The insets enlarge the scale of the y-axis. For a homogeneous system $u_c(\bar{n} = 1) \simeq 3.37$ is the critical value in the thermodynamic limit according to [66].

tions show the same decay as in the corresponding homogeneous phases. In the intermediate regime (b), however, it shows a new behaviour, a slow increase, which is due to the coexistence of the superfluid and the Mott-insulating state. The superfluid region determines mainly the height of the interference peak, while its broadening is due to the presence of the Mott-insulating region. For certain parameters (not shown here) in the crossover region between the totally incommensurate and the coexistence region, the interference pattern has additional oscillations with period $2\pi/l$, where l is the distance between the two outer superfluid regions, due to the appearance of relatively strong correlations between the latter[2]

Knowing that except for the scaling factors the behaviour of the one-particle density-matrix is the same with and without trap we can investigate to what extent the properties of the interference patterns in Fig. 3.10 can be understood in terms of simple phenomenological approximations for $\langle b_j^\dagger b_{j'} \rangle$ in the homogeneous and the scaled correlations $C_j(r)$ in the inhomogeneous system.

To illustrate this we show in Fig. 3.10 (A) in addition to the DMRG results

[2]Similar oscillations were seen in [78]. In smaller systems such as in [74] the effect is more pronounced causing well-separated satellite peaks.

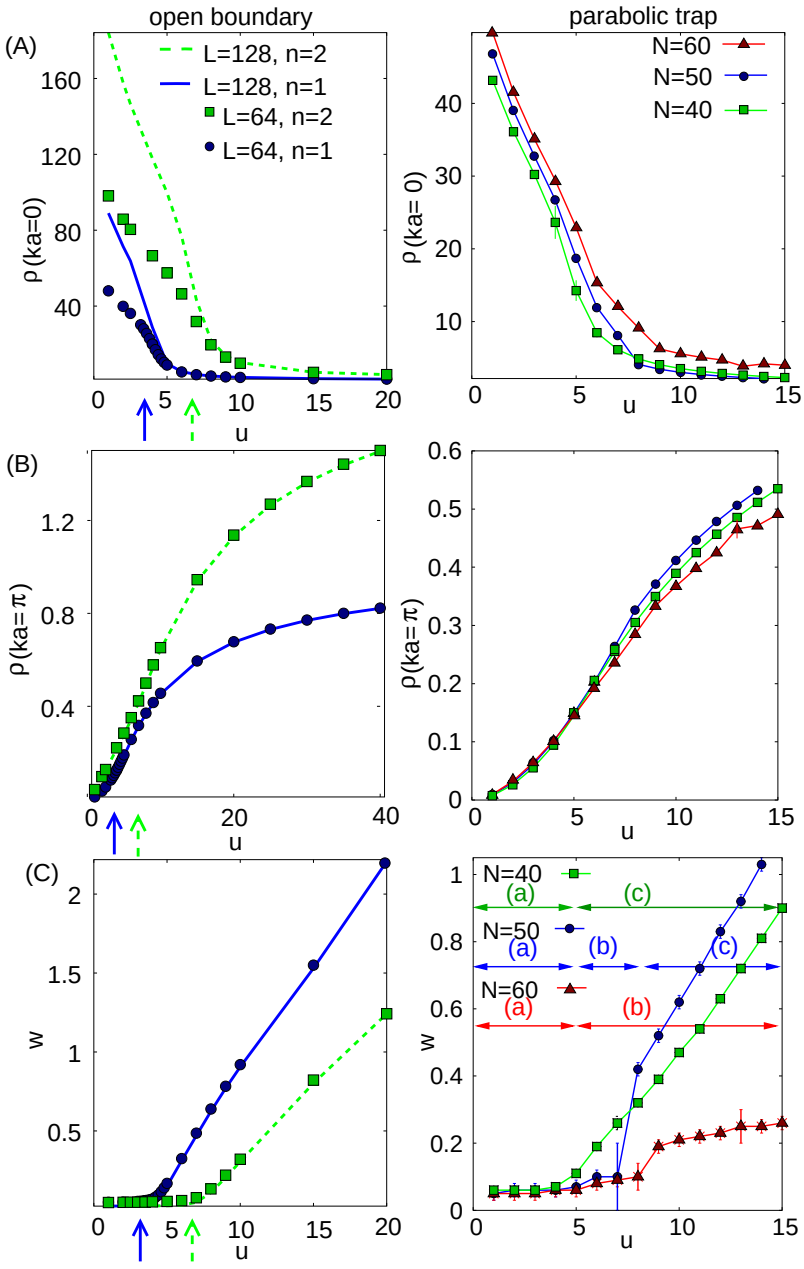

Figure 3.11.: Properties of the interference pattern: (A) peak height, (B) background, and (C) half width of the central interference peak for a system with open boundary conditions on the left and for a parabolic confining potential on the right. The arrows on the left mark the critical value of u in the thermodynamic limit of the homogeneous system (blue/solid and green/dashed for $n = 1$ and $n = 2$ respectively). The height of the peak decreases and the background increases with increasing u. The arrows in (C) on the right mark the three different regimes described in the text.

(symbols), results (lines) obtained by approximating $\langle b_j^\dagger b_{j'} \rangle$ in Eq. (3.7.1.1) by

$$\langle b_j^\dagger b_{j'} \rangle = \begin{cases} A\,|j-j'|^{-K/2} & \text{for} \quad j \neq j' \\ n_j & \text{for} \quad j = j' \end{cases} \tag{3.7.1.2}$$

$$\text{and} \quad \langle b_j^\dagger b_{j'} \rangle = B\mathrm{e}^{-|j-j'|/\xi}, \tag{3.7.1.3}$$

for small and large u, respectively. The values of K and ξ are determined by fitting $\langle b_j^\dagger b_{j'} \rangle$ to DMRG results (not shown here). The constants A and B are chosen such that the value at $k = 0$ agrees with the DMRG results. In Fig. 3.10 (B) the approximation (lines) are obtained analogously by taking the density scaling into account, i.e. replacing $\langle b_j^\dagger b_{j'} \rangle$ by the algebraically and the exponentially decaying functions times the scaling factor $\sqrt{n_j n_{j'}}$

$$\langle b_j^\dagger b_{j'} \rangle = \begin{cases} A\sqrt{n_j n_{j'}}\,|j-j'|^{-K/2} & \text{for} \quad j \neq j' \\ n_j & \text{for} \quad j = j' \end{cases} \tag{3.7.1.4}$$

$$\text{and} \quad \langle b_j^\dagger b_{j'} \rangle = \sqrt{n_j n_{j'}} B\mathrm{e}^{-|j-j'|/\xi},$$

for small and large u, respectively. Hereby we use the density distribution $n_j = n_0(1-(j-j_0)^2/R^2)$ for $u = 1$, and $n_j = 1$ for $u = 9$. The parameters K and ξ are determined by fitting the scaled correlation functions. Comparing the DMRG data to the approximation we see in Fig. 3.10 that for both cases, the homogeneous system and the system with trap, this simple approximation works very well for small values of ka; in particular, it reproduces the correct shape of the peak [even including the small non-monotonities which are due to the finite sum in Eq. (3.7.1.1)]. Therefore, once the characteristic decay of the (scaled) one-particle density-matrix has been identified (in this case by fitting to DMRG results), our simple scaling procedure captures most of the essential observable physics.

3.7.2. Comparison to experiment

Clearly our calculations in one dimension cannot be compared quantitatively with the earlier experiments in a three-dimensional lattice [1]. Recently, however, an array of truly one-dimensional Bose systems has been created [59, 79]. Typically, this array consists of several thousands of parallel one-dimensional systems, called tubes, with different fillings. The advantage of this setup compared to a single tube (for example realized on an atom chip) is that the signal is enhanced, but a disadvantage is that tubes with different fillings contribute to the measured signal and smear out otherwise clear structures. This can be seen in the experimental results [79] for the half width of the interference pattern which was measured for different lattice heights in such an array following our predictions. In Fig. 3.12 the experimental result for the half width is shown for one-dimensional tubes with $\bar{n} \approx 1.2$ (solid squares), with $\bar{n} \approx 0.6$ (open squares) and three-dimensional system $\bar{n} \approx 1$ (triangles). Note, the parameter J used in Fig. 3.12 is the same as the one used in this work for the one-dimensional tubes, but for the three-dimensional system the J in Fig. 3.12

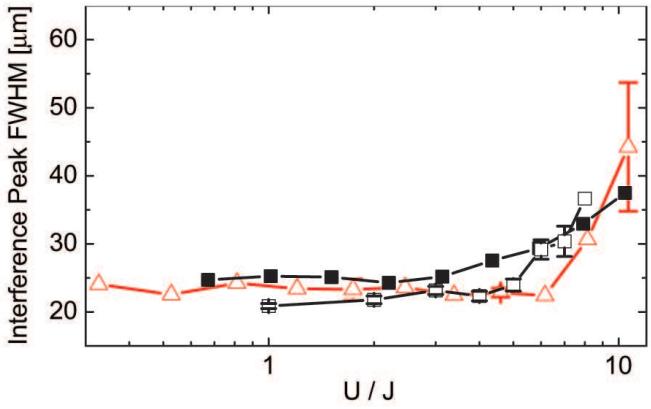

Figure 3.12.: Experimental results for the half width of the central interference peak at different interaction strength [79]. The different curves correspond to one-dimensional tubes with $\bar{n} \approx 1.2$ (solid squares), with $\bar{n} \approx 0.6$ (open squares), and a three-dimensional system $\bar{n} \approx 1$ (triangles).

corresponds in our notation to the sum of the hopping coefficient in all directions, i.e. $J_e = 2(J_x + J_y + J_z)$. In the case of a three dimensional system the upturn at the transition is relatively sharp and lies approximately at $U/J_e \approx 6$ in agreement with the predicted critical value $U/J_e = 5.8$ of mean-field approximations. For the array of one dimensional tubes with filling $\bar{n} \approx 0.6$ the upturn sets in at about $u \approx 4$ and for filling $\bar{n} \approx 1.2$ at $u \approx 2$. This is in good qualitative agreement with our predictions. We found that for small particle numbers (cf. $N = 40$ in Fig. 3.11) the half width bends up at approximately the critical value and for higher particle number (cf. $N = 50$ in Fig. 3.11) the half width increases slightly before it bends up at a higher value of u than the curve for the lower particle number. Due to the presence of the tubes with different filling the upturn in the experiment is not as sharp as in our predictions and quantitative comparisons are difficult, but it is still sharp enough to distinguish the lattice height for which most of the system are in the superfluid-like state (a) or Mott-insulating-like state (c), respectively.

3.8. Conclusion

We have shown that numerical calculations using the DMRG method in the Bose-Hubbard model are well suited to correctly describe and predict experimental quantities for ultracold atoms in optical lattices. We were able to demonstrate that the complication introduced by the confining potential which in the current experimental setups is unavoidably introduced by the intensity profiles of the lasers producing the lattice can be overcome by a modified finite DMRG calculation. In particular, the characteristics of the one-particle density-matrix known for the superfluid and Mott-insulating phase of the ho-

mogeneous system can be recovered in the confined case using a scaled one-particle density-matrix. Comparison with the local density approximation in the weakly interacting regime showed good agreement with the DMRG calculation thus providing mutual confirmation. Investigation of various quantities showed that the half width of the interference peak is best suited to identify the Mott-insulating and superfluid phases in the experiment.

4. Evolution of density wave packets in ultracold bosons

4.1. Perturbations: experiments and theoretical descriptions

In the present chapter our aim is to study the propagation of density wave packets in a Bose-Einstein condensate confined to an optical lattice [80]. Quite generally, the low-lying excitations in a Bose-Einstein condensate are sound-like and correspond to fluctuations of the condensate phase [12]. The associated sound velocity depends on both the density in the system and the strength of the interaction between the atoms. Experimentally, density perturbations in a Bose-Einstein condensate have been created by applying a localized potential to the Bose-Einstein condensate with a far detuned laser beam [81, 82]. Alternatively, a phase imprinting method can be used, which allows to create solitonic excitations [83, 84]. Employing these experimental techniques for the generation of a density perturbation in a setup of ultracold bosons in optical lattices would make the investigation of the evolution of density waves in a lattice Bose gas with different interactions strengths possible.
The theoretical description of these systems beyond the weak interaction limit, where a Gross-Pitaevskii or Bogoliubov description applies, is very demanding and very few results are available. In this chapter we use the adaptive t-DMRG (see section 2.7) to calculate the time evolution of the density wave packets [80]. This method allows us to find the time evolution for both weak and strong interaction. In particular, it works best in an intermediate interaction regime, where other methods are not reliable.
Most previous theoretical approaches were limited to the regime of weak interactions [85, 86, 87, 88], describing properly systems with many particles per site. In contrast to these, we focus here on perturbations in one-dimensional systems at low filling, i.e. with approximately one or less than one particle per site on average at different interaction strengths. This regime is of particular interest, since it allows to study the behaviour of density waves near the transition from a superfluid to a Mott-insulating phase or close to the Tonks gas regime, as has been realized experimentally by Stöferle et al. [89] and in references [59, 90], respectively. We focus our investigation on the sound velocity, i.e. the velocity of propagation of an infinitesimal perturbation. In particular we discuss the dependence of the sound velocity on the interaction strength and background density. Further, we determine the velocity of propagation of a perturbation with finite amplitude and the decay of the amplitude with time, thus analyzing nonlinear effects which are difficult to discuss analytically.
To make the connection to earlier work we compare our numerical results in

the limits of weak and strong interaction to different approximations: For weak interactions a continuum description is applied, which leads to the Lieb-Liniger model [91, 92], a system of bosons with δ-interaction. We compare the resulting sound velocity with our results and find good agreement up to intermediate interaction strengths. A further simplification is obtained by treating the Lieb-Liniger model in a hydrodynamical approach. The sound velocity determined by this approach is that of a Gross-Pitaevskii type description. It agrees with our result only for rather small interaction strengths. In the limit of strong interactions and at low fillings, the Bose-Hubbard model can be mapped onto a model of spinless fermions [93]. As expected, our numerical results for the sound velocity in this limit smoothly approach the value predicted from this mapping to fermions [94]. Thus the adaptive t-DMRG provides a unified description for the whole range of interaction strengths.
This chapter is organized as follows: We start by checking the applicability of the Bose-Hubbard model (Sec. 4.2) to describe density perturbations in a system of ultracold bosons subjected to an optical lattice. Then we explain how a density perturbation can be created in this framework (Sec. 4.3). Before we discuss the evolution of the perturbation in Sec. 4.5, we introduce the analytical approximations to which we compare our results in Sec. 4.4. In section 4.6 we analyse the decay of the amplitude of the perturbation. Further the dependence of the velocity, in particular the sound velocity, on system parameters like the background density, the interaction strength (Sec. 4.7) and the height of the perturbation (Sec. 4.8) are discussed. Finally in section 4.9, we study how the presence of a wave packet can be detected experimentally from the interference pattern in a time-of-flight experiment.

4.2. Theoretical description of the density perturbation

As seen in chapter 3 ultracold bosons in an optical lattice can be well described by the Bose-Hubbard model (3.2.0.2), if the dynamics of the system is confined to the lowest energy band induced by the lattice. Hence the additional energy by the perturbation has to be much smaller than the level spacing of the energy bands induced by the optical lattice. As we will see below this gives a constraint on the strength of the density perturbation which can be described within the Bose-Hubbard model. In the following we will investigate the time evolution of density wave packets of approximately Gaussian form which is created at $t = 0$, i.e.

$$\rho_j(t=0) = \rho_0(1 + 2\eta \mathrm{e}^{-j^2/(2\sigma^2)}). \tag{4.2.0.1}$$

Here ρ_0 is the background density, η the height of the perturbation, and σ its width. The energy change induced by such a density perturbation consists of two contributions: (i) the change in the interaction energy and (ii) the change in the kinetic energy.

(i) The change in the interaction energy can be estimated by taking the 'mean' interaction of the atoms in the system with the perturbation

into account by $\Delta E_{\text{int}} = 2\rho\Delta\rho U$. Here we approximate the additional density corresponding to the perturbation by the product of its width and height $\Delta\rho \sim \eta\sigma$. The interaction strength is given by the integral $U \approx g\int d^3x\,|w(x)|^4$, where $w(x)$ is the associated Wannier function localized around $x = 0$ (appendix B.3.2).

(ii) The kinetic energy is dominated by the fast density oscillations induced by the periodic lattice potential as long as the density in the perturbation varies more slowly than these oscillations. Hence an upper bound for the change in the kinetic energy is given by $\Delta E_{kin} \sim J\Delta\rho$.

The total energy change induced by the density perturbation is therefore given by $\Delta E \sim U\Delta\rho(J/U + 2\rho)$. On the other hand approximating the wells of the lattice by parabolic potentials the energy level spacing ν can be expressed by the oscillator lengths $a_\perp$ and $a_{||}$ perpendicular and parallel to the quasi-one dimensional system. The condition $\Delta E \ll \nu$ is obeyed for $\rho \sim 1$ and $J/U \lesssim 1$ provided that $\eta\sigma \ll \frac{a_\perp^2}{a_{||}a_s} \sim 10$, where a_s is the scattering length. This means that as long as the density perturbation is not too strong, the description of the system by the Bose-Hubbard model is applicable.

4.3. Preparation of the density perturbation

To prepare a density perturbation as in Eq. 4.2.0.1 we apply a localized external potential ε_j of Gaussian form [Eq. (3.2.0.2)],

$$\varepsilon_j(t) = -2\tilde{\eta}\tilde{\rho}\mathrm{e}^{-j^2/2\tilde{\sigma}^2}\,\theta(-t)\;. \tag{4.3.0.2}$$

This potential is assumed to be switched on adiabatically such that the system is in its ground state at $t = 0$. We determine this initial state using a finite-system DMRG-algorithm. For times $t > 0$ the external potential is switched off and the perturbation can evolve freely in the system.
For weak density perturbations, this potential creates an approximately Gaussian density packet (Eq. 4.2.0.1). Note the difference between the parameters $\tilde{\sigma}$ and $\tilde{\eta}$, which are used to describe the applied potential, and the parameters σ and η, which determine the resulting density profile. For weak perturbations $\sigma = \tilde{\sigma}$, and η is related to $\tilde{\eta}$ via the compressibility $\partial\tilde{\rho}/\partial\mu \sim 1/U$ (μ is the chemical potential and $\tilde{\rho}$ the filling of the system). The background filling ρ_0 differs from the filling $\tilde{\rho}$ not only by the effect of the perturbation but also by boundary effects. Before we present our results on the time evolution of the density waves, we briefly review in the next section 4.4 the analytical approximation valid in the limiting regimes of very weak and very strong interaction to which we compare our results.

4.4. Analytical approximations

For *weak interactions*, or quite generally for a description of the long wavelength properties of a non-commensurate superfluid state, the continuum limit can be

performed by taking $Ja^2 = const$ and $a \to 0$. In this limit the Bose-Hubbard model becomes equivalent to the Lieb-Liniger model [91, 92]

$$\begin{aligned} H_{LL} &= \int \mathrm{d}x \left(\frac{1}{2M} |\partial_x \Psi(x)|^2 + V(x)\Psi^\dagger(x)\Psi(x) \right. \\ &+ \left. \frac{g}{2}(\Psi^\dagger(x))^2(\Psi(x))^2 \right), \end{aligned} \tag{4.4.0.3}$$

a bosonic model with δ-interaction of strength g and external potential V. Here Ψ is the bosonic field. The hopping parameter of the lattice model is related to the mass M of the atoms by $Ja^2 = \frac{1}{2M}$ and the onsite interaction strength to the δ-interaction strength by $Ua = g$.
Starting from this continuum model and considering the interaction in a mean field approximation, the Gross-Pitaevskii equation can be derived [12]. Within this approximation, the motion of density waves is described by the two coupled equations [11]

$$\begin{aligned} \frac{\partial \rho}{\partial t} &+ \frac{\partial (v\rho)}{\partial x} = 0 \\ M\frac{\partial v}{\partial t} + \frac{\partial}{\partial x}\left(\frac{M}{2}v^2 + V\right) &+ \frac{\partial}{\partial x}\left(g\rho - \frac{1}{2M}\frac{\partial_x^2\sqrt{\rho}}{\sqrt{\rho}}\right) = 0. \end{aligned} \tag{4.4.0.4}$$

Here $\rho = |\Psi|^2$ is the density and $v = \frac{1}{2\mathrm{i}M}\frac{\Psi^*\nabla\Psi - \Psi\nabla\Psi^*}{\rho}$ the velocity field. This equation gives a good description for systems in higher dimensions or one-dimensional systems with many particles per site. Linearizing the equations one recovers the results of the hydrodynamical approach [12].
We now turn to the opposite limit of *strong interactions*. For low densities $\tilde{\rho} \leq 1$ and strong interactions, the Bose-Hubbard Hamiltonian can be mapped onto an effective model of spinless fermions with correlated hopping and attractive interactions [93]:

$$\begin{aligned} H_F &= -J\sum_j \left(c_{j+1}^\dagger c_j - \frac{2J\hat{n}_j}{U} c_{j+1}^\dagger c_{j-1} + h.c. \right) \\ &- \frac{2J^2}{U}\sum_j \left(\hat{n}_{j+1} + \hat{n}_{j-1}\right)\hat{n}_j + O\left(J^3/U^2\right). \end{aligned} \tag{4.4.0.5}$$

Here c_j and $c_j^\dagger$ are the annihilation and creation operators obeying $\{c_j, c_{j'}^\dagger\} = \delta_{j,j'}$, and anti-commuting otherwise. $\hat{n}_j = c_j^\dagger c_j$ is the density operator. Due to the correction $O\left(J^3/U^2\right)$, this mapping is only valid for $u \gg 1$ assuming $J = 1$.
In the following we use units in which the lattice spacing $a = 1$, the hopping $J = 1$, and $\hbar = 1$. This means that times are measured in units of $\hbar/J$ and velocities in units of $aJ/\hbar$. In section 4.7 we compare the sound velocity of these models to our results obtained by the adaptive t-DMRG pointing out the different ranges of the validity of the approximations.

4.5. Evolution of the wave packet

Fig. 4.1 shows snap shots of the evolution of a density-wave packet created at time $t = 0$ obtained by the adaptive t-DMRG. The initially Gaussian wave

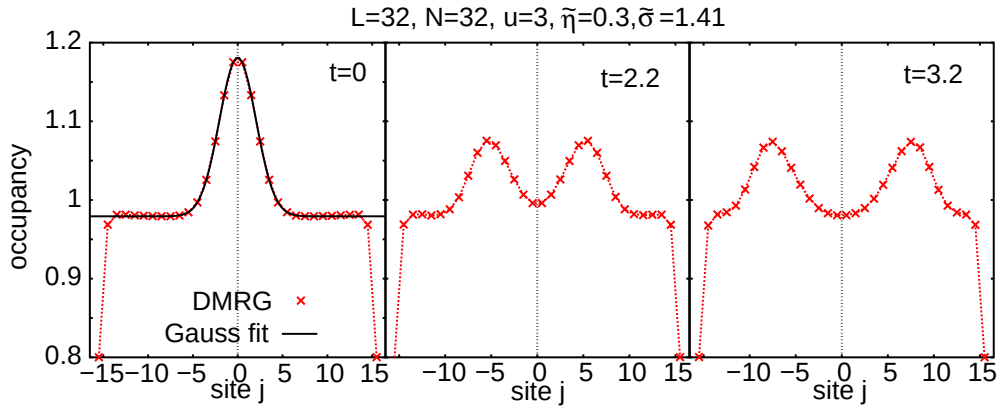

Figure 4.1.: Snap shots of the evolution of the density distribution are shown at different times. At $t = 0$, a Gaussian wave packet is present in the center of the system. It splits up into two packets which move with the same speed in opposite directions.

packet splits into two packets, which travel with the same speed into opposite directions. This is in agreement with the results obtained in the weakly interacting regime from a hydrodynamical approach. Within this approach, the evolution of an initially Gaussian wave packet of height η and background density $\bar{\rho}$ is determined by a linear wave equation, obtained by linearizing equations (4.4.0.4). The initial density wave splits up into two waves of the same form moving into opposite directions:

$$\rho(x,t) = \bar{\rho}[1 + \eta(\mathrm{e}^{-(x-vt)^2/2\sigma^2} + \mathrm{e}^{-(x+vt)^2/2\sigma^2})]. \tag{4.5.0.6}$$

For stronger interactions this simple description is no longer valid. The form of the initial density wave changes drastically as we will show in section 4.8.
In the finite systems of consideration the wave packets are reflected at the boundaries and travel towards the center where they meet again and the cycle restarts. The evolution of the density wave for up to four reflections is shown in Fig. 4.2 by a density plot, i.e. the height of the density is encoded in a grey-scale scheme (bright corresponds to high density and dark to low density). The bright lines indicate the motion of the wave packet, which splits into two packets moving towards the boundaries. After some time the pattern becomes less pronounced and a substructure arises due to the reflection and scattering of the wave packets.
Our numerical results for the time evolution of the density profile presented in this chapter were obtained using chain lengths between $L = 32$ and $L = 48$ sites. We ensured convergence in the number of states kept in the reduced space m (taken between $m = 64$ and $m = 96$), which means that the Suzuki-Trotter error dominates the total error (see Sec. 2.9). The errors in the determined observables are very small (of the order of 0.0001) for the used Suzuki-Trotter time steps $\Delta t = 0.01 - 0.05$ and can safely be neglected. For bosons the number of allowed states on each site has to be limited for numerical calculations. Typical values taken here are $N_B = 6$ and $N_B = 9$.

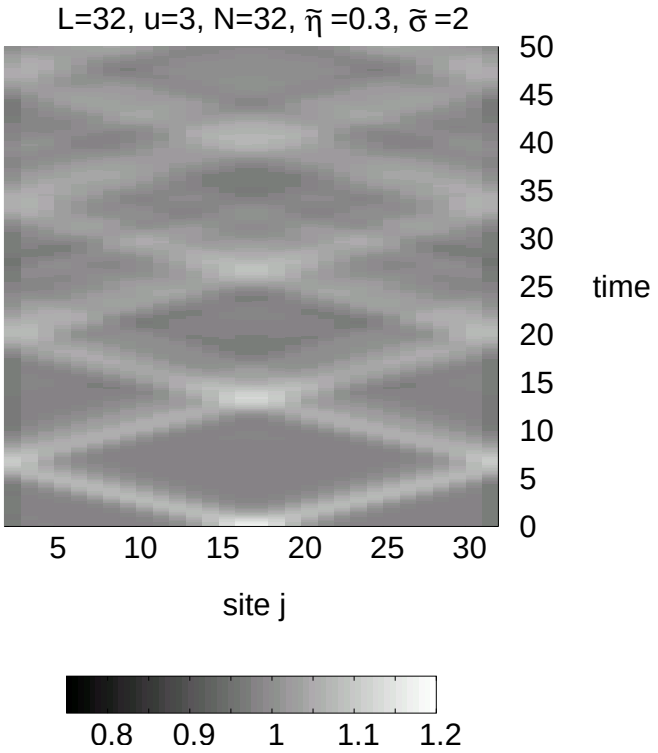

Figure 4.2.: The evolution of a density-wave packet is shown in a density plot. A linear grey scale is used, bright meaning higher densities. The bright lines correspond to the wave packets first splitting up moving towards the boundaries, being reflected by the boundaries and meeting again in the center of the system, where the cycle starts again.

4.6. Decay of the amplitude

In the previous section in Fig. 4.2 we have seen that the Gaussian structure of the wave packets at $t = 0$ becomes less pronounced in time. This decay of the wave packet is not only due to the reflection at the boundaries and the scattering at the other wave packet, but occurs as well in a homogeneous infinite system. In Fig. 4.3 this is shown by monitoring the maximal height of the density wave over time for two different amplitude heights and widths before the density wave reaches the end of the system. A decay of the amplitude is observed in both cases; for small times (in (a) for $t < 1$ and in (b) for $t < 2$) a very rapid decrease is seen, which is due to the splitting of the wave packet into two. For larger times after the two wave packets are separated, the decay is approximately linear in time (this might be just the first contribution of a more complicated decay). The decay of the amplitude of the initially small height $\tilde{\eta} \approx 0.1$ and width $\tilde{\sigma} \approx 1.4$ [Fig. 4.3 (b)] is much slower than the decay of the amplitude of the initial height $\tilde{\eta} \approx 0.3$ and width $\tilde{\sigma} \approx 1$ [Fig. 4.3 (a)]. The oscillations seen in the curve stem from the discrete structure of the lattice, since we plot the maximum value of the lattice occupancies over all lattice sites (and not the maximum of an fitted continuous curve which could lie between two lattice sites). The behaviour that the decay of the height of the perturbation becomes faster if (i) the width of the perturbation is narrower, and (ii) if the amplitude of the perturbation is higher is found at various parameters. It is in agreement with the qualitative picture one can obtain from analytical approximations. Damski [85] has shown that, neglecting the last term in the Gross-Pitaevskii equation (4.4.0.4), the so called quantum pressure term, the amplitude of the perturbation stays constant in time and equals $\bar{\rho}(1 + \eta)$. A decay of the amplitude in this approximation only occurs when the quantum pressure term becomes relevant. The quantum pressure term arises from the kinetic energy term and describes a restoring force due to spatial variations in the magnitude of the wave function of the condensate. It becomes important if the length scale of spatial variations is of the order of the healing length $\xi = 1/(\sqrt{2\gamma}\bar{\rho})$, where γ is the dimensionless interaction strength defined by $\gamma = \frac{Mg}{\bar{\rho}}$. Hence a decay of narrow or high wave packets is expected in agreement with our results.

4.7. Sound velocity

The sound velocity is one of the fundamental quantities of a Bose system. It is defined as the velocity of an infinitesimally small density perturbation. Since in our calculations we can only create perturbations with a finite amplitude we use an interpolation procedure to determine the sound velocity: we create two small density perturbations with low amplitudes, a "bright" one, i.e. $\eta > 0$, and a "grey" one, i.e. $\eta < 0$, ($|\eta| < 0.02$) at approximately the same background densities and interpolate between the two results for the velocities of these perturbations $\eta > 0$ and $\eta < 0$ linearly. This approach will be justified in section 4.8). The velocities for the bright or grey perturbations are determined from the propagation of the maximum or the minimum of the wave packet, respectively.

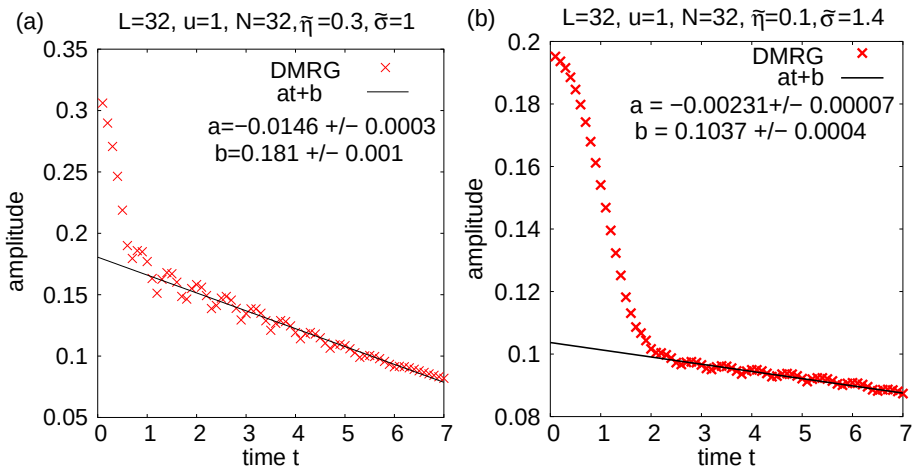

Figure 4.3.: The typical decay of the amplitude of the density perturbation. We plot $(\rho_j)_{\max} - \rho_0$, i.e. the difference between the largest discrete site occupancy and the background occupation.

In the remaining part of this chapter we investigate the dependence of the sound velocity on the interaction strength u and on the background density ρ_0 and compare our findings with analytical approximations with the theoretical predictions (compare section 4.4) from (i) a hydrodynamical approach or the linearized Gross-Pitaevskii equation, (ii) the approximation for the continuum gas by Lieb, and (iii) the results of the mapping onto a spinless fermion model.

(i) The sound velocity determined by a hydrodynamical approach is given by

$$v(\bar{\rho}, g) = \sqrt{\frac{g\bar{\rho}}{M}} = v_{\text{bare}} \frac{\sqrt{\gamma}}{\pi}, \tag{4.7.0.7}$$

where $v_{\text{bare}} = \frac{\pi\bar{\rho}}{M}$ is the analog of the bare 'Fermi' velocity. Using the relations of the continuum limit, the corresponding velocity in the lattice is

$$v(\rho_0, u) = 2\rho_0\sqrt{\gamma_{\text{lat}}}. \tag{4.7.0.8}$$

(ii) As will be shown below, a much wider range of applicability than (i) is obtained from the results of Lieb and Liniger for the continuous bosonic model (Eq. 4.4.0.3) with δ-interaction. They found two distinct modes of excitations, the usual Bogoliubov mode and the Lieb mode, which is associated with solitary waves [95]. At low momenta the dispersion relations for both modes have the same slope, which means that they propagate at the same sound velocity. The expression for the sound velocity can be obtained from the thermodynamic relation $Mv_s^2 = \bar{\rho}\partial_{\bar{\rho}}\mu$. Here μ is the chemical potential of the ground state, which is calculated within the Bogoliubov approximation. This results in [92]

$$v_s = v_{\text{bare}} \frac{\sqrt{\gamma}}{\pi} \left(1 - \frac{\sqrt{\gamma}}{2\pi}\right)^{1/2}. \tag{4.7.0.9}$$

In order to relate that to the Bose-Hubbard model, the expressions obtained from the continuum limit, i.e. $\gamma \to \gamma_{\rm lat}$ and $v_{\rm bare} \to v_{\rm bare,lat} = 2\pi\rho_0$ are used. Within the continuum model, the numerical calculation of the sound velocity by Lieb shows that expression (4.7.0.9) is quantitatively correct up to $\gamma \sim 10$. By contrast the hydrodynamical result Eq. (4.7.0.8) is valid only up to $\gamma \approx 1$.

(iii) For strong interactions the sound velocity obtained by a mapping onto a spinless fermion model is given by [94]

$$v_s^F \simeq v_F \left(1 - \frac{8}{u}(\rho_0 \cos \pi\rho_0)\right) \tag{4.7.0.10}$$

where the Fermi velocity of the lattice model is $v_F = 2 \sin \pi\rho_0$.

In Fig. 4.4 we compare the predictions (i)-(iii) for the dependence of the sound velocity on the interaction strength to our numerical results. To do this the sound velocity is plotted as a function of the interaction strength at fixed background density $\rho_0 \approx 0.52$. (The background density cannot be fixed easily to a certain value, since it depends on the total number of particles, the boundary effects and the perturbation. In our calculations it deviates from ρ_0 at most by 0.01. Note that for $\rho_0 = 0.52$ the relation $u \approx \gamma_{\rm lat}$ holds with $\gamma_{\rm lat} = u/2\rho_0$ being the lattice analogy of the dimensionless interaction.) We see that for small interaction strength, $u \lesssim 1$, i.e. $\gamma_{\rm lat} \lesssim 1$, the curves obtained using (i) and (ii) agree well with our numerical results. Around $\gamma_{\rm lat} \approx 1$ the mean field prediction (i) starts to grow too fast, while the approximation (ii) remains close to the numerical results up to intermediate interaction strength $\gamma_{\rm lat} \approx 4$. For even higher interaction strength also (ii) starts to differ significantly from our numerical results. This means that the lattice model starts to deviate from the continuum model, since (ii) was a very good approximation for the continuum model up to $\gamma \approx 10$. A breakdown of the continuum limit in this regime is expected, since the lattice analog of the healing length, i.e. $\xi_{\rm lat} = a/\left(\sqrt{2\gamma_{\rm lat}}\rho_0\right)$ becomes of the order of the lattice spacing a and thus the discreteness of the lattice becomes relevant (we restored here the dependence on the lattice spacing a). The sound velocity in the lattice model always remains lower than in the continuum model [compare (i) and (ii)]. For higher interaction strength the numerical results approach the asymptotic value of prediction (iii). Note, that the prediction (iii) is only expected to become valid for even stronger interactions than shown here, since it is an expansion in J^3/U^2. In Fig. 4.5 we see that our numerical results up to intermediate interaction strength show the dependence on the background density predicted by (ii) [cf. Eq. (4.7.0.9)]. Deviations from the predicted form occur for $\gamma_{\rm lat} \gtrsim 2$, depending on the particular set of parameters u and ρ_0. This dependence of the breakdown of the continuum limit ($\xi_{\rm lat}$ becomes of the order of a) is due to the fact that the healing length $\xi_{\rm lat}$ does not only depend on ρ_0 and u in the combination given by $\gamma_{\rm lat}$, but $\xi_{lat} = a/\sqrt{u\rho_0}$. Therefore the deviations at smaller values of u arise for larger background densities. Alternatively, this may be expressed in the form shown in Fig. 4.5: the breakdown of the continuum limit occurs for larger u at smaller $\gamma_{\rm lat}$.

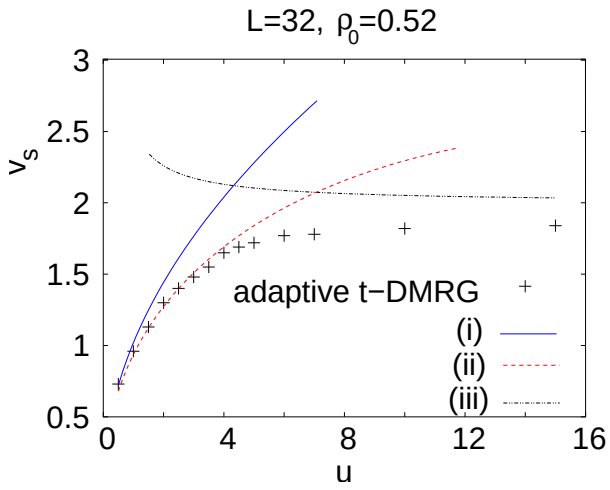

Figure 4.4.: The dependence of the sound velocity at constant background density $\rho_0 = 0.52$ on the interaction strength is shown (note $u \approx \gamma_{\mathrm{lat}}$). Our numerical results (+) are compared to (i) the results Eq. (4.7.0.8) of the hydrodynamical approach, (ii) the sound velocity determined by Lieb Eq. (4.7.0.9), and (iii) the results Eq. (4.7.0.10) for strong interaction strength obtained by mapping onto spinless fermions. The results of Eq. (4.7.0.10), i.e. (iii), should become applicable for even stronger interactions than the ones shown here. Recall that the velocities are measured in units of $aJ/\hbar$.

To summarize, we find that the sound velocity as a function of the interaction strength shows a crossover between (ii) [cf. Eq. (4.7.0.9)], where v_s/ρ_0 depends only on the combination of ρ_0 and u given by γ_{lat}, to a saturation at a value given by (iii) [cf. Eq. (4.7.0.10)]. In fact, a completely analogous behaviour appears in the average kinetic energy of the particles, allowing to identify the Tonks regime for quasi 1D tubes of bosons which are radially confined by a 2D optical lattice of increasing strength [90]. The breakdown of the prediction (ii) [Eq. (4.7.0.9)] is due to the discreteness of the lattice model and takes place if the healing length becomes of the order of the lattice spacing.

We add some more technical remarks on the determination of the sound velocity: The uncertainties introduced in the determination of the density profiles are negligible in comparison to the uncertainties introduced by the determination of the sound velocity. Curve of the location of the maximum (minimum) of the bright (dark) wave packet versus time is fitted by a linear fit to extract the velocity. For small interaction strength the velocity is relatively low and the movement over a long time can be fitted such that the accuracy of the results is of the order of ± 0.01 before interpolation between $\eta > 0$ and $\eta < 0$. For higher interaction strength, the uncertainty in the results for the velocity increases (approximately $O(\pm 0.05)$ for $u = 6$). This has two reasons: first, the velocity increases such that the end of the chain is reached in a rather short time. Moreover, oscillations in the density distribution induced at the end of

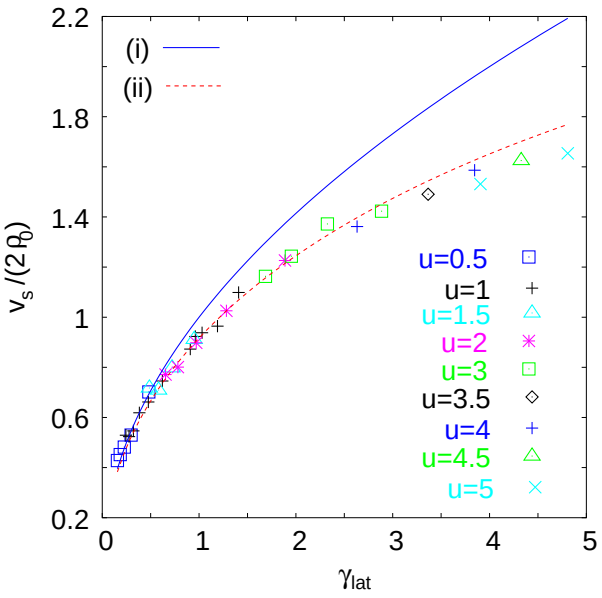

Figure 4.5.: The dependence of the sound velocity on the interaction strength and the background density is shown up to intermediate interaction strength. To show at which values of γ_{lat} the break down of the prediction (ii) (Eq. 4.7.0.9) occurs for different interaction strength u, we plot the ratio $v_s/(2\rho_0)$ versus $\gamma_{lat} = u/(2\rho_0)$. Recall that the velocities are measured in units of $aJ/\hbar$.

the chain due to the stronger interaction become more important and disturb the free evolution of the wave packets.

4.8. Self-steepening

In the previous section we studied the sound velocity which is important since it describes the elementary excitations in the system. In experimental setups also perturbations of finite strength play an important role. To investigate these in Fig. 4.6 the dependence of the velocity on the height of the initial density-perturbation amplitude is shown. The simulations were done at fixed interaction strength $u = 1$ and different background densities ρ_0. The dependence of the velocity on the density ρ_0 is taken out by dividing by $l(\rho_0) = \sqrt{2\rho_0}(1 - \frac{1}{2\pi}\frac{1}{\sqrt{2\rho_0}})^{1/2}$ using our knowledge from the previous results (cf. Eq. 4.7.0.9, with $\gamma = \gamma_{\mathrm{lat}} = u/2\rho_0$, and $u = 1$). Some technical remarks are in order: We determine the values for ρ_0, η, and σ, by fitting the initial wave packet at $t = 0$ to the form given by Eq. (4.2.0.1). Such a fit is shown in Fig. 4.1. We found that the errors made when reading off the parameters from the fit are much smaller than the size of the symbols used for data points in our plots (see for example Fig. 4.1). The error that results from assuming a time-independent amplitude η is negligible for small amplitudes and broad widths of the density perturbation, but should be taken into account for faster decaying amplitudes.

We see that for small amplitudes η, the dependence is approximately linear. It may be parameterized by $a\eta + b$ where $a = 0.8$ and $b = 1.1$. This linear dependence justifies the previously applied linear interpolation between $\eta > 0$ and $\eta < 0$ for the determination of the sound velocity.

As a consequence of the fact that the velocity increases monotonically with the amplitude of the perturbation, the wave can undergo self-steepening and shock wave formation can occur [85, 86]. One example where the phenomenon of self-steepening can be seen for a "bright" perturbation is shown in Fig. 4.7 (a). The form of the density wave becomes very asymmetric. The front of the density wave steepens and the back becomes shallower. An additional dip arises at the front of the density wave packet. This might stem from the discreteness of our system. In the case of a "grey" perturbation [Fig. 4.7 (b)], the asymmetry develops the other way round; the front becomes shallower and at the same time the back of the wave steepens. It should be emphasized, however, that the perturbations taken here are very narrow and high to obtain a clear signal. The Bose-Hubbard model might not be quantitatively applicable to describe such strong perturbations in the experiment as discussed in section 4.3.

4.9. Experimental observation

Experimentally, one way of detecting the density perturbation is to take time-of-flight images. As shown in section 3.7.1 the interference pattern can be

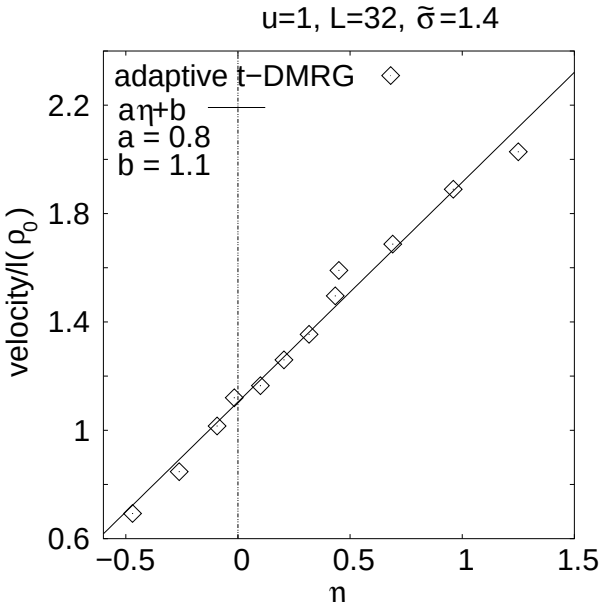

Figure 4.6.: The dependence of the velocity on the height of the amplitude η. The velocity is scaled by $l(\rho_0)$ to remove its dependence on the background density. Recall that the velocities are measured in units of $aJ/\hbar$.

determined from the Fourier transform of the one-particle density matrix

$$\rho(k) = 1/N \sum_{j,j'=1}^{L} \mathrm{e}^{\mathrm{i}(j-j')ak} \left\langle b_j^\dagger b_{j'} \right\rangle ,$$

neglecting its slowly varying envelope and the interaction between the atoms after switching off the trapping potentials. In a homogeneous system without a density perturbation a sharp interference peak appears at low interaction strength due to the long range order in the one-particle density matrix (see section 3.7). If the interaction increases beyond the point where a Mott-insulating phase is present, this peak broadens and decreases. Finally, for very strong interaction only a diffuse pattern is left. In the presence of a density-wave packet, we find that a second interference peak appears at a finite momentum. In Fig. 4.8 we show the difference between an interference pattern at $t = 0$, where the density wave is still in the center, and a later point $t = 5$, where the wave packets travel through the system. The possibility to resolve the second peak in the experiments depends on the parameters of the system. Specifically, the peak shown in Fig. 4.8 (a) was calculated for a high amplitude of the density perturbation. This ensures that the mean number of bosons contributing to the second peak in the interference pattern is a sufficiently large fraction of the total boson number.

Comparing our results to future experiments one should keep in mind that in the experimental realizations a parabolic trapping potential is present in addition to the periodic lattice. As a result, the background density is no

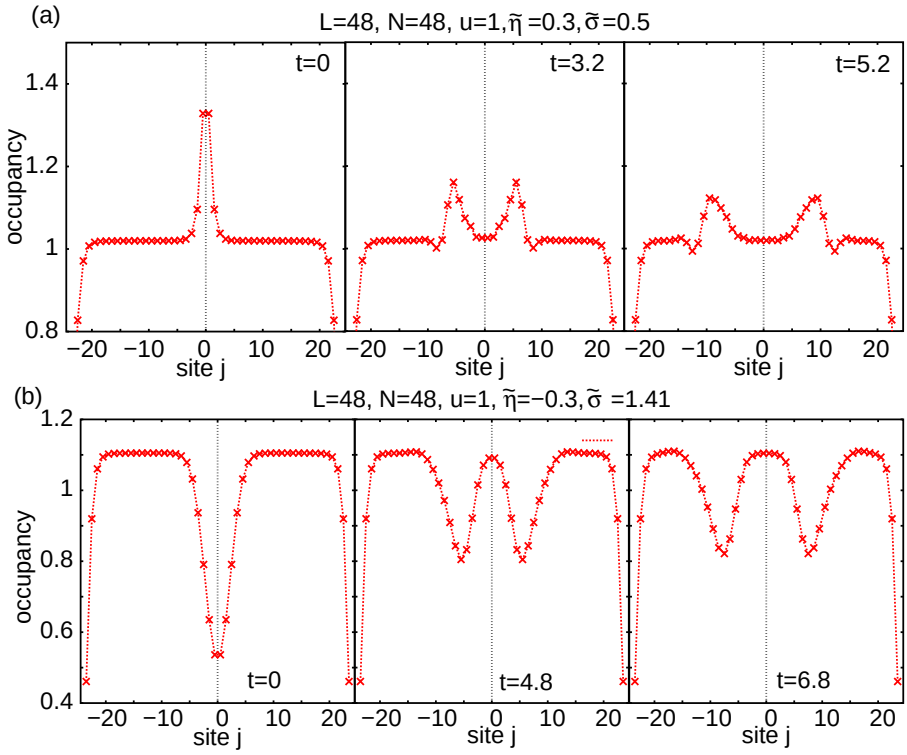

Figure 4.7.: The evolution of a narrow density-wave packet is shown for various fixed times. The wave packets undergo self steepening. The lines are guides to the eye.

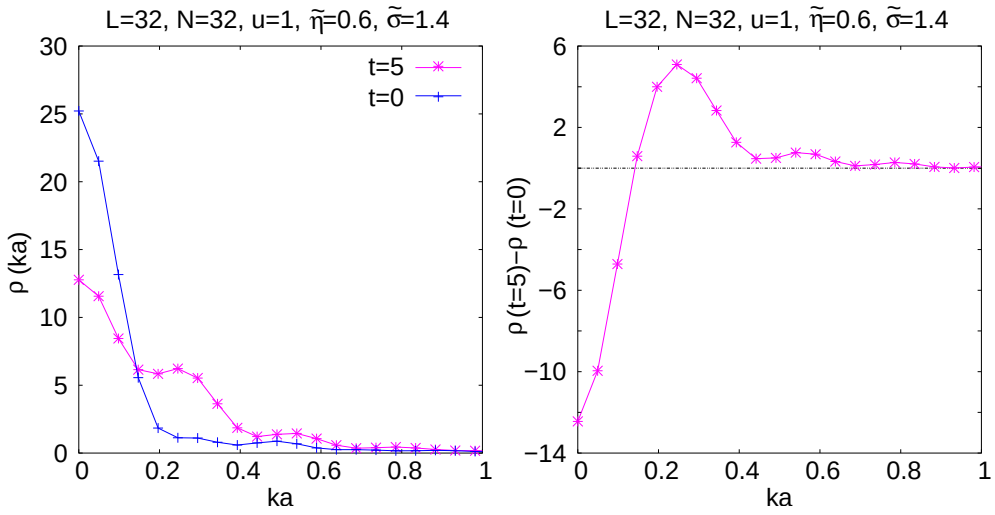

Figure 4.8.: On the left the interference pattern is shown for two different times. At $t = 0$ only one sharp interference peak at $k = 0$ exists. For times $t > 0$ further peaks at finite momentum k and $-k$ arise which correspond to the moving wave packets. Here only the region $k > 0$ is shown, exploiting a symmetry under $k \to -k$. On the right the difference of the interference pattern for $t = 5$ and $t = 0$ is shown. Here the errors are of the order of a few percent.

longer homogeneous (see section 3). Since the sound velocity depends on the background density, we expect it to vary for weak interactions according to Eq. (4.7.0.9) and for strong interactions according to Eq. (4.7.0.10). In the region where the trap varies slowly enough that the background density is almost constant, we expect the trap to have negligible effect on the motion of the wave packet such that we can directly compare our theoretical results to experiments.

4.10. Conclusion

We have shown that the adaptive t-DMRG allows us to study the motion of wave packets in a Bose-Hubbard model far beyond the regimes where commonly used approximations apply. This gave us the possibility to investigate the dynamics of density perturbations in ultracold bosons subjected to an optical lattice in many experimentally relevant situations. By comparing our results for the sound velocity to the results of different approximations we determine the regime in which they hold. The hydrodynamical approach or the linearized Gross-Pitaevskii equation agrees only well for rather weak interaction strengths and the continuum model holds up to intermediate interaction strengths. In contrast the fermionic model is only applicable for very strong interactions. The investigation of perturbations of experimentally realistic strength showed a decay of the amplitude and an approximately linear dependence of the velocity on the height of the amplitude. This dependence gives rise to interesting

effects like self steepening and shock wave formation which remain to be studied further. In the experiments the density wave may be detected as an additional peak in the interference pattern.
Let us conclude by mentioning a few open questions: In the exact solution of the continuum model by Lieb and Liniger there are in fact two independent types of excitations. One of them exhibits a generalized Bogoliubov type dispersion, which is linear at small momenta and crosses over to a quadratic free particle behaviour at large momenta. The other one only exists in a finite momentum range. It has been later identified as the solitary wave of the nonlinear Schrödinger equation in 1D [95, 96]. As was shown by Lieb and Liniger, the velocity of the dark solitons for repulsive interactions is always smaller than the linear sound velocity, coinciding with the latter only in the limit of long wave lengths. Experimentally, dark solitons have been observed in quasi 1D Bose-Einstein condensates, and have been identified by the fact that their velocity depends on the imposed phase gradient [83, 84]. In the case of a deep lattice potential, as is studied here, solitary waves are predicted to appear in the weak coupling regime $u \ll 1$ [97] and for sufficiently wide density perturbations which can be described by the 1D nonlinear Schrödinger equation. In addition, the presence of a lattice potential implies that atoms with momenta near a reciprocal lattice vector acquire a negative effective mass. This leads to the existence of bright gap solitons, a subject of considerable current interest [98, 99, 75], in particular in connection with instabilities for strongly driven optical lattices [100]. In this work we focused our investigations mainly on the case of perturbations with small momenta, for which the two modes cannot be distinguished by their velocity. It is an open question to which extent the density waves in our simulations, can be interpreted as solitary waves and in particular what happens to these stable excitations in the regime of strong coupling, where the nonlinear Schrödinger equation no longer applies.

5. Spin-charge separation in cold Fermi gases: a real time analysis

5.1. Fascinating physics in one dimension

In this chapter we turn to excitations in one-dimensional fermionic systems. In striking contrast to Fermi liquids, where the elementary quasiparticle excitations carry both charge and spin, the phenomenon of spin and charge separation is predicted for one dimensional systems by the Luttinger liquid picture [101, 102]. According to this picture - at low energy - the excitations of charge and spin completely decouple and propagate with different velocities. In condensed matter systems, numerous experiments have looked for spin-charge separation e.g. in 1D metallic wires [103], in 1D organic wires [104], in carbon-nanotubes [105], and in quantum wires in semiconductors, where the different velocities have now clearly been observed [106]. In addition Recati et al. [72] suggested to study the phenomenon of spin-charge separation using ultracold fermions in atomic wires. The experimental realization is now in reach by the recent creation of ultracold Fermi gases in an 'atomic quantum wire' configuration. This is an array of thousands of parallel atom waveguides, which are created by a very strong two dimensional optical lattice [107]. The advantage of the use of systems of ultracold atoms lies in the possibility of both the tuning and the quantification of the interaction, allowing quantitative comparison between theory and experiments. Moreover, using a very strong axial confinement, for atomic wires 3D effects are negligible, thus avoiding the possibility to mistake experimentally Fermi liquid collective spin and charge density modes for the different ones in 1D. We will propose yet another experiment to observe spin-charge separation effects using these very clear and tunable systems of ultracold atoms. Our proposal does not encounter the problems which still trouble the approach of Recati et al. (see below).
The analysis of Recati et al. [72] is essentially based on the hydrodynamic Hamiltonian of the Luttinger liquid. The inhomogeneity due to the presence of a harmonic trap is treated within a local density approximation (see also [108]). Clearly, such an approach is only valid at low energies. It requires very weak perturbations and length scales much beyond the average interparticle spacing. In reality, with typically less than 100 atoms per atomic wire [107], stronger and more localized perturbations are required to produce observable effects. In addition, the effect of boundaries, where the local density approximation breaks down, are of crucial importance. For a quantitative description of spin-charge separation in 1D cold Fermi gases, it is thus necessary to use a microscopic description like the Hubbard model and to treat properly the inhomogeneous case with realistic system sizes. Due to the short range nature of the interac-

tions between cold atoms, the Hubbard model is indeed a perfect description of a situation, in which there is an additional optical lattice along the weakly confined axial direction (for bosons cf. section 3.2). Hereby the spin degrees of freedom in the Hubbard model correspond to two different hyperfine levels in the system of ultracold fermions, and the 'charge' density is the particle density. Despite this we will use the terms of 'spin' and 'charge' also in the context of ultracold fermions. For the realistic case of low filling, the hopping matrix element J and the on-site Hubbard repulsion U can be straightforwardly obtained from the known lattice parameters and the scattering length [cf. Eq. (3.2.0.3) and Eq. (3.2.0.4)]. It is the aim of the present chapter to study the phenomenon of spin-charge separation within a time-dependent calculation of a microscopic model for parameters which would be realistic in an experiment with cold atoms [109].
We start by introducing the one-dimensional Hubbard model (section 5.2) and its phases (section 5.3), before we introduce in section 5.4 the phenomenon of spin-charge separation. In section 5.5 we give details on the perturbations considered. In section 5.6 we show our results for the real-time evolution of spin and charge perturbations of finite strength. An experiment to observe the effect of spin-charge separation in systems of ultracold fermions is proposed in section 5.7, before we discuss in section 5.8 the parameters which need to be achieved in such an experiment.

5.2. Hubbard model

Our starting point is the standard Hubbard model

$$\begin{aligned} H = \quad & -J\sum_{j,\sigma}\left(c^{\dagger}_{j+1,\sigma}c_{j,\sigma}+h.c.\right)+U\sum_{j}n_{j,\uparrow}n_{j,\downarrow} \\ & +\sum_{j,\sigma}\varepsilon_{j,\sigma}\hat{n}_{j,\sigma} \end{aligned} \tag{5.2.0.1}$$

the fermionic analog of the Bose-Hubbard model Eq. 3.2.0.2. Its parameters are the hopping matrix element J, the on-site repulsion $U > 0$ between fermions of opposite spin $\sigma = \uparrow, \downarrow$ at sites $j = 1, \ldots, L$ and a spin-dependent local on-site energy $\varepsilon_{j,\sigma}$, describing both a possible smooth harmonic confinement and time-dependent local potentials which allow to perturb the system. One introduces a 'charge' density $n_c = n_\uparrow + n_\downarrow$ and a 'spin' density $n_s = n_\uparrow - n_\downarrow$. Similar to bosons in an optical lattice (section 3.2), the ratio $u = U/J$ between the on-site repulsion U and the hopping J can easily be changed experimentally by varying the depth V_0 of the optical lattice. We use units where both J and $\hbar$ are equal to one; thus time is measured in units of $\hbar/J$.

5.3. Quantum phase diagram

The ground state of the Hubbard model can be determined exactly by the Bethe ansatz [110], but due to its complicated structure the evaluation of physical

quantities like correlation functions remains quite involved. As in the Bose-Hubbard model two different phases occur in the Hubbard model: a liquid phase and a Mott-insulating phase. At half filling, i.e. $n_c = n_\uparrow + n_\downarrow = 1$, even an infinitesimal small interaction U causes a Mott-insulating state, whereas at fillings different from half filling only the liquid phase occurs. Therefore only the analogue of the commensurate-incommensurate phase transition of the bosonic case (cf. section 3.3) exists.
The lowest excitations in the system are two collective modes, the spin and the charge mode. In the liquid phase both of these are gapless with a linear spectrum. In contrast in the Mott-insulating phase for the charge mode a gap opens up which causes the insulating behaviour, whereas the spin mode stays gapless. In the limit of infinitely strong interaction the two modes decouple not only for low energies and the spin part of the Hamiltonian becomes equivalent to the antiferromagnetic Heisenberg model with an exchange constant $4J^2/U$.

5.4. Spin-charge separation

A simple picture for the effect of spin-charge separation can be gained considering a chain at half filling with very strong interaction U between the different species. The strong interaction induces an antiferromagnetic behaviour as sketched in Fig. 5.1 (a). Removing a fermion from the chain [Fig. 5.1 (b)] changes both the spin and the charge quantum number. Two excitations are created in this case:
(i) a *holon* [circle in Fig. 5.1 (c)], a charge is lacking, but the spin environment is purely antiferromagnetic and
(ii) a *spinon* [ellipse in Fig. 5.1 (c)], two neighbouring spins are aligned, but no charge is missing.
In one dimension once created the holon and the spinon can move independently and freely —without any additional cost in energy— through the chain, by first and second order hopping processes, respectively. Thus any single-particle excitation dissociates into these elementary excitations. In contrast if a fermion is removed from a system of higher dimension the spinon and the holon are held together by the frustration which is created by the neighbouring chains as marked by the box in [Fig. 5.1 (d)]. A penalty in the energy has to be paid if the spinon and holon separate. Therefore, the fermionic single-quasiparticle excitation has a finite life time and does not split up immediately as in the one-dimensional case.
More technically this phenomenon can be described by the hydrodynamical approach [70, 102], which covers the low energy properties of the one-dimensional system. In this approximation the degrees of spin and charge decouple completely for any strength of interaction. This becomes obvious using these degrees of freedom to express the Hamiltonian:

$$H = H_s + H_c \quad \text{with} \tag{5.4.0.2}$$

$$H_\nu = 1/2 \int \mathrm{d}x \left(u_\nu K_\nu \partial_x \theta_\nu^2 + \frac{u_\nu}{K_\nu} (\partial_x \phi_\nu)^2 \right). \tag{5.4.0.3}$$

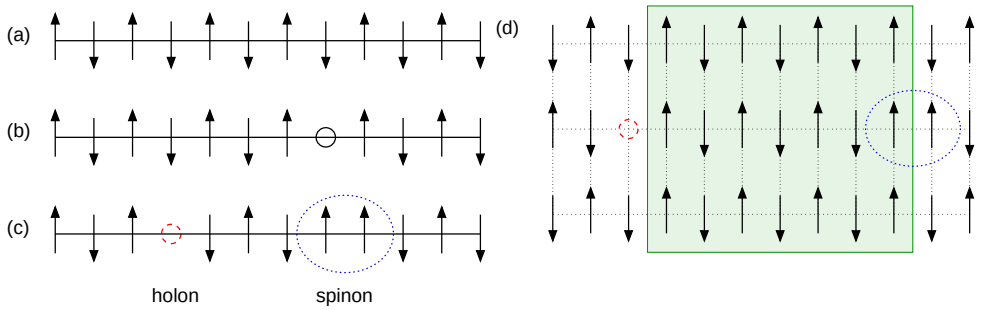

Figure 5.1.: Left: Sketch of the splitting of a single-particle excitation [circle in (b)] into a holon [circle in (c)] and a spinon [ellipse in (c)] in an one-dimensional system. Right: In higher dimension (d) the spinon and the holon are held together by the influence of the neighbouring chains [block in (d)] and thus single-quasiparticle excitation have a finite life time.

Here θ_ν and ϕ_ν are bosonic fields describing the phase and the density fluctuations of the spin $\nu = s$ and the charge $\nu = c$, respectively. The parameters u_ν are the 'sound' velocities, while K_ν are related to the low energy behaviour of the correlation functions. Since the Hamiltonian splits into a charge and a spin part, both modes are totally decoupled. The hydrodynamical approach therefore predicts the spin-charge separation for low energies. However, stronger perturbation which are necessary for the experimental detection cannot be described by this approach. It is an advantage of the adaptive t-DMRG that we can study the dynamics of the Hubbard model using initial perturbations of various strengths.

5.5. Preparation of the perturbation

In the investigation of the evolution of density perturbations we focus on three different types:

(i) perturbations in the density of the ↑-fermions; thereby a perturbation in both the spin and the charge density is created.

(ii) perturbations in the charge density

(iii) perturbations mainly in the spin density.

To prepare these different cases of perturbations we apply localized external potentials of different type in Eq. (5.2.0.1):
(i) $\varepsilon_{j,\uparrow}(t) = f(j,t)$,
(ii) $\varepsilon_{j,\uparrow}(t) = \varepsilon_{j,\downarrow}(t) = f(j,t)$, and
(iii) $\varepsilon_{j,\uparrow}(t) = -\varepsilon_{j,\downarrow}(t) = f(j,t)$.
A Gaussian form of the perturbations is chosen

$$f(j,t) \propto \exp^{-(j-j_0)^2/(2\sigma^2)}\ \theta(-t), \tag{5.5.0.4}$$

with variance $\sigma = 2$ centered at site j_0. The strength of the perturbation is varied. For each case the external potential is assumed to have been switched on slowly enough for equilibration and is then switched off suddenly at time $t = 0$. We determine the initial state as the ground state of the corresponding Hamiltonian (5.2.0.1) at $t = 0$ for an equal number of spin-up and spin-down fermions, $N_\uparrow = N_\downarrow = N/2$ using a finite-system DMRG-algorithm. For relatively weak potentials the resulting density perturbations are approximately of Gaussian form Eq. (4.3). The height of the charge and spin density perturbations will be denoted by η_c and η_s, respectively, and the charge background density by n_0.
In the experiments the perturbations (i)-(iii) may be generated by a differently far blue- or red-detuned laser beam tightly focused perpendicular to an array of atomic wires, which generates locally repulsive or attractive potentials for the atoms in the wires. These perturbations due to an external laser field are quite strong, typically of the order of the recoil energy E_r.
In the calculations presented the lengths of the chains were chosen up to $L = 128$ sites, keeping of the order of several hundred DMRG states. DMRG error analysis reveals that all density distributions shown here are for all practical purposes exact, i.e. with controlled errors of less than $O(10^{-3})$.

5.6. Spin-charge separation: beyond small perturbations

In this section we study the propagation of spin and charge perturbations in a homogeneous system, i.e. in a system without an additional trapping potential. We investigate, in particular, the dependence of their propagation velocities on the strength of the perturbation. In this section the perturbations are chosen to be centered at $j_0 = (L + 1)/2$ to minimize boundary effects.
We start with a homogeneous system which is perturbed by a potential of type (i) localized at the chain center. In Fig. 5.2 (a) the density distributions close to the density distributions of the initial state are shown as obtained by DMRG with the perturbation at the chain center. The external potential, Eq. (5.5.0.4), generated a dominant perturbation in the $\uparrow$-Fermion distribution by direct coupling and, indirectly, a smaller perturbation in the $\downarrow$-density due to the repulsive interaction between the different spin species. Note, that due to the presence of the spin perturbation a slight mismatch in the background densities of the $\uparrow$- and the $\downarrow$- fermions is induced by the fixed number of the $\uparrow$- and the $\downarrow$-fermions. The wave packets in $\uparrow$- and $\downarrow$-density perform a complicated time evolution [Fig. 5.2 (a)-(c)] which is due to their repulsive interaction. In contrast, the resulting perturbations in the spin and charge density evolve more or less as non-interacting perturbations. Both perturbations split into two wave packets each of which moves outwards. Their respective velocities are found to be different as indicated by the arrows in Fig. 5.2 (c). The charge perturbation has moved out further than the spin perturbation at the same point of time, such that spin and charge have separated. To our knowledge, this is the first time that the different velocities of spin and charge are obtained numerically in a microscopic model for systems of a size suitable for comparison

with experiments.

It is always illuminating to compare numerical results to analytical solutions when available. From the Bethe ansatz [110, 111, 112, 113, 114] both spin and charge velocities are known analytically in the limit of an infinitesimal perturbation much broader than the average interparticle spacing.

To compare our numerical findings to the exact charge velocity, we create pure *charge density perturbations*, by applying the potential of type (ii), and calculate their time evolution after switching off the potential. The charge velocity is determined from the propagation of the maximum (minimum) of the charge density perturbation for bright (amplitude $\eta_c > 0$) and grey ($\eta_c < 0$) perturbations, respectively. In Fig. 5.3 the charge velocities for various background densities n_0 and perturbation amplitudes η_c are shown. We find good agreement between the exact result of the Bethe ansatz for the 'sound' velocity of the charge and our numerical results for the charge velocity, if we plot our results of the charge velocity versus the charge density at the maximum (minimum), i.e. $n_c = n_0 + \eta_c$. The velocity of the maximum (minimum) of the wave packet is therefore mainly determined by the value of the charge density at the maximum (minimum), and not by the background density.

As we mentioned before in the experiment the perturbations generated by an external laser field are quite strong. The theoretical description of the evolution of these finite strength perturbations is not trivial at all and indeed, has never been studied before. Numerically, we find that even for strong perturbations $\eta_c \approx \pm 0.1$ which corresponds to 20% of the charge density, the phenomenon of spin-charge separation remains valid and the charge velocity only depends on the charge density at the extremum of the perturbation n_c. The charge velocity is thus robust against separate changes of the background density n_0 and the height of the perturbation η_c.

The uncertainties in Fig. 5.3 which are of the order of the symbols have their origin not in the uncertainties in the evolution of the density distributions which have controlled errors less than 10^{-3}, but stem mainly from the fitting of the motion of the maximum/minimum and the presence of oscillations in the background density.

To study the behaviour of the *spin perturbation* we apply a local potential of type (iii) which mainly generates a spin perturbation. In contrast to the charge perturbation, we find in Fig. 5.4 that the velocity of a spin perturbation varies strongly with its height η_s. The velocity of the finite perturbation approaches the 'sound' velocity of the spin, the solution of the Bethe ansatz, from below. The interpolation to an infinitesimal spin perturbation has to be taken with care due to the strong variation at low spin amplitude η_s. These results show once more the importance to investigate perturbations of finite strength in order to obtain quantitatively reliable results for comparison with experiments.

It remains to be studied further, if the origin of the change of the velocity is purely the height of the spin perturbation or whether the slight difference in the background densities for $\uparrow$- and $\downarrow$-fermions —induced by the fixed total number of $\uparrow$- and $\downarrow$-fermions— contributes as well.

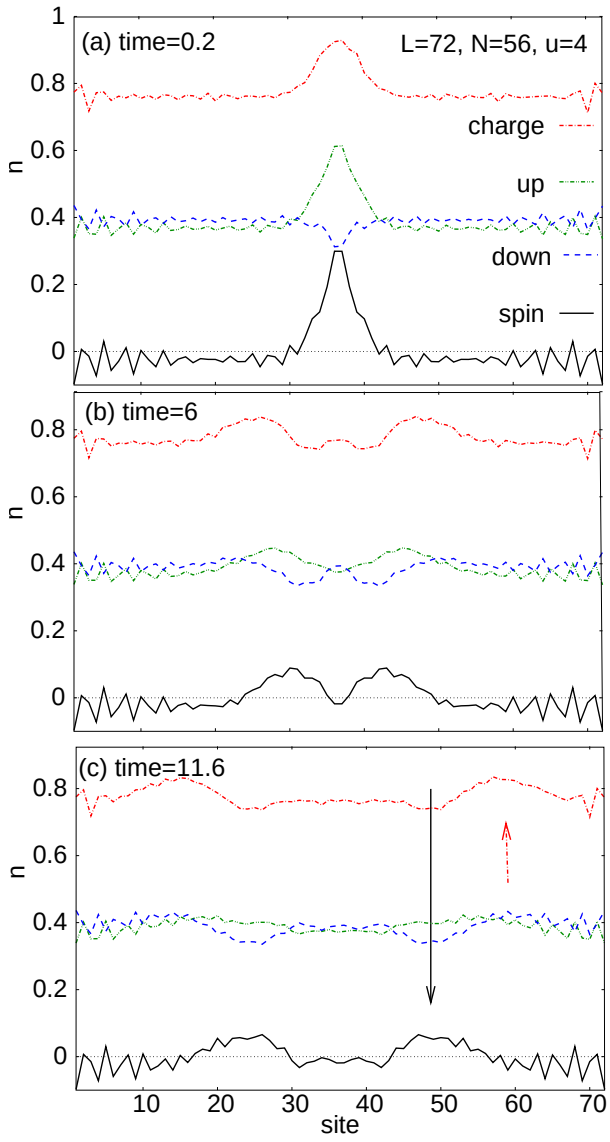

Figure 5.2.: Snapshots of the evolution of the density distributions at different times. At $t = 0$, a wave packet is present in the center of the system in both the spin and the charge density. Each of these splits up into two packets which move with the same velocity in opposite directions. The velocity of the propagation of the charge wave and the spin wave are different. $U/J = 4$, charge background density $n_0 = 0.78$.

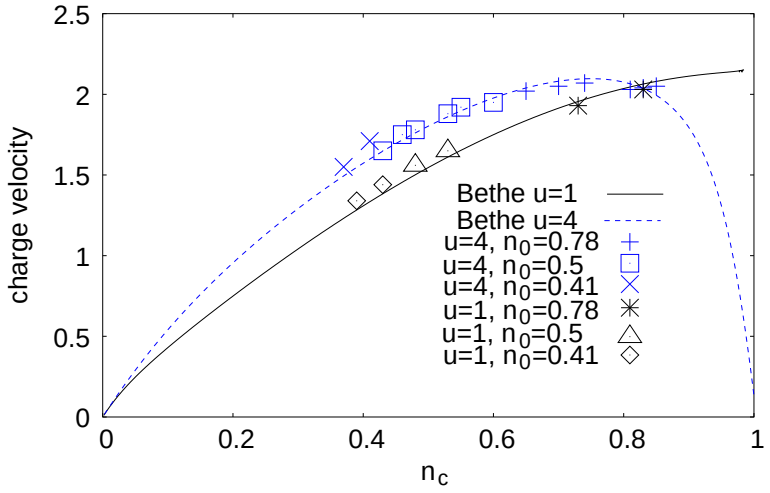

Figure 5.3.: Exact results for the charge velocity obtained by the Bethe ansatz (lines) are compared to the numerical results of the adaptive t-DMRG. The numerical results correspond to different heights of the perturbations at various charge background densities n_0. n_c is the charge density at the maximum/minimum of the charge density perturbation. The uncertainties are of the order of the size of the symbols and stem mainly from the determination of the velocity which is complicated by the presence of oscillations in the background density.

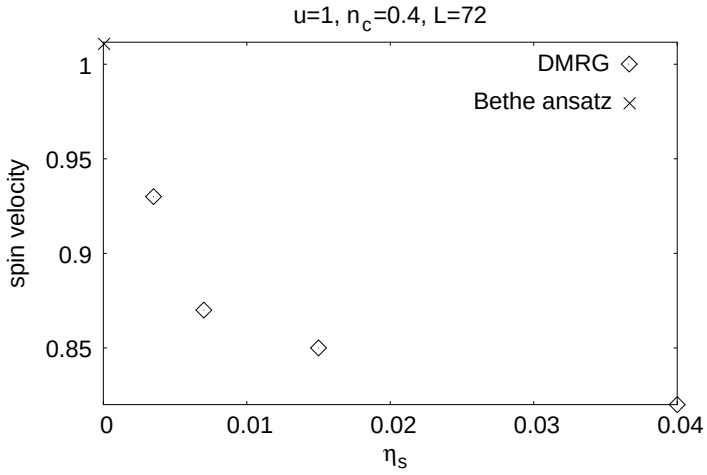

Figure 5.4.: Spin velocity for different strength η_s of the spin density perturbation. The cross marks the Bethe ansatz result for the 'sound' velocity.

5.7. Proposed experimental realization

To study the separation of spin and charge experimentally in systems of ultracold atoms, the first idea would be to perturb the system by a localized potential and to observe the evolution of the perturbation by measuring the densities in a certain region of the system. However, in a single one-dimensional system the signal would be very low and in an experiment with arrays of parallel atomic wires, the different filling in individual wires would lead to a signal broadening due to the resulting differences in velocities. In order to avoid these problems, we suggest to look for spin-charge separation in a completely different way. Our proposal relies on the coexistence of a Mott-insulating state and a liquid state in spatially separated regions of the system as it can be the case in the presence of a parabolic trapping potential $\varepsilon_{\sigma,j} = -V_t a^2 (j - L/2 + 0.5)^2 E_r$ (section 3.4, [115]). The idea is to use the very different behaviour of the charge and spin degrees of freedom in the Mott-insulating phase. In this phase the charge excitation spectrum has a gap, whereas the spin dispersion is still linear for small momenta, and the spin velocity is finite. By contrast, in the liquid phase both excitation spectra are linear for small momenta. To exploit this difference in the behaviour, assume the system of one-dimensional wires confined by a trapping potential which is prepared in such a way, that a Mott-insulating region is present in the center of most of the wires. In these Mott-insulating regions the charge density is locked to half-filling, $n_c = 1$. At the boundary of the Mott-insulating regions liquid regions exist. A localized potential which couples to one species [of type (i) section 5.5] in the liquid region will then create spin and charge density perturbations. While the spin density perturbation can evolve unhindered, the charge density perturbation cannot penetrate the Mott-insulating region due to its gapped spectrum. This effect can be seen from Fig. 5.5 in which calculated snapshots of the time evolution in such a situation are shown. In Fig. 5.5 (a) the perturbation, centered around site 10 is clearly seen in the spin density and in the density of the $\uparrow$- and $\downarrow$ - fermions. In the charge density the perturbation enlarges the region where the charge density is locked, i.e. $n_c = 1$. We point this out by sketching the idealized charge density profile without the perturbation in Fig. 5.5 (a). In Fig. 5.5 (b) and (c) the density distribution at later times are shown. Evidently, the spin density wave propagates into the Mott-insulating region, whereas the charge density perturbation is almost completely reflected due to the charge gap in the Mott-insulating region. The presence of spin density oscillations which are due to the anti-ferromagnetic coupling induced by the interaction obscures the exact evolution of the spin perturbation. However by averaging over several lattice sites — as it is necessary within current experimental techniques, anyway — the effect of spin-charge separation is clearly visible. In Fig. 5.6 examples for the evolution of the sum of the charge and the spin number of particles between site 25 and 35, N_c and N_s, are shown. It is clearly seen that the sum of the charge occupation does not change, whereas the spin occupation shows the moving wave packet. The average spin velocity can be determined from Fig. 5.6 if the distance between the localized potential which generates the perturbation and the center of the region over which the density is measured is known. Here, the

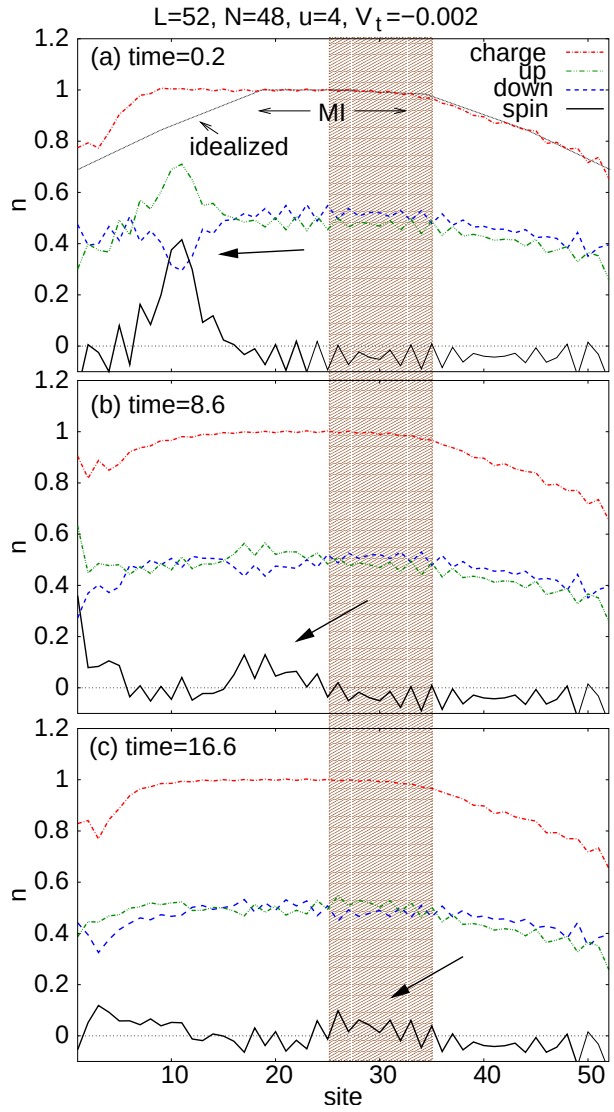

Figure 5.5.: The time evolution of charge and spin density perturbations in the presence of a parabolic trapping potential. MI marks the approximate Mott-insulating region in the absence of the perturbation. The line denoted by idealized is a sketch of the charge density distribution without the perturbation. The presence of the perturbation enlarges the region in which the charge density is locked to $n_c = 1$. The arrows show the approximate place of the spin perturbation, and the shaded region marks the region over which the densities are averaged (cf. Fig. 5.6).

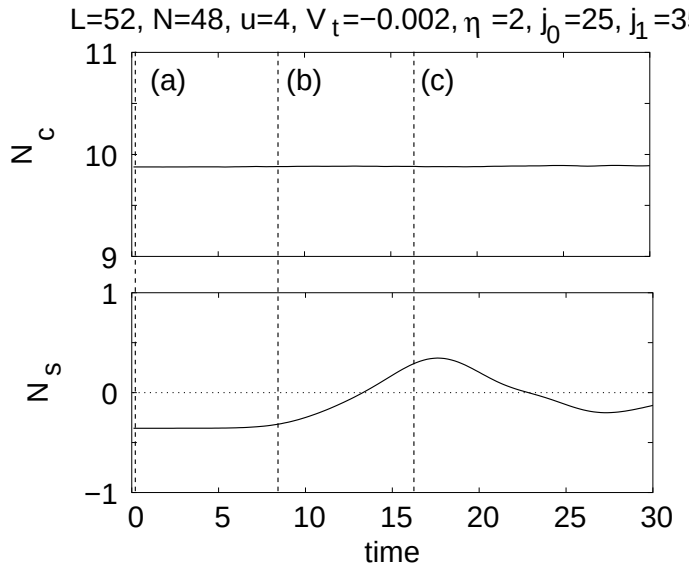

Figure 5.6.: Time evolution of the charge and spin density summed over the sites $j_0 = 25$ to $j_1 = 35$. Vertical lines correspond to the times of the snapshots in Fig. 5.5

spin velocity is found to be $v_s \approx 1.1J/\hbar$ which agrees nicely within the expected accuracy with the value of $v_s(n_c = 1) = 1.2J/\hbar$ of the Bethe ansatz.
The very different propagation behaviour of charge and spin can as well be used experimentally to distinguish between a Mott-insulator and a band insulator: In a band insulator not only the velocity of the charge, but also that of the spin would vanish, whereas, as used above, in the Mott-insulator the spin velocity stays finite.

5.8. Experimental parameters

In order to quantify the requirements for an experimental observation of spin-charge separation in cold Fermi gases, we discuss typical parameters which need to be achieved in a setup with an array of atomic wires [107]. Such an array consists of several thousand parallel wires with typically less than 100 ^{40}K atoms each. In addition to the smooth axial confinement potential with frequency $\omega_z \approx 2\pi \cdot 275$Hz (corresponding to $V_t \approx -0.0035$), the realization of a 1D Hubbard model requires adding a strong periodic potential along the tubes as it has already been realized for bosonic atoms. For ^{40}K and a standard lattice constant $a = 413$ nm, the recoil energy is $E_r \approx 7$kHz. An optical lattice of height $V_0 = 15E_r$ then gives an on-site repulsion $U \approx 0.17E_r$, where we have used a standard value for the s-wave scattering length $a_s \sim 174a_0$ between the levels $F = 9/2$ $m_F = -9/2$ and $m_F = -7/2$ [116]. The resulting ratio of the interaction and the kinetic energy $u \approx 22$ leads to a central Mott-insulating region in most of the tubes with a typical size of the order of twenty sites. With these parameters, the time in which the spin wave travels 20 sites is of

the order of a few ms. The creation of state selective potentials for two different hyperfine states may be done by using laser light whose frequency falls between the respective transitions. This might be difficult for the $F = 9/2$ $m_F = -9/2$ and $m_F = -7/2$ levels, but should be possible - for instance - using $F = 9/2$ and $F = 7/2$ levels. The $1/e^2$-radius of the potential (Eq. 5.5.0.4) is taken to be four lattice sites, which corresponds to a laser with an approximate $1/e^2$-radius of $2.1\mu m$. Finally, to ensure that finite temperature does not destroy the Mott-insulating behaviour by thermal activation, the energy scale $k_B T$ should be smaller than the Mott energy gap. In recent experiments the temperature reached was about $T \sim 0.1 T_F$, where T_F is the temperature set by the Fermi energy. Approximating the Fermi temperature by $E_F \sim N/2\omega_z$, here N is the particle number and ω_z the axial trapping frequency, the energy scale set by the temperature is $k_B T \sim 0.6 E_r$. This is about three to four times the gap in the Mott-insulating phase $U \sim 0.17 E_r$ for $V_0 = 15 E_r$. Therefore, already the very first experiment of 1D fermions in an optical lattice [107] is very close to matching those conditions. Improvements can be made, e.g., by reducing the axial confinement frequency such we expect that the necessary regime can be reached in near future.

5.9. Conclusions

We have performed the first numerical simulations of the time evolution of charge and spin density perturbations in real time in 1D Hubbard systems of sizes comparable to experiments. From this it becomes evident that the separation of spin and charge is a generic feature of 1D interacting fermions, far beyond the low-energy regime where a Luttinger liquid description applies. This opens the possibility to observe spin-charge separation experimentally in systems of ultracold atoms. We propose an experiment in which the different propagation behaviour of spin and charge perturbation in the liquid and the Mott-insulating phases is used to observe the spin-charge separation in an array of one-dimensional systems of ultracold fermions. We expect that the experimental parameter regimes necessary will become accessible in near future. Thus the experimental evidence for the existence of spin-charge separation could be strengthened considerably relating the experimental findings to theoretical predictions. Hereby the good control and microscopic knowledge about the parameters like the interaction strength make the systems of ultracold fermions advantageous. Further the same experimental setup could distinguish a Mott-insulator and a band insulator, one very important proof for the importance of the interaction in these systems. Let us mention that a modification of this setup by creating an excitation with single-particle character instead of the density perturbation would allow to contrast the behaviour in one and three dimensions. Whether such a single-particle excitation can be created and detected experimentally in these systems, remains to be shown.

6. Transport in spin-$1/2$ chains

6.1. Introduction

The transport properties of spin chains have attracted much attention recently, due to the possible applications to information storage, spintronics, and quantum information processing. In this chapter, we study a highly simplified picture for spin transport between two coupled reservoirs of opposite spin polarization [117]. This is done by investigating the time evolution of an initial state $\left|\uparrow \ldots \uparrow\downarrow \ldots \downarrow\right\rangle$, i.e. with all spins on the left half of the chain pointing up along the z-axis modeling one of the reservoirs, and all spins on the right half pointing down modeling the second reservoir. The spins are coupled by nearest-neighbour spin interaction (see Eq. 6.2.0.1) [117]. We are mainly interested in the following questions: Does the state evolve into a simple long time limit? If so, how is this limit reached? On what properties does the long time behaviour depend?
Analytical results for this problem are essentially restricted to the XX-chain with and without dimerization which is amenable to an exact solution [118, 119]. In Ref. [118], a scaling relation for the long-time limit was found. However, it is presently not known whether this relation is general, or whether it relies on special properties of the XX- model. If a long-time limit exists for other models as well, the question arises which of its characteristics are universal, and which depend on certain system properties. We will address these questions in the following.
As so far no detailed error analysis of the adaptive t-DMRG has been performed, an important aspect of the present chapter is that besides their own physical interest, spin-1/2 chains provide an excellent benchmark for the adaptive t-DMRG, because of the nontrivial exact solution for the XX-model, against which the method can be compared. This allows to analyze the accuracy of the adaptive t-DMRG explicitly, namely to address the questions what kinds of errors can occur in principle, which ones of these dominate in practice, and how they can be minimized.
The outline of the chapter is as follows: In section 6.2 we introduce the model and its characteristics. In section 6.3 a detailed error analysis is performed. In section 6.4 we present our results for the long time limit of the time evolution for different interaction and dimerization strength.

6.2. Model and initial state

In this chapter we analyze the dynamics of the inhomogeneous initial state $\left|\text{ini}\right\rangle := \left|\uparrow \ldots \uparrow\downarrow \ldots \downarrow\right\rangle$ on the one-dimensional spin-1/2 chain with interactions

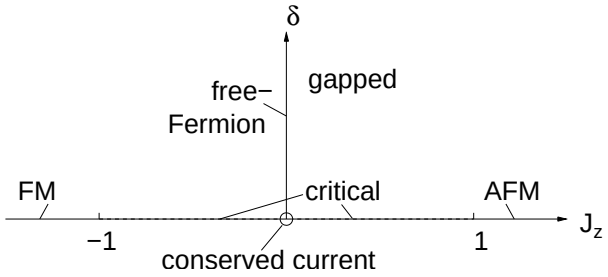

Figure 6.1.: Quantum phase diagram of the Heisenberg model, Eq. (6.2.0.1). See [120, 121] for details.

given by the Heisenberg model

$$H = \sum_n J_n (S_n^x S_{n+1}^x + S_n^y S_{n+1}^y + J_z S_n^z S_{n+1}^z) \equiv \sum_n h_n. \tag{6.2.0.1}$$

Here, $\vec{S}_n$ is the spin operator on site n, and J_n, J_z are interaction constants. Note, that in this chapter n denotes the site of the chain to make an easy connection to references [117, 118]. We consider dimerized models where J^z does not depend on the site n and $J_n = (1 + (-1)^n \delta)$, δ being the dimerization coefficient. For $\delta > 0$, the "strong bond" with $J_n = 1 + \delta$ is chosen to be at the center, where the spin flip of the initial state is located.
We have chosen our energy unit such that $J_n = 1$ for the homogeneous case $\delta = 0$. We also set $\hbar = 1$, measuring time in units of $\hbar/J$. The quantum phase diagram of this model at zero temperature is well known (see [120, 121]) and sketched in Fig. 6.1. For the homogeneous case, $\delta = 0$, the ground state has ferromagnetic / anti-ferromagnetic order with a gap in the excitation spectrum for $J_z < -1$ and $J_z > 1$, respectively. The gap closes if $|J_z|$ approaches 1 from above, and the model becomes critical for $-1 < J_z < 1$, i.e. gapless in the thermodynamic limit, with correlation functions showing a power-law decay. The model at the point $J_z = \delta = 0$ is known as the XX-model. It has the special property that the spin-current operator $J = \sum_n j_n$ is conserved, i.e. $[J, H] = 0$. Here $j_n = J_n \mathrm{Im}\,(S_n^+ S_{n+1}^-)$ is the current operator on the bond between site n and $n+1$. For finite dimerization, $\delta \neq 0$, the spectrum is again gapped for all values of J_z.
It is often useful to map the Heisenberg model onto a model of spinless fermions:

$$\begin{aligned} H &= \sum_n J_n \left[\frac{1}{2}(c_n^\dagger c_{n+1} + c_{n+1}^\dagger c_n) \right. \\ &\quad \left. + J_z \left(c_n^\dagger c_n - \frac{1}{2} \right) \left(c_{n+1}^\dagger c_{n+1} - \frac{1}{2} \right) \right]. \end{aligned} \tag{6.2.0.2}$$

Here $c_n^\dagger$ and c_n are the fermionic creation and annihilation operators. In this picture, the first two terms describe nearest-neighbour hopping of fermions, whereas the third term (the one proportional to J_z) describes a density-density interaction between nearest neighbours. In particular, the case $J_z = 0$ describes free fermions on a lattice, and can be solved exactly [122].

The time evolution under the influence of a time-independent Hamiltonian H as in Eq. (6.2.0.1) is given by:

$$\big|\psi(t)\big\rangle = U(t)\big|\mathrm{ini}\big\rangle \quad \text{with } U(t) = \exp(-iHt). \tag{6.2.0.3}$$

In most of the phases shown in Fig. 6.1, the state $\big|\mathrm{ini}\big\rangle = \big|\uparrow \ldots \uparrow\downarrow \ldots \downarrow\big\rangle$ contains many high-energy excitations and is thus far from equilibrium. In the following, we briefly discuss these phases separately.
– Deep in the ferromagnetic phase, $J_z < -1$, $\big|\mathrm{ini}\big\rangle$ corresponds to a state with one domain wall between the two degenerate ground states. For $J_z \to -\infty$ it is identical to the ground state in the total magnetization sector $S_z^{\mathrm{tot}} = 0$ and with boundary conditions given by $\big|\uparrow\big\rangle$ and $\big|\downarrow\big\rangle$ at the left and right end of the chain respectively. It is therefore stationary. For finite J_z, it is no longer identical to the ground state, but still close to it [123].
– In the anti-ferromagnetic phase, $J_z > 1$, the state $\big|\mathrm{ini}\big\rangle$ is highly excited. One could view it as a state with almost the maximum number of domain walls of staggered magnetization.
In this context, it is interesting to note that the sign of J_z does not matter for the time evolution of physical quantities, as long as the initial state is described by a purely real wave function (which is the case for our choice of $\big|\mathrm{ini}\big\rangle$), since the sign change in J_z can be compensated by a gauge transformation that inverts the sign of the terms S^xS^x, S^yS^y in Eq. (6.2.0.1) and together with complex conjugation of Eq. (6.2.0.3). In particular, the time evolution of the low-energy one domain-well state in the ferromagnetic is the same as the evolution of the high-energy many domain-walls state in the anti-ferromagnetic. We therefore restrict ourselves to the case $J_z > 0$, since both cases can be dealt with by the adaptive t-DMRG equally well.
– In the critical phase $\delta = 0$ and $|J_z| < 1$, the ground state is a state with power-law correlations in the xy-plane of the spins. Here, the state $\big|\mathrm{ini}\big\rangle$ is not close to any particular eigenstate of the system, but contains many excited states throughout the energy spectrum, depending on the value of J_z: The energy expectation value of $\big|\mathrm{ini}\big\rangle$ is low as $J_z \to -1$ and high as $J_z \to 1$. For $J_z = 0$, the time evolution of the system can be solved exactly. For example, the time evolution of the magnetization profile for the initial state $\big|\mathrm{ini}\big\rangle$ reads [118]:

$$S_z(n,t) = \big\langle\psi(t)\big|S_n^z\big|\psi(t)\big\rangle = -1/2 \sum_{j=1-n}^{n-1} \mathtt{J}_j^2(t), \tag{6.2.0.4}$$

where $\mathtt{J}_j$ is the Bessel function of the first kind. $n = \ldots, -3, -2, -1, 0, 1, 2, 3, \ldots$ labels chain sites with the convention that the first site in the right half of the chain has label $n = 1$.
– In the dimerized phase, $\delta \neq 0$, the mentioned characteristics remain unchanged. However, here the delocalization becomes confined to pairs of neighbouring sites in the limit $\delta \to 1$. For $\delta = 1$ there exists only a coupling on every second bond.
We finally note that the total energy and magnetization of the system are

conserved at all times, such that even for long times the state cannot relax to the ground state.
The initial state $|\text{ini}\rangle$ is prepared as the ground state of a suitably chosen Hamiltonian H_{ini} (which does in principle not have to have any physical significance). Such a choice is $H_{\text{ini}} = \sum_n B_n S_n^z$, with $B_n < 0$ for n on the left, $B_n > 0$ for n on the right half of the chain. In this case, a physical picture for H_{ini} does exist; it corresponds to switching on a magnetic field that aligns the spins and that is strong enough for all interactions in Eq. (6.2.0.1) to be negligible.

6.3. Accuracy of the adaptive t-DMRG

As so far no quantitative analysis of the accuracy of the adaptive t-DMRG has been given in the literature, we provide a detailed error analysis for the time evolution of the initial state $|\text{ini}\rangle$ in a spin-1/2 quantum XX-chain, i.e. $J_z = \delta = 0$. This system is an excellent benchmark for the adaptive t-DMRG due to its exact solution [118] that can be compared to the DMRG results. The exact solution reveals a nontrivial behaviour with a complicated substructure in the magnetization profile. From a DMRG point of view this Hamiltonian $J_z = 0$ is not too specific in the sense that the experience from static DMRG suggests a relatively weak truncation error dependence on J_z. We therefore expect that the main findings of the error analysis hold more generally.

6.3.1. Error analysis for the XX-model

In this section, we analyze the errors from the adaptive t-DMRG in the time evolution of the XX-model by comparing it to the exact solution [118], with the ultimate goal of finding optimal DMRG control parameters to minimize the errors. Recall that the errors introduced in the adaptive t-DMRG have two main origins: the truncation of the Hilbert space and the Suzuki-Trotter decomposition (see section 2.9). In the following we mainly use two measures for the error:
(i) As a measure for the overall error we consider the *magnetization deviation* $\text{err}(t)$ the maximum deviation of the local magnetization found by DMRG from the exact result,

$$\text{err}(t) = \max_n |\langle S^z_{n,\text{DMRG}}(t)\rangle - \langle S^z_{n,\text{exact}}(t)\rangle|. \tag{6.3.1.1}$$

In the present study, the maximum was typically found close to the center of the chain.
(ii) As a measure for the truncation error which excludes the Suzuki-Trotter error we use the *forth-back deviation* $FB(t)$, which we define as the deviation between the initial state $|\text{ini}\rangle$ and the state $|fb(t)\rangle = U(-t)U(t)|\text{ini}\rangle$, i.e. the state obtained by evolving $|\text{ini}\rangle$ to some time t and then back to $t = 0$ again. If we Suzuki-Trotter-decompose the time evolution operator $U(-t)$ into odd and even bonds in the reverse order of the decomposition of $U(t)$, the identity $U(-t) = U(t)^{-1}$ holds without any Suzuki-Trotter error, and the forth-back deviation has the appealing property to capture the truncation error only. In

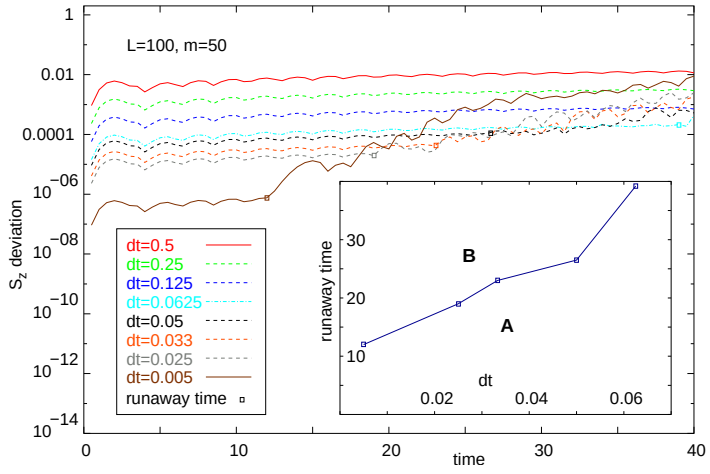

Figure 6.2.: Magnetization deviation as a function of time for different Suzuki-Trotter time steps dt and for $m = 50$ DMRG states. At small times (region A in the inset), the deviation is dominated by the linearly growing Suzuki-Trotter error for small times. At later times (region B in the inset), much faster, non-linear growth of the deviation sets in at some well-defined runaway-time t_R. As shown in the inset, t_R increases with increasing dt.

contrast to the magnetization deviation, the forth-back error does not rely on the existence of an exact solution.
As our DMRG setup does not allow easy access to the fidelity $|\langle \mathrm{ini}|fb(t)\rangle|$, we define the forth-back deviation to be the L_2 measure for the difference of the magnetization profiles of $|\mathrm{ini}\rangle$ and $|fb(t)\rangle$,

$$FB(t) = \left(\sum_n \left(\langle \mathrm{ini}|S_n^z|\mathrm{ini}\rangle - \langle fb(t)|S_n^z|fb(t)\rangle \right)^2 \right)^{1/2}. \tag{6.3.1.2}$$

In order to influence Suzuki-Trotter and truncation errors, two DMRG control parameters are available, the number of DMRG states m and the Suzuki-Trotter time step dt. We start studying the effect of different dt. The *magnetization deviation* for different dt is shown in Fig. 6.2. Two main observations can be made. At small times (regime A), the magnetization deviation decreases with dt and is linear in t as expected from the Suzuki-Trotter error. Indeed, as shown in the upper part of Fig. 6.3, the magnetization deviation depends quadratically on dt for fixed t as expected for the used second order Suzuki-Trotter decomposition. The Suzuki-Trotter error dominates over the truncation error. At large times (regime B in Fig. 6.2), the magnetization deviation is no longer linear in t, but grows much more rapidly. It also does no longer show simple monotonic behaviour in dt: The magnetization deviation in this regime is no longer dominated by the Suzuki-Trotter error, but by the accumulated truncation error.
The two regimes A and B are very clearly separated by some *runaway time* t_R, with regime A for $t < t_R$ and regime B for $t > t_R$ (a precise procedure

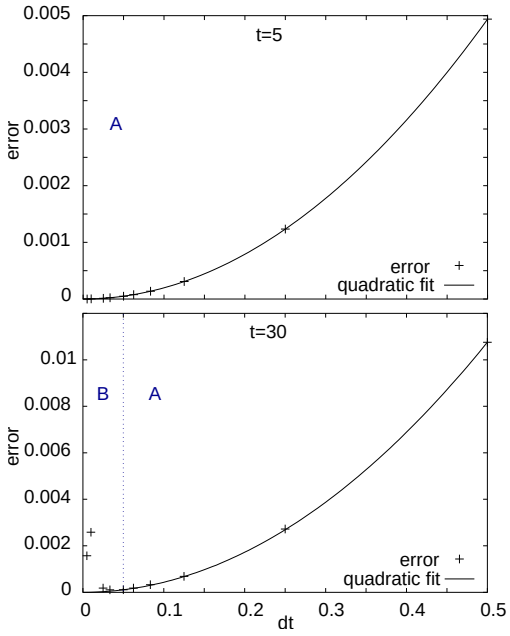

Figure 6.3.: Magnetization deviation as a function of Suzuki-Trotter time step dt (system size $L = 100$, $m = 50$ DMRG states) at times $t = 5$ (upper figure) and $t = 30$ (lower figure). For $t = 5$, the magnetization deviation is quadratic in dt as expected from the Suzuki-Trotter error. For $t = 30$, at small dt the magnetization deviation is no longer quadratic in dt and larger than the Suzuki-Trotter error would suggests. This is a signal of the contribution of the accumulated truncation error.

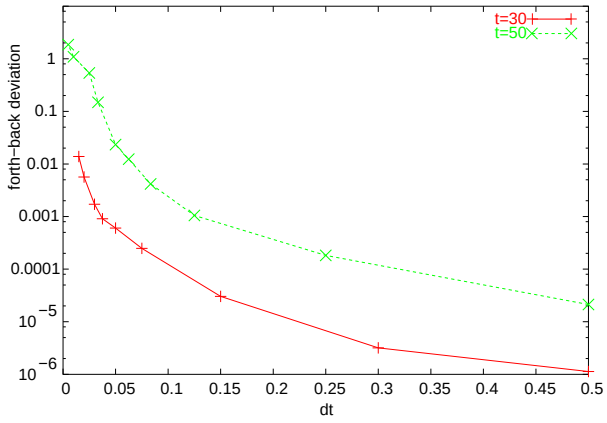

Figure 6.4.: The forth-back error $FB(t)$ for $t = 30$ and $t = 50$, as function of $\mathrm{d}t$. Here, $L = 100$, $m = 50$.

for its determination will be outlined below). The runaway time t_R increases when $\mathrm{d}t$ is increased: Because the total number of Suzuki-Trotter time steps $t/\mathrm{d}t$ is decreased, the accumulated truncation error decreases, and the Suzuki-Trotter error increases, hence the time t_R where the accumulated truncation error becomes of the order of the Suzuki-Trotter error is even longer. This $\mathrm{d}t$-dependence of t_R is also seen in the lower part of Fig. 6.3, where the $\mathrm{d}t$ dependence of the magnetization deviation is plotted at some larger time ($t = 30$) than in the upper part. $t = 30$ is larger than the runaway time (i.e. in regime B) for $\mathrm{d}t \leq 0.05$, in regime A otherwise. We see indeed for $\mathrm{d}t > 0.05$ (region A) the familiar quadratic Suzuki-Trotter error dependence. For small $\mathrm{d}t \leq 0.05$ (region B), the deviation is dominated by the accumulated truncation error that increases as $\mathrm{d}t$ decreases. This is reflected in the growth of the magnetization deviation as $\mathrm{d}t$ is *de*creased.

The very rapid growth of the truncation error with the number of Suzuki-Trotter steps can also be seen from the forth-back deviation that is not susceptible to the Suzuki-Trotter error. In Fig. 6.4, we show the forth-back deviation $FB(t)$ for $t = 30$ and $t = 50$ as a function of the Suzuki-Trotter time step $\mathrm{d}t$. $FB(t)$ increases as a consequence of the higher accumulation of the truncation error with decreasing Suzuki-Trotter step size $\mathrm{d}t$ and hence an increasing number of steps $t/\mathrm{d}t$.

The influence of the dependence of the magnetization deviation $\mathrm{err}(t)$ on the second control parameter, the number m of DMRG states, is shown in Fig. 6.5. Here $\mathrm{err}(t)$ is plotted for a fixed Suzuki-Trotter time step $\mathrm{d}t = 0.05$ and different values of m. In agreement with our previous observations, some m-dependent "runaway time" t_R, separates two regimes: for $t < t_R$ (regime A), the deviation grows essentially linearly in time and is independent of m, for $t > t_R$ (regime B), it suddenly starts to grow very rapidly. The onset of a significant m-dependence has indeed been our operational definition of t_R in Fig. 6.2 and Fig. 6.5. In the inset of Fig. 6.5, t_R is seen to increase roughly linearly with growing m. As $m \to \infty$ corresponds to the complete absence of

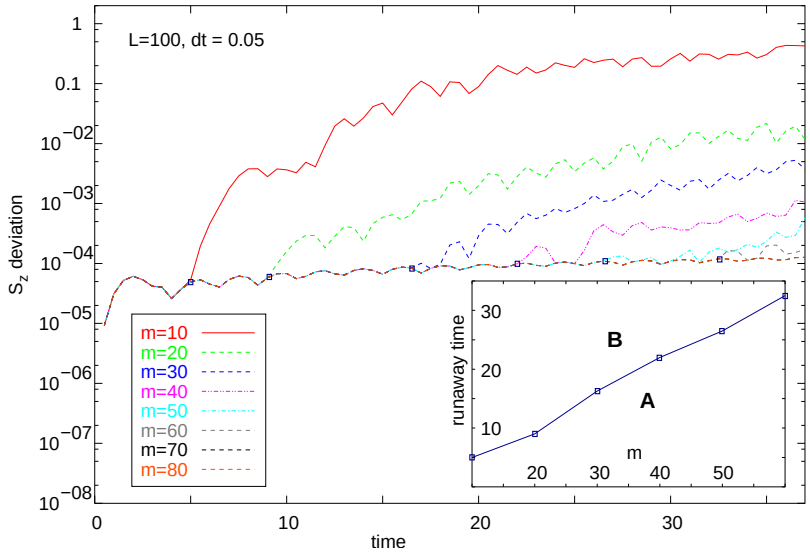

Figure 6.5.: Magnetization deviation $\Delta M(t)$ as a function of time for different numbers m of DMRG states. The Suzuki-Trotter time interval is fixed at $\mathrm{d}t = 0.05$. Again, two regimes can be distinguished: For early times, for which the Suzuki-Trotter error dominates, the error is slowly growing (essentially linearly) and independent of m (regime A); for later times, the error is entirely determined by the truncation error, which is m-dependent and growing fast (almost exponential up to some saturation; regime B). The transition between the two regimes occurs at a well-defined "runaway time" t_R (small squares). The inset shows a monotonic, roughly linear dependence of t_R on m.

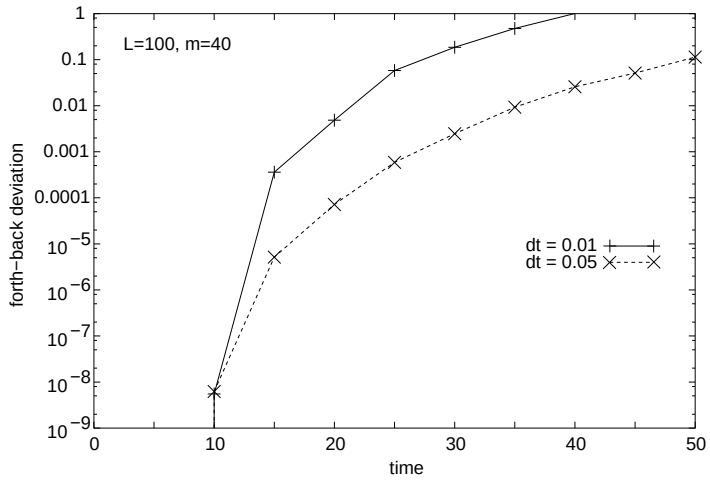

Figure 6.6.: The forth-back error $FB(t)$ for $L = 100$, $m = 40$, $\mathrm{d}t = 0.01$ and $\mathrm{d}t = 0.05$, as function of t.

the truncation error, the m-independent bottom curve of Fig. 6.5 is a measure for the deviation due to the Suzuki-Trotter error alone and the runaway time can be read off very precisely as the moment in time when the truncation error starts to dominate.

That the crossover from a dominating Suzuki-Trotter error at short times and a dominating truncation error at long times is so sharp may seem surprising at first, but can be explained by observing that the Suzuki-Trotter error grows only linearly in time, but the accumulated truncation error grows much faster in time. The latter fact is shown in Fig. 6.6, where the forth-back deviation $FB(t)$ is plotted as a function of t for some fixed m. The effects of the truncation error are below machine precision for $t < 10$ and then grow very rapidly in time up to some saturation.

In Fig. 6.7 $FB(t)$ is plotted as a function of m, at $t = 30$ and $t = 50$. An approximately exponential increase of the accuracy of the method with growing m is observed for a fixed time. Our numerical results that indicate a roughly linear time-dependence of t_R on m (inset of Fig. 6.5) are the consequence of some balancing of very fast growth of precision with m and decay of precision with t.

Before concluding this section, let us briefly consider a number of other possible effects that might affect t_R. One might alternatively conceive that the well-defined runaway-time t_R results from a sudden failure (of stochastic or of fundamental nature) of the truncation algorithm to capture one important basis state. It can be refuted on the basis of Fig. 6.4, Fig. 6.6 and Fig. 6.7: Such an error should manifest itself as a pronounced step in $FB(t)$, depending on the time evolution having gone past t_R or not. However, such a step is not observed.

t_R might also be thought to reflect a fundamental DMRG limit, namely a growth of the entanglement within the time-evolved state which the limited number of DMRG states m is not able to capture adequately at $t > t_R$. This scenario can

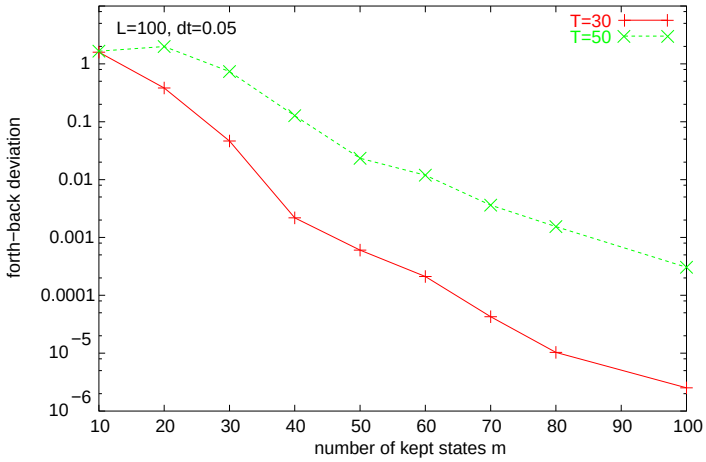

Figure 6.7.: The forth-back error $FB(t)$ for $t = 50$ and $t = 30$, as function of m. Here, $L = 100$, $\mathrm{d}t = 0.05$.

be excluded by observing the strong dependence of t_R on the number of time steps, which this scenario cannot explain. Indeed, a study of the entanglement entropy between the left and the right half of the chain

$$S_e(t) = \mathrm{Tr}\hat{\rho}\log_2\hat{\rho}, \tag{6.3.1.3}$$

$\hat{\rho}$ being the reduced density matrix of the left (or equivalently the right) half of the chain, confirms this view: As shown in Fig. 6.8, $S_e(t)$ is only mildly growing with time after its first increase and is well below the maximum entanglement entropy $S_{\max} \sim \log_2 m$ that DMRG can reproduce.
Therefore, we conclude that the error at short times is dominated by the Suzuki-Trotter error, which is independent of m and approximately growing linearly with time. At some runaway time, we observe a sharp crossover to a regime in which the m-dependent and very rapidly growing truncation error is dominating. This crossover is sharp due to drastically different growth of the two types of errors. The runaway time thus indicates an imminent breakdown of the method and is a good, albeit very conservative measure of available simulation times. We expect the above error analysis for the adaptive t-DMRG using the XX-model to be generic and also applicable for other models. The truncation error will remain also in approaches that dispose of the Suzuki-Trotter error; maximally reachable simulation times should therefore be roughly the same or somewhat shorter if other approximations enhance the truncation error.

6.3.2. Optimal choice of DMRG parameters

How can the overall error – which we found to be a delicate balance between the Suzuki-Trotter and the accumulated truncation error – be minimized and the important runaway time be found in practice? From the above scenario it should be expected that the truncated density matrix weight at each step does not behave differently before or after the runaway time and hence is no

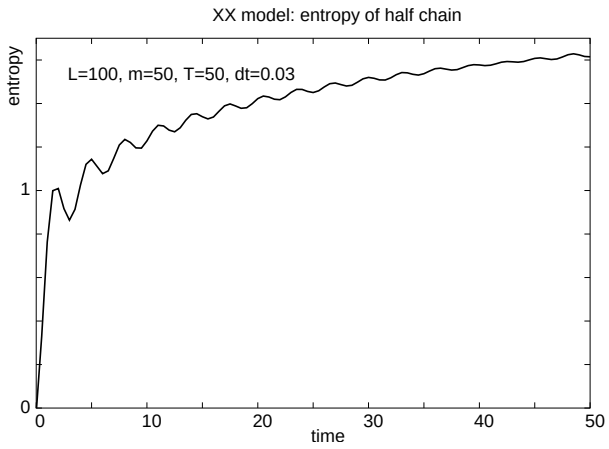

Figure 6.8.: Entanglement entropy S_e from Eq. 6.3.1.3 between the left and the right half of the chain as function of time.

immediately useful indicator to identify the runaway time. This can in fact be seen from Fig. 6.9, where the truncated weight is shown for the same parameters as in Fig. 6.2. Also, it is not obvious to extract a precise relationship between the truncation errors at each DMRG truncation and the accumulated errors. Instead, a precise convergence analysis in m or dt seems to be more telling and is therefore recommended.
In practice, it is desirable to choose the number of kept states m as large as possible within the constraints regarding the available computer resources. This choice having been made, the runaway time t_R is determined for different Suzuki-Trotter time steps dt by comparing different values of m (analog to Fig. 6.5, but using only the knowledge about curves for different m). Only two slightly different values of m are sufficient for that purpose. Now the Suzuki-Trotter time step dt is chosen such that the desired time t is just below t_R. This way, the optimal balance between the Suzuki-Trotter error and the truncation error is found, which corresponds in the lower part of Fig. 6.3 to the minimum of err(t) on the border between regime A and B: The total error would increase at larger dt due to the Suzuki-Trotter error, and at smaller dt due to the truncation error.
Thus, it is a good practice to choose for small times rather small values of dt in order to minimize the Suzuki-Trotter error; for large times, it makes sense to choose a somewhat coarser time interval, in order to push the runaway time to as large values as possible.
In terms of numbers of time steps, we conclude from Fig. 6.2 that for the present model and our parameters (lengths $L = 100-200$), the adaptive time-dependent DMRG seems to be able to perform about 1000-5000 time steps reliably even for $m = 50$, depending on the desired level of accuracy, corresponding to $O(100/J)$ in "real" time. We note that this is a very small value of m by DMRG standards, and that using an optimized code, one should be able to increase m by an order of magnitude, and hence access much longer times (by an order of magnitude) if so desired.

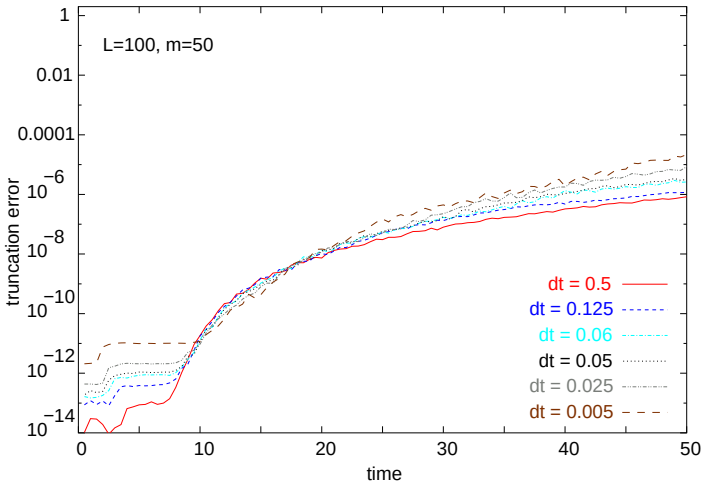

Figure 6.9.: The lost weight in the density matrix truncation, summed over time intervals $\Delta t = 0.1$, is shown for the same parameters as in 6.2. A comparison with Fig. 6.2 reveals, however, that both values are not useful criteria for the DMRG truncation error and are in particular not suited to reveal the runaway time t_R.

6.4. Long-time properties of the time evolution

The time evolution of the initial state $|\text{ini}\rangle$ on the XX-chain at temperature $T = 0$ was examined in the long-time limit using the exact solution [118, 124]. The question we would like to address in the following is how the long-time properties of the system changes if the spin interaction in z-direction is chosen to be finite, i.e. $J_z \neq 0$. To do this we briefly summarize the findings for the XX-chain, before we discuss our results for finite J_z.

For the XX-chain it was found that the magnetization $S_z(n,t)$ given in Eq. (6.2.0.4) can be described for long times in terms of a simple scaling function, $S_z(n,t) \approx \Phi\left([n-n_c]/t\right)$, where n_c is the position of the chain center. The scaling function is the solution of the partial differential equation $\partial_t S_z + \partial_x j(S_z) = 0$ with the magnetization current $j(S_z) = 1/\pi \cos|\pi S_z|$ which has been shown to describe the macroscopic time evolution of the magnetization profile [118]. The characteristics, i.e. the lines of constant magnetization S_z, have a slope $v = \sin|\pi S_z|$. The magnetization profile $\Phi\left([n-n_c]/t\right)$ has a well-defined front at $(n-n_c)/t = \pm 1$, i.e. is moving outwards ballistically with velocity $v = 1$. On top of this overall scaling form an additional step-like substructure arises, which was analysed in detail in Ref. [124]. It was found that while the step width broadens as $t^{1/3}$, the step height decreases as $t^{-1/3}$, such that the integrated transported magnetization within each step remains constant at 1. It was suggested that each of these steps corresponds to a localized flipped spin flowing outwards.

The XX-model, however, has several very special properties: It corresponds to a free-fermion model and is therefore exactly solvable; it is critical; and its total current operator $J = \sum_n j_n$ commutes with the Hamiltonian, $[J, H] = 0$.

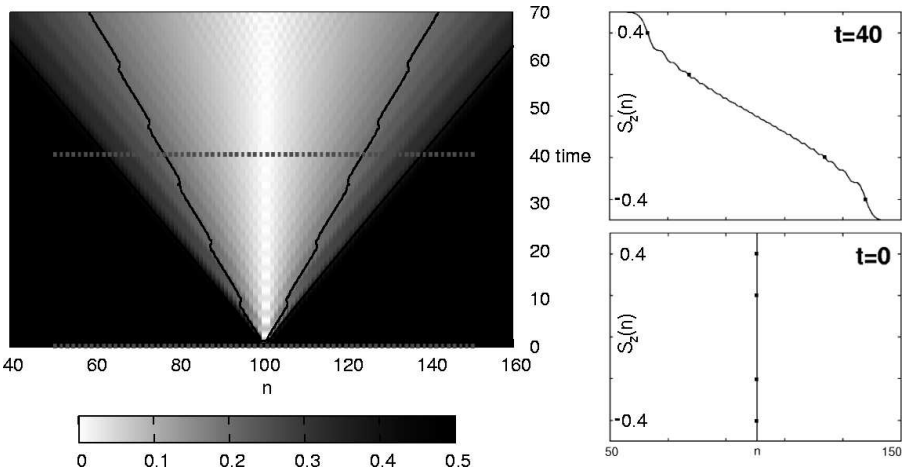

Figure 6.10.: Left: Time evolution of the absolute value of the local magnetization $|\langle S_n^z(t)\rangle|$ for the XX-model as a density plot, where the local magnetization itself is exactly antisymmetric with regard to the chain center. The lines of constant-magnetization $\langle S_n^z\rangle = \pm 0.2, \pm 0.4$ are shown as solid lines ($S_z = \pm 0.4$ can hardly be seen). As an illustration, local magnetizations $\langle S_n^z(t)\rangle$ for the time slices $t = 0$ and $t = 40$ are shown explicitly. The symbols mark the values $\langle S_n^z\rangle = \pm 0.2, \pm 0.4$. A step-like substructure can be seen for $t = 40$ in perfect quantitative agreement with the exact solution. Error bars are below visibility.

One may ask whether the above findings are due to any of the particularities of the XX-model or more generic.
The adaptive t-DMRG allows us to study the long-time evolution of $\big|\mathrm{ini}\big\rangle$ in different coupling regimes of Hamiltonian (6.2.0.1). We chose two extensions of the XX-model, namely a S^zS^z- interaction, and dimerization.

S^zS^z-interaction In Fig. 6.10 and Fig. 6.11, we visualize the time evolution of the local magnetization obtained from the adaptive t-DMRG in density plots, with site index n on the x-axis, time t on the y-axis. Here, the absolute value of the magnetization is shown as a grey-scale and in lines of constant magnetization at $|\big\langle S_z\big\rangle| = 0.2,\ 0.4$. In Fig. 6.10, the relation between the density plots and the actual magnetization profile for the XX-model is shown at two times, $t = 0$ and $t = 40$. The exact solution is perfectly reproduced, including the detailed substructure of the magnetization profile.
In Fig. 6.11, density plots for various values of J_z between 0 and 1.1 are shown. For small J_z ($J_z < 1$), we observe ballistic transport of the magnetization. This regime is characterized by a constant transport velocity of the magnetization, hence the lines of constant magnetization shown in Fig. 6.11 are approximately straight for $J_z < 1$. The magnetization front propagation slows down as J_z increases, and almost comes to a halt when $J_z > 1$. Although the sharpness of this crossover at $J_z = 1$ is surprising, its general nature can be understood

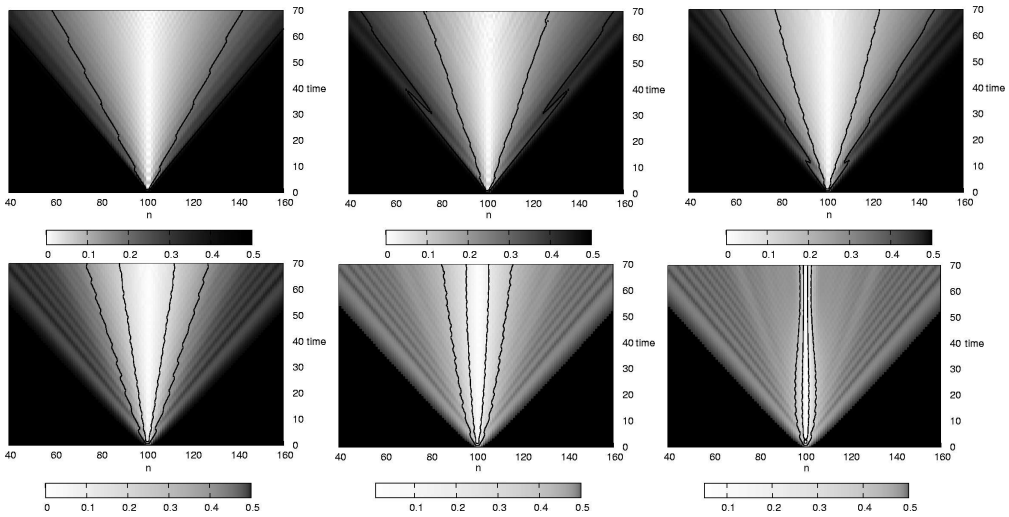

Figure 6.11.: Density plots of the magnetization $|\langle S^z_n(t)\rangle|$ as in Fig. 6.10, the values of J_z being (from left to right, top to bottom) 0, 0.3, 0.6, 0.9, 1.0, 1.1, and $\delta = 0$. For better visibility of the profile, the grey-scale mapping of $|\langle S^z_n(t)\rangle|$ was chosen differently in each plot as indicated by the legends. Solid lines: lines of constant magnetization $\langle S^z_n\rangle = \pm 0.2, \pm 0.4$; these allow for a direct comparison of the magnetization transport between different J_z. The ray-like structure indicates the "carriers".

from the limits $J_z \ll 1$ and $|J_z| \to \infty$: For small $J_z \ll 1$ the S^xS^x- and S^yS^y-interactions dominate. Being spin flip terms, they smear out the initially hard step profile in the z magnetization. For large J_z, on the other hand, the S^zS^z-interaction dominates. This term does not delocalize the step profile, and in the limit $|J_z| \to \infty$, the initial state is even a stationary eigenstate of the Hamiltonian.
Besides the structure of the overall front, we also observe for $J_z \neq 0$ remnants of the steplike substructure from the XX-model, individual pockets which transport magnetization at velocity 1, which we call "carriers". As J_z is increased, these carriers keep the velocity $v \approx 1$, but are increasingly damped and thus less and less effective in transporting magnetization.
In order to put the above observations on a more quantitative footing, we plot in Fig. 6.12 the integrated flow of magnetization through the center,

$$\Delta M(t) = \int_0^t \big\langle j_{L/2}(t')\big\rangle \mathrm{d}t' = \sum_{n>L/2}^{L} \big(\big\langle S^z_n(t)\big\rangle + 1/2\big)\,. \tag{6.4.0.1}$$

This quantity has the advantage that unlike the lines of constant magnetization in Fig. 6.10 and Fig. 6.11, it shows the overall spin transport without being too much biased by single "carriers". We observe in Fig. 6.12 a roughly linear behaviour of $\Delta M(t)$ for $|J_z| < 1$, which suggests ballistic magnetization transport at least on the time scales accessible to us. As J_z increases, magnetization transport slows down until around $J_z = 1$ the behaviour changes drastically:

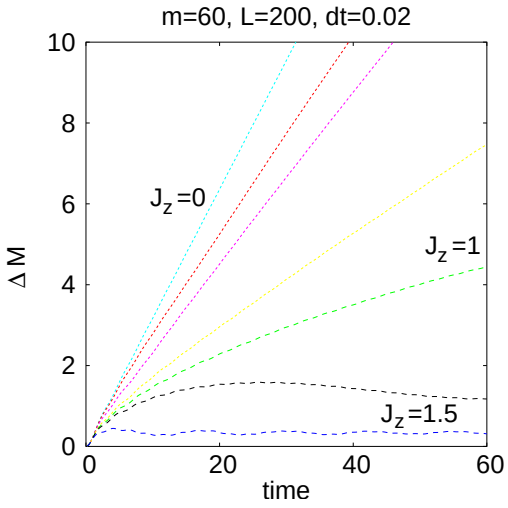

Figure 6.12.: The change in the magnetization $\Delta M(t)$ is shown. The curves are plotted in the order $J_z = 0;\ 0.3;\ 0.6;\ 0.9;\ 1.0;\ 1.1;\ 1.5$, where $J_z = 0$ is the steepest. The curves $J_z = 0;\ 0.3;\ 0.6;\ 0.9$ show the same linear behaviour for the observed times, i.e. up to $t = 60$.

For $J_z > 1$, $\Delta M(t)$ seems to saturate at a finite value, around which it oscillates. Thus on the time scales accessible to us, we find a sharp crossover at $J_z = 1$ from ballistic transport to an almost constant magnetization.

This crossover is even more clearly visible in Fig. 6.13, where we plot the exponent a of the magnetization, $\Delta M(t) \propto t^a$, for values J_z between 0 and 1.5. Here, the exponent a is close to 1 for $J_z < 1$, confirming the roughly linear transport, and quickly drops to zero in the regime of constant magnetization for $J_z > 1$. Fig. 6.14 illustrates how the exponent a was obtained, for the special case $J_z = 1$. Here the exponent $a = 0.6 \pm 0.1$ indicates that the magnetization transport is clearly not ballistic anymore. In fact, we find from a scaling plot Fig. 6.15 that for long times the magnetization collapses best for a scaling function of the form $S_z(n,t) \sim \phi(n/t^{0.6})$ with an uncertainty in the exponent of approximately 0.1, indicating superdiffusive or diffusive transport in the time range under consideration.

The proposed crossover from ballistic to almost no transport is also visible in the expectation value of the current j_n between site n and site $n+1$, i.e. $j_n = J_n \mathrm{Im}\left(\left\langle S_n^+ S_{n+1}^- \right\rangle\right)$. For $J_z = \delta = 0$, it is known [118] that the current at the middle of the chain approaches a finite value as $t \to \infty$. This is only possible for ballistic transport. In the case of (sub- / super-) diffusive transport or constant / oscillatory magnetization, on the other hand, the central current must fall off to zero as the magnetization gradient flattens or must even become negative to allow for the oscillations.

This expected behaviour is seen in Fig. 6.16, where we plot the current at the center of the chain as a function of time for various values of J_z between 0 and 1.1. We averaged the current over the 5 middle sites in order to filter out local current oscillations. We observe that for relatively long times, the current

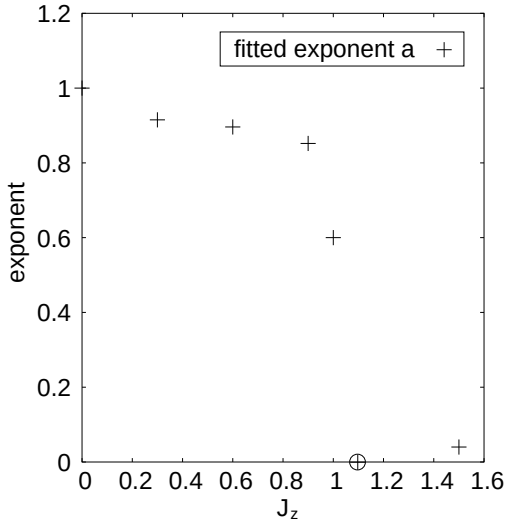

Figure 6.13.: Best fit for the exponent a in $\Delta M(t) \propto t^a$, for the data shown in Fig. 6.12 using times between $t = 20$ and $t = 60$. We estimate the uncertainty in a to be of the order of 0.1 due to the limited time available (cf. Fig. 6.14). It was not possible to fit the slow oscillations for $J_z = 1.1$. To the eye, however, the curve in Fig. 6.12 suggests slow oscillations around a constant value, hence we included in the data point $a = 0$ for $J_z = 1.1$ by hand (encircled).

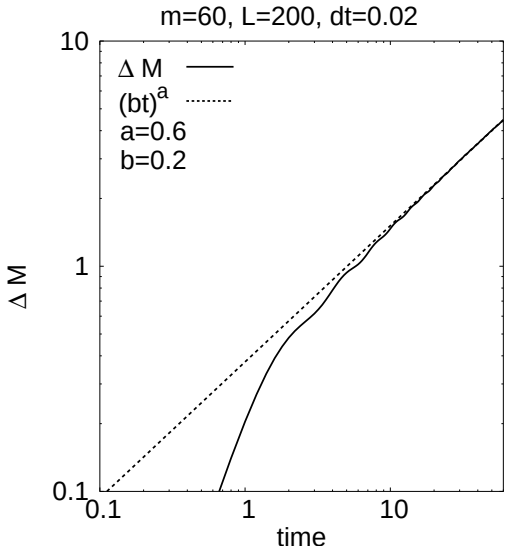

Figure 6.14.: $J_z = 1$: The change of the magnetization in a double logarithmic plot with an algebraic fit.

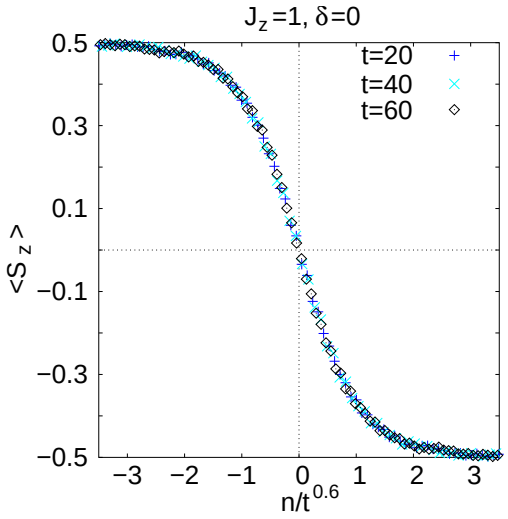

Figure 6.15.: $J_z = 1$: Collapse of magnetization for different times t using the superdiffusive scaling form $(x/t^{0.6})$.

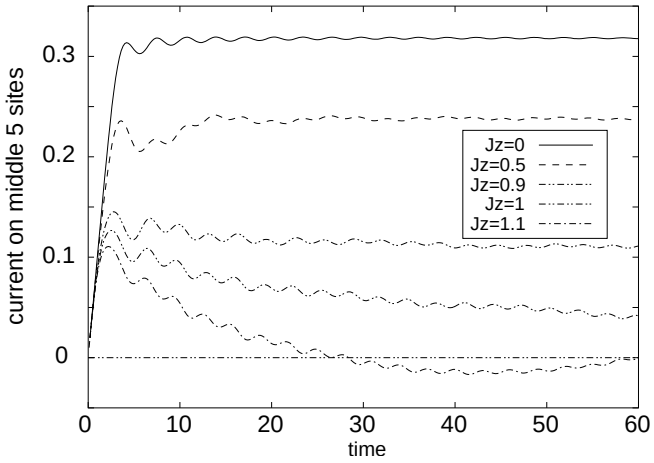

Figure 6.16.: Current, averaged over the 5 sites around the center, for various values of J_z between 0 and 1.1.

approaches a constant value for $|J_z| < 1$, whereas the current falls off rapidly and then seems to exhibit damped oscillations around zero for $|J_z| > 1$. This strengthens our previous conclusion of a crossover from ballistic transport to a more or less constant magnetization at $|J_z| = 1$.

Remarkably, this crossover for the behaviour of a high-energy quantum state $\big|\mathrm{ini}\big\rangle$ is found at the value $J_z = 1$ of the quantum phase transition from the critical phase to the Néel anti-ferromagnetic state (see Fig. 6.1), a priori a low-energy event. To understand the subtle connection between the time evolution of $\big|\mathrm{ini}\big\rangle$ and the phase transition, we exploit the fact that the time evolution does not depend on the sign of J_z, as discussed in Sec. 6.2. Therefore the time evolution of the high-energy state $\big|\mathrm{ini}\big\rangle$ for $J_z > 1$ is identical to the time evolution for $J_z' = -J_z < -1$, where $\big|\mathrm{ini}\big\rangle$ is a low-energy state. At the quantum phase transition from the ferromagnetic state to the critical phase at $J_z' = -1$ the ground state, a kink state for $J_z' < -1$ (if we impose the boundary condition spin up on the left boundary and spin down on the right boundary) [123], changes drastically to a state with no kink and power-law correlations for $J_z' > -1$. Therefore, our initial state is very close to an eigenstate – the ground state – for $J_z' < -1$, but not for $J_z' > -1$. Thus, the harsh change in the time evolution of the high-energy state $\big|\mathrm{ini}\big\rangle$ at $J_z = 1$ can be explained by the severe change in the ground state properties at $J_z' = -1$, and the crossover is linked to the quantum phase transition at the value $J_z' = -1$ in the phase diagram.

Dimerization We now study the influence of a nonzero dimerization δ in the Hamiltonian (6.2.0.1.) We restrict our analysis to the case $J_z = 0$. The dimerized models can still be described in terms of the free-fermion picture and are exactly solvable (for static properties see [121]). The current, however, is not conserved for nonzero dimerization and the energy spectrum has a gap. This example will shed light on the question whether the long-time limit depends on current conservation, on the presence of a gap, or on the free-fermion property, or another special properties of the system. As the dimerized case is also exactly solvable, the results could have been obtained also analytically, for example by utilizing the results for the Fourier transformation of the magnetization $\big\langle S_z(q,t)\big\rangle$ of Ref. [119]. We expect two obvious effects of nonzero dimerization: Firstly, the overall front velocity should slow down, because the magnetization now propagates faster on half of the links, but slower on the other half, the net effect being a reduction of the total velocity. Secondly, we expect oscillations with a period of two lattice sites. This is obvious in the limit $\delta \to 1$, where each strongly coupled pair of sites can be viewed as an almost isolated subsystem, in which the magnetization oscillates back and forth. We expect remnants of this behaviour also at dimerizations $|\delta| < 1$. The data for the magnetization shown in Fig. 6.17 confirms this expectation qualitatively, but does not reveal any other qualitative change of the long-time limit for nonzero dimerization.

For $\delta = 1$, the system is trivially given by isolated pairs of neighbouring sites, therefore the propagation velocity drops to zero.

Fig. 6.18 and Fig. 6.19 reveal explicitly that no qualitative change occurs in the transport behaviour as the dimerization is switched on: the change in mag-

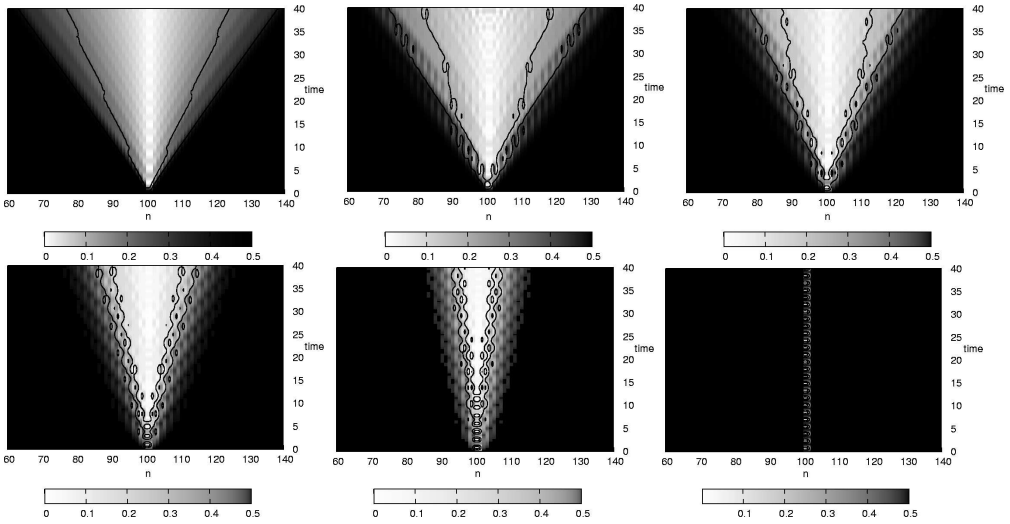

Figure 6.17.: Density plots of the magnetization $\langle S_n^z(t)\rangle$, for dimerization (from left to right, top to bottom) $\delta = 0; 0.2; 0.4; 0.6; 0.8; 1.0$, and $J_z = 0$. The grey-scale mapping is different in each plot as indicated by the legends. Solid lines: lines of constant magnetization $\langle S_n^z\rangle = \pm 0.2, \pm 0.4$.

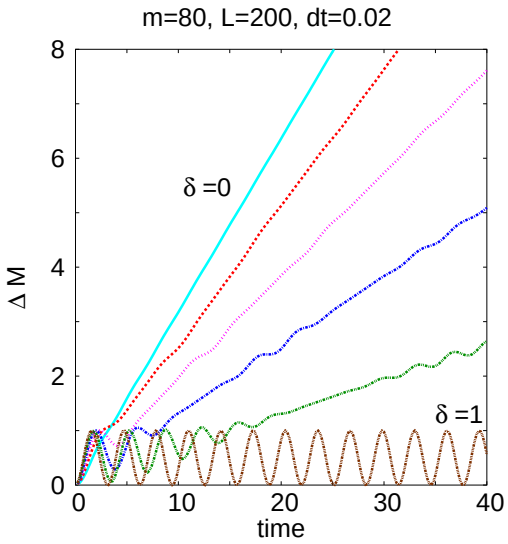

Figure 6.18.: Change in magnetization $\Delta M(t)$ for different dimerizations, from top to bottom: $\delta = 0$, 0.2, 0.4, 0.6, 0.8, 1.0.

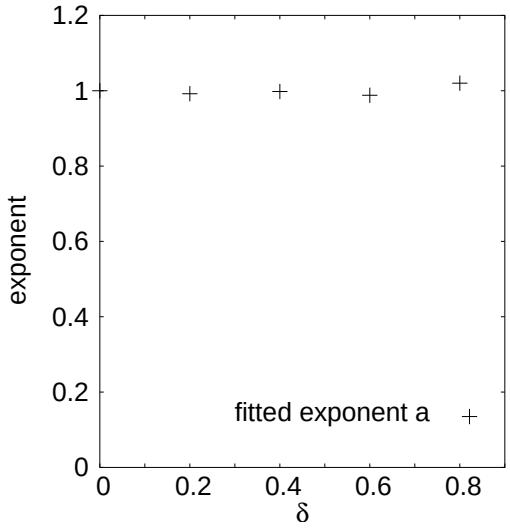

Figure 6.19.: Best fit for the exponent a in $\Delta M(t) \propto t^a$, for the data shown in 6.12 and for times between $t = 20$ and $t = 40$.

netization $\Delta M(t)$ still shows the linear behaviour typical of ballistic transport. For increasing $\delta \to 1$ oscillations on top of this linear behaviour arise. We find that also for nonzero J_z (not shown) switching on finite dimerization does not change the long-time behaviour of the time evolution. In particular, the time evolution here is drastically influenced by the transition at $J_z = 1$ as in the case $\delta = 0$ discussed above.

To summarize, we find the same long-time behaviour using $\left| \uparrow \ldots \uparrow\downarrow \ldots \downarrow \right\rangle$ as initial state in the dimerized system — a system with gapped excitation spectrum and which is exactly solvable — as in the system with small S^zS^z-interaction, $|J_z| < 1$ — a system which is critical — whereas the behaviour changes drastically for larger S^zS^z-interaction, $|J_z| > 1$. Hence we cannot attribute the ballistic transport of the magnetization to the specific properties of the XX-model; neither to be exactly solvable, nor to the continuous spectrum nor to the conserved current in the XX-model. The drastic change at $|J_z| = 1$ stems from the special property of the initial state to resemble the ground state in the ferromagnetic phase and the highest energy state in the anti-ferromagnetic phase.

Finally, let us include a note on the errors in the analysis presented here. A convergence analysis in m as in section 6.3 shows that the errors and the runaway time are roughly the same as for the XX-model. The plot in Fig. 6.11 goes up to time $t = 95$, whereas the runaway time t_R is somewhat earlier, $t_R \approx 60 - 80$, depending on the precise value of J_z. Indeed, a convergence analysis in m reveals that the accuracy in the central region decreases for $t > t_R$. For dimerized models the runaway time t_R is somewhat shorter (between $t_R = 40$ and $t_R = 80$ for $m = 50$, depending on the dimerization). This fact reflects the need of keeping more states in the DMRG algorithm when dealing with inhomogeneous systems as already seen in chapter 3. As always, it is possible to increase

t_R by increasing m.

6.5. Conclusions

We modeled two coupled spin-polarized reservoirs by a spin-1/2 system with the initial state $\left| \uparrow \ldots \uparrow\downarrow \ldots \downarrow \right\rangle$ and have investigated its time evolution under the effect of nearest-neighbour interactions with the adaptive t-DMRG.
For weak S^zS^z-interaction, i.e. $|J_z| < 1$ in Eq. (6.2.0.1), and arbitrary dimerization, $0 \leq \delta < 1$, we find that for long times the transport of the magnetization is ballistic as it was found for the XX-model [118]. For stronger S^zS^z-interaction, i.e. $|J_z| > 1$, even in a homogeneous system without dimerization $\delta = 0$, the long-time evolution is completely different. The magnetization transport is no longer ballistic, but shows oscillatory behaviour around a constant value. Hence our results suggest that the ballistic transport at long times is not an artefact of the XX-model. The drastic change or the long time behaviour at the phase transition $J_z = 1$ can be attributed to the close resemblance of the initial state to the ground state of the ferromagnetic phase ($J_z < -1$).
Our error analysis for the adaptive t-DMRG using the exact solution of the XX-model showed that for small times the error is dominated by the Suzuki-Trotter error whereas for long times the truncation error becomes the most important. We expect this finding to be general and hold for non-exactly solvable models as well, and therefore it should allow to control the accuracy of the results of adaptive t-DMRG in general models. Overall, we find this method to be very precise at relatively long times.

7. Conclusion and outlook

In this thesis we developed a powerful new computational tool, the adaptive t-DMRG. It is based on the existing finite-system DMRG, modified to incorporate the TEBD algorithm. The new method is applicable to simulate the time evolution of one-dimensional strongly correlated quantum systems. The idea of DMRG, to construct a specially chosen reduced space of states to describe the physics one is interested in, has been extended for time-dependent phenomena. Unlike traditional DMRG, where the reduced state space is fixed, the adaptive t-DMRG adapts the state space at each time step to cover the evolution of the system. Even without attempting to reach the computationally most efficient implementation of the new algorithm, the resulting code seems to perform systematically better than non-adaptive time-dependent DMRG codes, in which a fixed reduced space is kept for all time steps. The new algorithm allows for much smaller state spaces, because the state space changes in time and is well chosen to track the actual state of the system at any given time. The new method is also significantly more efficient than other existing embodiments of the TEBD due to well-known DMRG techniques, for instance the way DMRG exploits good quantum numbers. Therefore, it can describe the time evolution of one dimensional quantum systems at very reasonable numerical cost.
We tested the applicability, efficiency, and accuracy of the new adaptive t-DMRG algorithm addressing questions in different physical systems: a bosonic, a fermionic, and a spin system. We used the spin system to perform a detailed error analysis. Overall we saw that this method gives precise results for relatively long times. The results of the applications presented in this work can be summarized as follows:

Ultracold bosons Motivated by recent progress in producing ultracold atoms in optical lattices, we applied the adaptive t-DMRG to analyze experimentally realistic situations. Ultracold bosons in optical lattices can be described by the Bose-Hubbard model. Due to the presence of a trapping potential in the experiments, we first had to investigate the influence of such a trapping potential on the static properties of the system. In these systems a superfluid-like and Mott-insulating-like phase can coexist. We found that in a parabolically confined system the one-particle density-matrix, after a remarkably simple scaling, can be used to characterize the occurring phases. This scaled one-particle density matrix shows for the superfluid-like and Mott-insulating like phases approximately the algebraic and exponential behaviour familiar from the one-particle density-matrix in the respective phases in the homogeneous system. We also investigated the applicability of the hydrodynamical approach to such an inhomogeneous system and found good agreement with the DMRG results in the limit of weak interaction. Moreover, we saw that if the experimental

system consists of one-dimensional tubes with a small variance in the average filling, the half width of the observed interference peak can be used to distinguish the different types of states that occur experimentally. In the meantime the experimental results observed in [79] confirmed our theoretical predictions. Turning to time dependent phenomena, we investigated the motion of density perturbations, which are the lowest lying excitations of the system. By comparison to our numerical results, we showed that in the limit of weak interaction the motion of relatively broad and small perturbations can be described well by the hydrodynamical approach or the linearized Gross-Pitaevskii equation. For intermediate interaction strength, however, the mean-field description breaks down while the result obtained from the corresponding continuum Lieb-Liniger model remains valid for somewhat stronger interactions. For very strong interactions, we found that the sound velocity is well approximated by a mapping onto a spinless fermionic model. The adaptive t-DMRG also allowed us to determine the sound velocity in the crossover region between these two regimes, which could not be done before. In addition, we found a linear dependence of the velocity on the height of the perturbation amplitude. This dependence gives rise to effects such as self steepening and shock wave formation. We have further shown that a density wave may be detected experimentally as an additional peak in the interference pattern.

Ultracold fermions: spin-charge separation One key feature of the physics of one-dimensional quantum systems is the phenomenon of spin-charge separation. At low energy the excitations of charge and spin are predicted to decouple in one dimensional systems and propagate with different velocities. To study this phenomenon we have performed numerical simulations of the time-evolution of charge and spin density perturbations using the 1D Hubbard model. To our knowledge these are the first real-time calculations showing spin-charge separation explicitly in systems of experimentally accessible sizes. We clearly observe the separation of spin and charge as a generic feature of 1D fermions, far beyond the low-energy regime where a Luttinger liquid description applies. Based on these results, we propose an experimental setup which should allow the observation of this phenomenon in cold gases by exploiting the different propagation behaviour of spin and charge density perturbations in the liquid and Mott-insulating state. This proposal avoids the problems arising from the different densities in an experimental array of parallel atomic wires. We performed quantitative calculations of the experimental requirements which seem to be within reach today. The different propagation behaviour can also be used to distinguish experimentally between a Mott- and a band insulator.

Spin-1/2 chain We have investigated a simple model for the spin transport between two spin polarized reservoirs a configuration of considerable interest in spintronics. To do this we have studied the evolution of the initial state $\left| \uparrow \ldots \uparrow\downarrow \ldots \downarrow \right\rangle$ under the effect of nearest-neighbour interactions using the adaptive t-DMRG. For weak S^zS^z-interaction and arbitrary dimerization, we find that for long times the transport of the magnetization is ballistic, similar

to the case of the XX-model (no S^zS^z-interaction) [118]. This finding suggests that the ballistic transport for long times is not an artefact of the XX-model. For stronger S^zS^z-interaction, even in a homogeneous system a completely different result is obtained by the adaptive t-DMRG in the long-time evolution. The magnetization transport is no longer ballistic, but shows oscillatory behaviour around some constant value. We found that the change in the long time behaviour takes place abruptly at the phase transition between the (anti-) ferromagnetic phase and the critical phase. This drastic change can be attributed to the close resemblance of the initial state to the ground state of the ferromagnetic phase.

Error analysis Using the exact solution for the XX-model we performed a detailed error analysis for the adaptive t-DMRG. We find that the error introduced in the adaptive t-DMRG decomposes into the Suzuki-Trotter error and the truncation error, and can be controlled well by the size of the Suzuki-Trotter time-step and the number of states kept. Our error analysis using typical values for the Suzuki-Trotter time and the number of states further shows that for small times the error is dominated by the Suzuki-Trotter error whereas for long times the truncation error becomes the most important. We expect this finding to be general and to hold also for other models not exactly solvable.

Outlook In this thesis we showed the successful application of the adaptive t-DMRG to calculate the time-evolution of quantum states which are initially far from equilibrium focusing on equal time correlation functions. The generalization of the method to problems with explicitly time-dependent Hamiltonians and to correlations functions at different times [7] is straightforward. Thus the advantages of the adaptive t-DMRG can be exploited for a wide range of non-equilibrium phenomena and dynamical quantities like the dynamical structure factor can be calculated. This might in many cases be a more efficient way than for example using the 'dynamic DMRG' (see reference [4] and references therein).
So far we considered systems at zero-temperature, since in most situations mentioned here low enough temperatures can be reached in experiments. A generalization to the simulation of mixed states [125, 126, 127] is possible at the cost of introducing an auxiliary space. The method then becomes applicable to a large field of dissipative systems and non-dissipative systems at zero and finite temperature. Presently very little is known about the detailed performance of such generalizations, but early signs look promising. As shown by the applications in this thesis the adaptive t-DMRG can address a number of problems which could not be treated previously. We are confident that by some generalizations the method can be taken beyond the field of applications studied so far. Indeed it shows potential to address many interesting questions and problems in the areas of condensed matter and quantum optics systems, providing for mutual benefit and cross-fertilization to both area.

A. Higher order Suzuki-Trotter decompositions

To implement an nth-order Suzuki-Trotter decomposition into the adaptive t-DMRG algorithm is very easy and at hardly any algorithmic cost. A second order Suzuki-Trotter decomposition reads for example [41]

$$e^{-\mathrm{i}\hat{H}\mathrm{d}t} = e^{-\mathrm{i}\hat{H}_{odd}\mathrm{d}t/2} e^{-\mathrm{i}\hat{H}_{even}\mathrm{d}t} e^{-\mathrm{i}\hat{H}_{odd}\mathrm{d}t/2} + O\left((\mathrm{d}t)^3\right), \tag{A.0.0.1}$$

where all local Hamiltonians on odd and even bonds have been grouped into $\hat{H}_{odd}$ and $\hat{H}_{even}$, respectively. At first sight this seems to indicate that at each Suzuki-Trotter time step three (instead of two) moves ("sweeps") through the chain have to be carried out. However, in many applications at the end of most time steps, the Hamiltonian does not change, such that for almost all time steps, we can contract the second $e^{-\mathrm{i}\hat{H}_{odd}\mathrm{d}t/2}$ from the previous and the first $e^{-\mathrm{i}\hat{H}_{odd}\mathrm{d}t/2}$ from the current time step to a standard $e^{-\mathrm{i}\hat{H}_{odd}\mathrm{d}t}$ time step. Hence, we incur almost no algorithmic cost. This is also standard practice in Quantum Monte Carlo [128]; following Quantum Monte Carlo, second order Suzuki-Trotter evolution is set up as follows:

1. Start with a half-time step $e^{-\mathrm{i}\hat{H}_{odd}\mathrm{d}t/2}$.
2. Carry out successive time steps $e^{-\mathrm{i}\hat{H}_{even}\mathrm{d}t}$ and $e^{-\mathrm{i}\hat{H}_{odd}\mathrm{d}t}$.
3. At measuring times, measure expectation values before a $e^{-\mathrm{i}\hat{H}_{odd}\mathrm{d}t}$ time step, and again before a time step $e^{-\mathrm{i}\hat{H}_{even}\mathrm{d}t}$, and form the average of the two values as the outcome of the measurement.
4. At times when the Hamiltonian changes, do not contract two half-time steps into one time step.

In this way, additional algorithmic cost is only incurred at the (in many applications rare) times when the Hamiltonian changes while strongly reducing the Suzuki-Trotter decomposition error.
Even more precise is the fourth order Suzuki-Trotter decomposition [129, 130] (we skip the third order here since this is as costly as the fourth order):

$$e^{-\mathrm{i}\hat{H}\mathrm{d}t} \approx \prod_{j=1}^{3} e^{-\mathrm{i}a_j\hat{H}_{odd}\mathrm{d}t} e^{-\mathrm{i}b_j\hat{H}_{even}\mathrm{d}t} \prod_{j=3}^{1} e^{-\mathrm{i}a_j\hat{H}_{odd}\mathrm{d}t} e^{-\mathrm{i}b_j\hat{H}_{even}\mathrm{d}t} \tag{A.0.0.2}$$

with $a_1 = \frac{14-\sqrt{19}}{108}$, $a_2 = \frac{20-7\sqrt{19}}{108}$, $a_3 = (1-2a_1-2a_2)/2$, $b_1 = 2/5$, $b_2 = -1/10$, and $b_3 = (1-2b_1-2b_2)/2$. Therefore, eleven sweeps have to be performed

per Suzuki-Trotter time step, but since accuracy grows with the fourth power and not only quadratically as for the second order decomposition, the number of time steps, which have to be performed to reach the demanded accuracy, decreases considerably.

B. Ultracold atoms confined in optical lattices

In this appendix the principle by which optical lattices are generated is explained.

B.1. Interaction of neutral atoms with light fields

The interaction of neutral atoms with light fields consists of two parts, a conservative and a dissipative part [131]. The dissipative contribution is caused by the absorption of a photon by the atom and the subsequent spontaneous emissions. On this principle the widely used laser cooling is based. The other contribution which is used for the realization of optical lattices, stems from the fact that the light field induces a dipole moment in the atom which results in a shift of the energy levels, called the ac-Stark shift.

ac-Stark shift Let us assume that the light field couples only two levels of the atom, say $|g\rangle$ and $|e\rangle$. If these levels have different parity a dipole moment can be induced by an external light field $\mathbf{E}$, i.e. in general $\langle g|H_{\text{dip}}|e\rangle = \langle g|\mathbf{dE}|e\rangle \neq 0$, where $\mathbf{d} = -e\mathbf{r}$ is the dipole moment of the atom. This coupling between the light field and the atom can cause a shift in the energy spectrum of the system. In the following we derive this shift in the so called dressed atom picture in which the atom is coupled to a quantized light field, i.e. $H_{\text{light}} = \hbar\omega_L(a^\dagger a + \frac{1}{2})$. The system of the decoupled atom and light $H = H_{\text{atom}} + H_{\text{light}}$ is taken as a starting point and the atom-light interaction is considered as a perturbation which shifts the energy levels of the system. The energy levels of the decoupled atom-light system are depicted in Fig. (B.1). The bare levels of the atom are shifted by the energy quantum $\hbar\omega_L$ for each light quantum present. Only levels like $|g, n\rangle$ and $|e, n-1\rangle$ [ellipse in Fig. B.1] are coupled by the atom-light interaction. Here g corresponds to the first level and e to the second level of the bare atom and n labels the number of light quanta. The shift of these levels can be determined in second order perturbation theory and is simply given by

$$\Delta E_{+/-} = \pm\frac{\left|\langle e, n-1|d|g, n\rangle\right|^2}{\Delta}\left|E\right|^2. \tag{B.1.0.1}$$

The + and − label the two states $|g, n\rangle$ and $|e, n-1\rangle$, respectively. Δ denotes the energy difference between these two unperturbed states which is given by the detuning of the laser, i.e. $E_+ - E_- = n\hbar\omega_l + E_g - (n-1)\hbar\omega_l - E_e = \hbar\Delta$. Using that the laser intensity is given by $I(\mathbf{r}) = \frac{1}{2}\varepsilon_0 c\left|E(\mathbf{r})\right|^2$ and that the on-resonance damping rate Γ is related to the dipole matrix element by

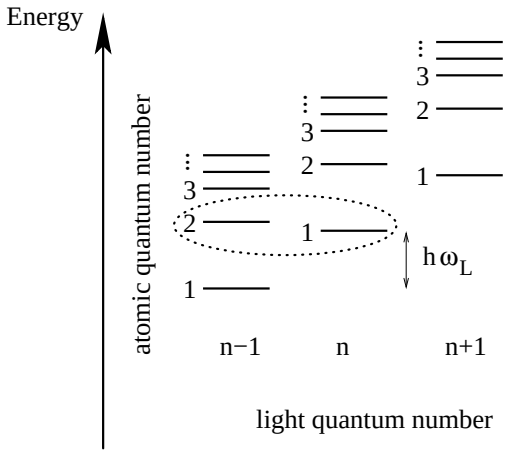

Figure B.1.: Energy levels for an atom and a quantized light field. The atomic levels are shifted by $\hbar\omega_L$ times the number of light quanta present. One level pair coupled by the atom-light interaction is indicated.

$\Gamma = \frac{\omega_0^3}{3\pi\varepsilon_0\hbar c^3}\left|\langle e, n-1|d|g, n\rangle\right|^2$, $\hbar\omega_0$ is the energy difference between the levels in question, the shift can be written as

$$\Delta E_{+/-}(\mathbf{r}) = \pm\frac{3\pi c^2}{2\omega_0^3}\frac{\Gamma}{\Delta}I(\mathbf{r}). \tag{B.1.0.2}$$

The resulting effective dipole potential acting on the atom, which is mainly in the ground state, is dominated by the light shift to the ground state energy, i.e. $V_{\mathrm{dip}}(\mathbf{r}) = \Delta E_+(\mathbf{r})$ and its magnitude is proportional to the intensity of the light field.

Multi-level atoms In the case of multi-level atoms like the experimentally widely used ^{87}Rb isotope transitions to all excited states should be taken into account. In particular in the case of ^{87}Rb the D_2 and D_1 line [47] should be considered. But if the laser detuning is large compared to the fine structure splitting and the polarization of the laser is linear, the effective dipole potential can again be approximated by the two level result with a detuning relative to the center of the D_2 and D_1 line.

B.2. Optical lattices

The proportionality of the effective dipole potential and the laser intensity can be used to create spatially varying potential landscapes. In the experiments [1, 50] simple cubic lattices were created by superimposing three standing waves orthogonal to each other. The laser beams used were far red detuned. Additionally to the periodic potential, in experiments the Gaussian intensity profile of the red-detuned lasers create a trapping potential. The effective dipole potential close to the trap center can be approximated as a contribution of the

periodic lattice potential and an additional external harmonic confinement:

$$V(\mathbf{r}) = V_{\text{lat}}(\mathbf{r}) + V_{\text{trap}}(\mathbf{r}) \quad \text{with} \tag{B.2.0.3}$$

$$V_{\text{lat}}(\mathbf{r}) \approx V_x \sin^2(kx) + V_y \sin^2(ky) + V_z \sin^2(kz) \quad \text{and} \tag{B.2.0.4}$$

$$V_{\text{trap}}(\mathbf{r}) \approx \frac{M}{2}(\omega_x^2 x^2 + \omega_y^2 y^2 + \omega_z^2 z^2). \tag{B.2.0.5}$$

Here M is the mass of the atoms, $V_{x,y,z}$ are the potential depths of the three superimposed standing waves. In the case of an isotropic lattice we denote it by V_0. The parameter $\omega_{x,y,z}$ are the effective trapping frequencies of the external harmonic confinement given by

$$\omega_x^2 = \frac{4}{M}\left(\frac{V_y}{\omega_y^2} + \frac{V_z}{\omega_z^2}\right) \quad \text{and cycl. perm. for} \quad \omega_{y,z}^2.$$

The period of the lattice is determined by the absolute value of the wave length λ and the wave vector k of the laser light by $a = \lambda/2 = \pi k$, respectively. In the experiments by Greiner et al. [1] the period of the optical lattice is approximately $a = \lambda/2 = (850/2)nm$. The height $V_{x,y,z}$ can experimentally be tuned very well by the intensity of the laser light. The potential depth of an optical lattice which is created by a far detuned laser can be evaluated by:

$$V_{x,y,z}/E_r = \frac{2M}{\hbar^2 k^2}\frac{3\pi c^2}{2\omega_0^3}\frac{2P\Gamma}{\Delta\pi w_0^2} \tag{B.2.0.6}$$

Here P is the total power of the laser light and $E_r = \hbar^2 k^2/2M$ the recoil energy.

B.3. Theoretical description of bosons in optical lattices

In this appendix the description of the ultracold bosons in an optical lattice by a lattice model, the Bose-Hubbard model is derived.

B.3.1. Influence of periodic structures

In the case of a periodic potential an energy band structure emerges. One way to determine this energy bands is to use Bloch's theorem which states that the eigenstates of the Hamiltonian $H_{periodic} = \frac{p^2}{2m} + V_{\text{lat}}(x)$ can be written as a product of a plane wave and a function with the lattice periodicity, $\phi_q^{(n)}(x) = \mathrm{e}^{\mathrm{i}qx} u_q^{(n)}(x)$, where $q = \frac{2\pi}{La} j$ with $j = -L/2, \ldots, 0, \ldots, L/2 - 1$ (L is the even number of the sites in the lattice) is called the quasi-momentum and is chosen to lie in the first Brillouin zone. The quantum number n counts the energy bands. The functions $u_q^{(n)}(x)$ are periodic functions with lattice period a and obey the equation

$$\left(\frac{1}{2m}(p + \hbar q)^2 + V_{\text{lat}}(x)\right) u_q^{(n)}(x) = E_q^{(n)} u_q^{(n)}(x). \tag{B.3.1.1}$$

The energy bands are now obtained solving these equations in the Fourier space. Examples for different energy structures are shown in Fig. B.2 for different heights of the lattice potential. If the lattice depth vanishes (Fig. B.2 (a)), the energy 'bands' correspond to the parabolic energy of free particles, if the lattice becomes deeper (Fig. B.2 (b)) band gaps open. For deep lattices the lowest band becomes flat and the width of the first band gap corresponds to the level spacing $\hbar\omega$ one would get assuming a harmonic potential $V \approx \frac{M}{2}\omega^2(x - x_j)^2$ at each lattice site. In contrast to the completely delocalized Bloch functions $\phi_q^{(n)}$ a set of wave functions which are maximally localized at the lattice sites x_j can be defined by

$$w_n(x - x_j) = \frac{1}{\sqrt{Z}} \sum_q \mathrm{e}^{\mathrm{i}qx_j} \phi_q^{(n)}(x). \tag{B.3.1.2}$$

Here Z is the normalization. These functions are called Wannier functions. Generally, the Wannier functions show the behaviour one expects for particles in the lattice in the sense that they become stronger localized as the lattice potential becomes deeper. Therefore, they offer an ideal tool for the discussion of phenomena in which the spatial localization in the periodic potential plays an important role.

B.3.2. Bose-Hubbard model

If the motion of the atoms is confined to the lowest energy band, it is favorable to work in the basis of Wannier functions w_0 of the lowest band neglecting higher bands. The bosonic field operators can be expanded in this basis:

$$\Psi(x) = \sum_j w_0(x - x_j) b_j, \tag{B.3.2.1}$$

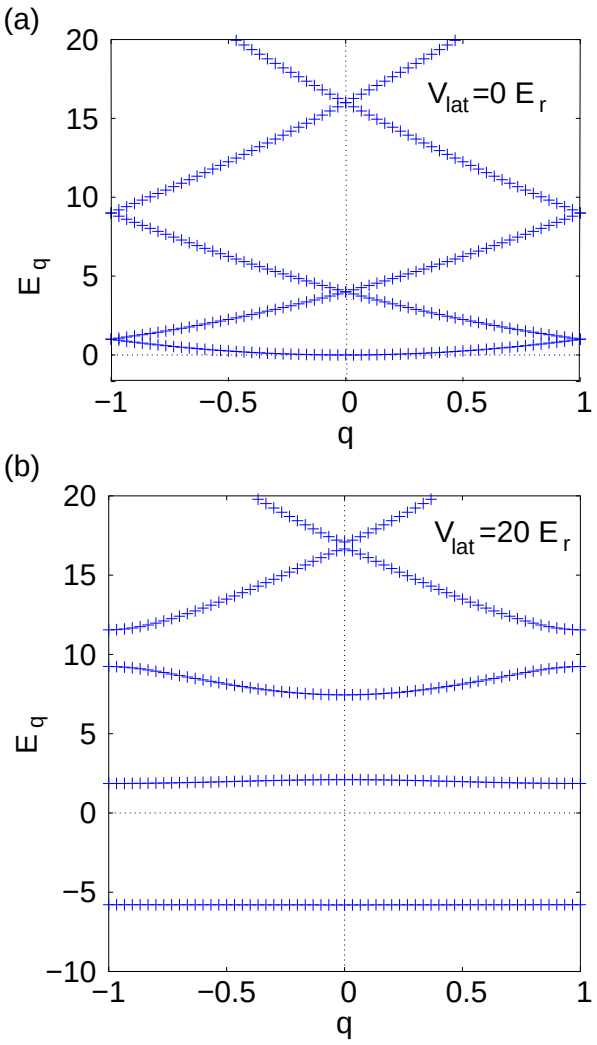

Figure B.2.: The different energy bands are shown without ($V_0 = 0$) and with ($V_0 = 20$) a lattice potential.

where b_j is the bosonic annihilation operator on site j. In the following the index 0 for the lowest band will be skipped. Inserting the expansion Eq. (B.3.2.1) into the Hamiltonian (3.2.0.1) one obtains the discrete lattice model:

$$
\begin{aligned}
(\text{B.3.2.2}) \quad H &= H_{\text{kin}} + H_{\text{int}} + H_{\text{pot}} \quad \text{with} \\
H_{\text{kin}} &= -\sum_{j,\tilde{j}} J_{\tilde{j},j} b_{\tilde{j}}^{\dagger} b_j, \quad H_{\text{int}} = \frac{1}{2} \sum_{\tilde{j},j,\tilde{l},l} U_{\tilde{j}j\tilde{l}l} b_{\tilde{j}}^{\dagger} b_j b_{\tilde{l}}^{\dagger} b_l, \quad \text{and} \\
H_{\text{pot}} &= \sum_j \varepsilon_j b_j^{\dagger} b_j.
\end{aligned}
$$

The coefficients are given by the expressions

$$\begin{aligned} J_{\tilde{j},j} &= \int \mathrm{d}^3x\, w^*(x-x_{\tilde{j}}) \left(\frac{-\hbar^2}{2M}\nabla^2 + V_{\mathrm{ext}}(x)\right) w(x-x_j) \quad \text{for} \quad j \neq \tilde{j} \\ \varepsilon_j &= -\int \mathrm{d}^3x\, w^*(x-x_j) \left(\frac{-\hbar^2}{2M}\nabla^2 + V_{\mathrm{ext}}(x)\right) w(x-x_j) \quad \text{and} \\ U_{\tilde{j}j\tilde{l}l} &= g\int \mathrm{d}^3x\, w^*(x-x_{\tilde{j}}) w^*(x-x_{\tilde{l}}) w(x-x_j) w(x-x_l) \end{aligned}$$

The main contribution to the kinetic energy is given by the terms with $\left|j-\tilde{j}\right| = 1$, whereas in the onsite interaction term the most important term is the term where all the creation and annihilation operators are taken on the same site (see below). Neglecting all other terms, the continuous Hamiltonian (3.2.0.1) reduces to the Bose-Hubbard Hamiltonian [46]:

$$H = -\sum_j J_j (b_j^\dagger b_{j+1} + h.c.) + \frac{1}{2}\sum_j U_j \hat{n}_j(\hat{n}_j - 1) + \sum_j \varepsilon_j \hat{n}_j, \tag{B.3.2.3}$$

where $b_j^\dagger$ and b_j are the bosonic creation and annihilation operators and $\hat{n}_j = b_j^\dagger b_j$ is the number operator on site j. This Hamiltonian is the simplest one describing the interplay between the kinetic energy (first term) and the on-site interaction of the atoms (second term). In the following we discuss the contribution of the different terms in more detail.

Trapping potential The contribution of the trapping potential can be approximated by

$$\int \mathrm{d}^3x\, w^*(x - x_{\tilde{j}}) V_{trap}(x) w(x - x_j) \simeq \delta_{\tilde{j},j} V_{trap}(x_j).$$

Here we used the fact that the trapping potential varies slowly compared to the periodicity of the system and that the Wannier functions are localized at the lattice sites and orthonormal.

Hopping coefficients The hopping elements can be related to the energy eigenvalues of the system. This can directly be seen expressing the Wannier functions by Bloch functions

$$\begin{aligned} J_{j'j} &= -\delta_{j'j} V_{trap(x_j)} + \frac{1}{Z} \int \mathrm{d}^3x \sum_{q,q'} \mathrm{e}^{\mathrm{i}qx_{j'}} \mathrm{e}^{-\mathrm{i}q'x_j} \phi_q^*(x) \left(\frac{p^2}{2m} + V_{\mathrm{ext}}(x) \right) \phi_{q'}(x) \\ &= -\frac{1}{Z} \sum_q \mathrm{e}^{\mathrm{i}q(x_{j'} - x_j)} E_q \end{aligned}$$

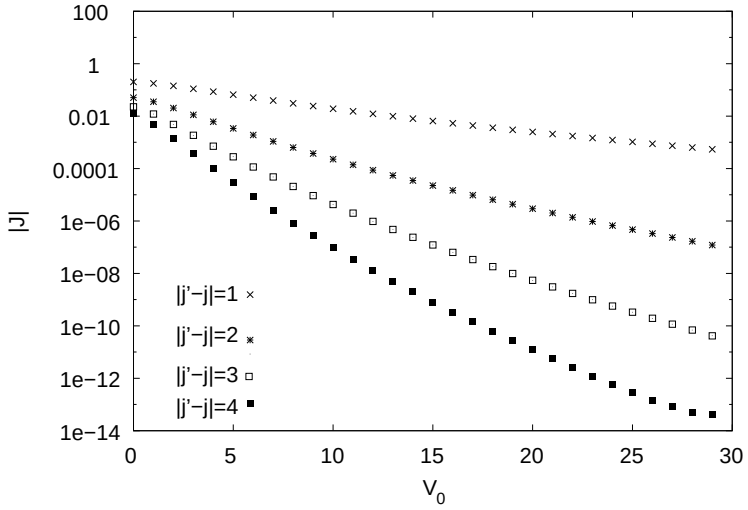

Figure B.3.: The dependence of the hopping elements J on the height of the lattice potential V_0 is shown for different distances $|j - j'|$ on a logarithmic scale.

In Fig. B.3 the dependence of the hopping elements on the height of the lattice potential is shown for different distances $|j' - j|$. The nearest-neighbour hopping element, i.e. $|j' - j| = 1$, is found to be an order of magnitude larger than the remaining except at very small lattice potentials. Therefore, only the nearest-neighbour hopping term is considered in the Hamiltonian (3.2.0.2) with $J_j := J_{j,j+1}$. For a homogeneous system and $V_0 \gg E_r$, an analytical approximation of the parameter J can be obtained from the asymptotic solutions of

the Mathieu equation [132] for the band gap

$$J/E_r = \frac{4}{\sqrt{\pi}} \left(\frac{V_0}{E_r}\right)^{\frac{3}{4}} \exp(-2\sqrt{V_0/E_r}) \tag{B.3.2.4}$$

The exact numerical solution is compared to this approximation in Fig. B.4.

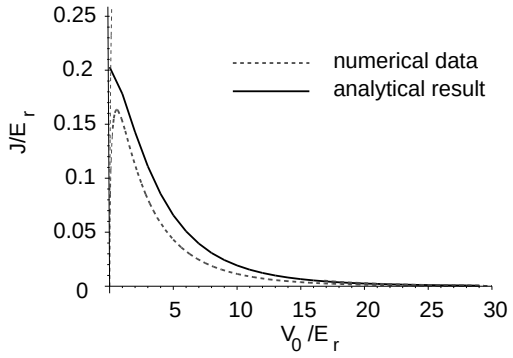

Figure B.4.: Comparison of numerical and analytical result for J.

Interaction terms For the interaction term the term in which all the creation and annihilation operators are taken on the same site is the most important, due to the localization of the Wannier functions at the lattice sites:

$$U_j \;:=\; U_{jjjj} = g \int \mathrm{d}^3x \, |w(x - x_j)|^4$$

The parameter U can be evaluated numerically. An analytical approximation is obtained, if the form of the Wannier functions is approximated by a Gaussian function. This can certainly not describe the decay of the Wannier functions at large x correctly, but gives a reasonable approximation for the interaction parameter U. The difference between both results is negligible if the dependence of the ratio U/J on the lattice height is considered, since J depends exponentially on the lattice height.

Bibliography

[1] M. Greiner, O. Mandel, T. Esslinger, T. Hänsch, and I. Bloch. Quantum phase transition from a superfluid to a Mott insulator in a gas of ultracold atoms. *Nature*, 415:39–44, 2002.

[2] S. R. White. Density matrix formulation for quantum renormalization groups. *Phys. Rev. Lett.*, 69:2863, 1992.

[3] I. Peschel, X. Wang, M. Kaulke, and K. Hallberg, editors. *Density-matrix Renormalization*. Springer, 1998.

[4] U. Schollwöck. The density-matrix renormalization-group. *cond-mat/0409292, Rev. Mod. Phys. (in press)*, 2005.

[5] G. Vidal. Efficient simulation of one-dimensional quantum many-body systems. *Phys. Rev. Lett.*, 93:040502, 2004.

[6] A. J. Daley, C. Kollath, U. Schollwöck, and G. Vidal. Time-dependent density-matrix renormalization-group using adaptive effective Hilbert spaces. *J. Stat. Mech.: Theor. Exp.* , P04005, 2004.

[7] S. R. White and A. E. Feiguin. Real time evolution using the density matrix renormalization group. *Phys. Rev. Lett.*, 93:076401, 2004.

[8] M. H. Anderson, J. R. Ensher, M. R. Matthews, C. E. Wieman, and E. A. Cornell. Observation of Bose-Einstein condensation in a dilute atomic vapor. *Science*, 269(0):198, 1995.

[9] K. B. Davis, M.-O. Mewes, M. A. Joffe, M. R. Andrews, and W. Ketterle. Evaporative cooling of sodium atoms. *Phys. Rev. Lett.*, 74:5202, 1995.

[10] C. C. Bradley, C. A. Sackett, J. J. Tollett, and R. G. Hulet. Evidence of Bose-Einstein condensation in an atomic gas with attractive interactions. *Phys. Rev. Lett.*, 75:1687, 1995.

[11] C. J. Pethick and H. Smith. *Bose-Einstein Condensation in Dilute Gases*. Cambridge University Press, 2002.

[12] L. P. Pitaevskii and S. Stringari. *Bose-Einstein Condensation*. Oxford University Press, 2003.

[13] S. L. Cornish, N. R. Claussen, J. L. Roberts, E. A. Cornell, and C. E. Wieman. Stable ^{85}Rb Bose-Einstein condensates with widely tunable interactions. *Phys. Rev. Lett.*, 85(9):1795, 2000.

[14] E. A. Donley, N. R. Claussen, S. L. Cornish, J. L. Roberts, E. A. Cornell, and C. E. Wieman. Dynamics of collapsing and expolding Bose-Einstein condensates. *Nature*, 412:295, 2001.

[15] C. Orzel, A. K. Tuchman, M. L. Fenselau, M. Yasuda, and M. A. Kasevich. Squeezed states in a Bose-Einstein condensate. *Science*, 291:2386, 2001.

[16] S. R. White. Density-matrix algorithms for quantum renormalization groups. *Phys. Rev. B*, 48:10345, 1993.

[17] M. A. Cazalilla and J. B. Marston. Time-dependent density-matrix renormalization-group: A systematic method for the study of quantum many-body systems out-of-equilibrium. *Phys. Rev. Lett.*, 88:256403, 2002.

[18] G. Vidal. Efficient classical simulation of slightly entangled quantum computations. *Phys. Rev. Lett.*, 91:147902, 2003.

[19] A. Klümper, A. Schadschneider, and J. Zittartz. Matrix-product ground states for one-dimensional spin-1 quantum antiferromagnets. *Europhys. Lett.*, 24:293, 1993.

[20] M. Fannes, B. Nachtergaele, and R. F. Werner. Finitely correlated states on quantum spin chains. *Comm. Math. Phys.*, 144:3, 1992.

[21] S. R. White. Spin gaps in a frustrated Heisenberg model for CaV_4O_9. *Phys. Rev. Lett.*, 77:3633, 1996.

[22] A. Kemper. *Transfermatrix-DMRG for dynamics of stochastic models and thermodynamics of fermionic models.* PhD thesis, Universität zu Köln, 2003.

[23] M. A. Nielsen and I. L. Chuang. *Quantum computation and quantum communication.* Cambridge University Press, 2000.

[24] T. J. Osborne and M. A. Nielsen. Entanglement, quantum phase transitions, and density matrix renormalization. *Quant. Inf. Proc.*, 1:45, 2002.

[25] C. M. Dawson and M. A. Nielsen. Frustration, interaction strength and ground-state entanglement in complex quantum systems. *Phys. Rev. A*, 69:052316, 2004.

[26] H. L. Haselgrove, M. A. Nielsen, and Osborne. Entanglement, correlations, and the energy gap in many-body quantum systems. *Phys. Rev. A*, 69:032303, 2004.

[27] G. Vidal, J. I. Latorre, E. Rico, and A. Kitaev. Entanglement in quantum critical phenomena. *Phys. Rev. Lett.*, 90:227902, 2003.

[28] J. Gaite. Entanglement entropy and the density matrix renormalization group. *quant-ph/0301120*, 2003.

[29] J. I. Latorre, E. Rico, and G. Vidal. Ground state entanglement in quantum spin chains. *Quant. Inf. and Comp.*, 4(1):048, 2003.

[30] C. H. Bennett and D. P. DiVincenzo. Quantum information and computation. *Nature*, 404:247, 2000.

[31] C. Lanczos. An iteration method for the solution of the eigenvalue problem of linear differential and integral operators. *J. Res. Natl. Bur. Stand.*, 45:225, 1950.

[32] E. R. Davidson. The iterative calculation of a few of the lowest eigenvalues and corresponding eigenvectors of large real-symmetric matrices. *J. Comput. Phys.*, 17:87, 1975.

[33] W. H. Press et al., editor. *Numerical Recipes in C: The Art of Scientific Computing*. Cambridge University Press, 1992.

[34] H. G. Luo, T. Xiang, and X. Q. Wang. Comment on "time-dependent density-matrix renormalization group: A systematic method for the study of quantum many-body out-of-equilibrium systems. *Phys. Rev. Lett.*, 91:049701, 2003.

[35] M. A. Cazalilla and J. B. Marston. Response to "comment on "time-dependent density-matrix renormalization-group: A systematic method for the study of quantum many-body systems out-of-equilibrium"". *Phys. Rev. Lett.*, 91:049702, 2003.

[36] S. Östlund and S. Rommer. Thermodynamic limit of density matrix renormalization. *Phys. Rev. Lett.*, 75:3537, 1995.

[37] J. Dukelsky, M. A. Martin-Delgado, T. Nishino, and G. Sierra. Equivalence of the variational matrix product method and the density matrix renormalization group. *Europhys. Lett.*, 43:457, 1998.

[38] I. Affleck, T. Kennedy, E. H. Lieb, and H. Tasaki. Rigorous results on valence-bond ground states in antiferromagnets. *Phys. Rev. Lett.*, 59:799, 1987.

[39] I. Affleck, T. Kennedy, E. H. Lieb, and H. Tasaki. Valence bond ground states in isotropic quantum antiferromagnets. *Comm. Math. Phys.*, 115:477, 1988.

[40] M. Fannes, B. Nachtergaele, and R. F. Werner. Exact antiferromagnetic ground states for quantum chains. *Europhys. Lett.*, 10:643, 1989.

[41] M. Suzuki. Relationship between d-dimensional quantal spin systems and (d+1)-dimensional Ising systems — equivalence, critical exponents and systematic approximants of the partition function and spin correlations —. *Prog. Theor. Phys.*, 56:1454, 1976.

[42] H. Takasaki, T. Hikihara, and T. Nishino. Fixed point of the finite system DMRG. *J. Phys. Soc. Jpn.*, 68:1537, 1999.

[43] F. Verstraete, J. J. Garcia-Ripoll, and I. Cirac. Matrix product density operators: Simulation of finite-T and dissipative systems. *Phys. Rev. Lett.*, 93:207204, 2004.

[44] M. R. Andrews, C. G. Townsend, H.-J. Miesner, D. S. Durfee, D. M. Kurn, and W. Ketterle. Observation of interference between two Bose condensates. *Science*, 275:637, 1997.

[45] F. S. Dalfovo. Theory of Bose-Einstein condensation in trapped gases. *Rev. Mod. Phys.*, 71:463, 1999.

[46] D. Jaksch, C. Bruder, I. Cirac, C. W. Gardiner, and P. Zoller. Cold bosonic atoms in optical lattices. *Phys. Rev. Lett.*, 81(15):3108, 1998.

[47] M. Greiner. *Ultracold quantum gases in three-dimensional optical lattice potentials*. PhD thesis, Ludwig-Maximilians-Universität München, 2003.

[48] R. Grimm, M. Weidemüller, and Y. B. Ovchinnikov. Optical dipole traps for neutral atoms. *Adv. At. Mol. Opt. Phys.*, 42:95, 2000.

[49] P. S. Jessen and I. H. Deutsch. Optical lattices. *Adv. At. Mol. Opt. Phys.*, 37, 1996.

[50] M. Köhl, H. Moritz, T. Stöferle, C. Schori, and T. Esslinger. Superfluid to Mott insulator transition in one, two and three dimensions. *J. of Low Temp. Phys.* , 138:635, 2005.

[51] W. Zwerger. Mott-Hubbard transition of cold atoms in optical lattices. *Journal of Optics B:*, 5:9, 2003.

[52] M. P. A. Fisher, P. B. Weichman, G. Grinstein, and D. S. Fisher. Boson localization and the superfluid-insulator transition. *Phys. Rev. B*, 40(1):546, 1989.

[53] B. Y. Chen, S. D. Mahanti, and M. Yussouff. Helium atoms in zeolite cages: Novel Mott-Hubbard and Bose-Hubbard system. *Phys. Rev. Lett.*, 75(3):473, 1995.

[54] M.-C. Cha, M. P. A. Fisher, S. M. Girvin, M. Wallin, and A. P. Young. Universal conductivity of two-dimensional films at the superconductor-insulator transition. *Phys. Rev. B*, 44:6883, 1991.

[55] M. P. A. Fisher. Quantum phase transitions in disordered two-dimensional superconductors. *Phys. Rev. Lett.*, 65(7):923, 1990.

[56] M. P. A. Fisher and G. Grinstein. Quantum critical phenomena in charged superconductors. *Phys. Rev. Lett.*, 60(3):208, 1988.

[57] M. P. A. Fisher, G. Grinstein, and S. M. Girvin. Presence of quantum diffusion in two dimensions: Universal resistance at the superconductor-insulator transition. *Phys. Rev. Lett.*, 64(5):587, 1990.

[58] H. Moritz, T. Stöferle, M. Köhl, and T. Esslinger. Exciting collective oscillations in a trapped 1d gas. *Phys. Rev. Lett.*, 91:250402, 2003.

[59] B. Paredes, A. Widera, V. Murg, O. Mandel, S. Fölling, I. Cirac, G. V. Shlyapnikov, T. W. Hänsch, and I. Bloch. Tonks-Girardeau gas of ultracold atoms in an optical lattice. *Nature*, 429:277, 2004.

[60] T. D. Kühner and H. Monien. Phases of the one-dimensional Bose-Hubbard model. *Phys. Rev. B*, 58(22):14741, 1998.

[61] G. G. Batrouni and R. T. Scalettar. World-line quantum monte carlo algorithm for a one-dimensional Bose model. *Phys. Rev. B*, 46(14):9051, 1992.

[62] J. K. Freericks and H. Monien. Phase diagram of the Bose-Hubbard model. *Europhys. Lett.*, 26(7):551–556, 1994.

[63] J. K. Freericks and H. Monien. Strong-coupling expansions for the pure and disordered Bose-Hubbard model. *Phys. Rev. B*, 53(5):2691, 1996.

[64] D. S. Rokhsar and B. G. Kotliar. Gutzwiller projection for bosons. *Phys. Rev. B*, 44(18):10328, 1991.

[65] J. J. Garcia-Ripoll, J. I. Cirac, P. Zoller, C. Kollath, U. Schollwöck, and J. von Delft. Variational ansatz for the superfluid Mott-insulator transition in optical lattices. *Optics Express*, 12(1):42, 2004.

[66] T. D. Kühner, S. R. White, and H. Monien. One-dimensional Bose-Hubbard model with nearest-neighbor interaction. *Phys. Rev. B*, 61(18):12474, 2000.

[67] C. Kollath, U. Schollwöck, J. von Delft, and W. Zwerger. Spatial correlations of trapped 1d bosons in an optical lattice. *Phys. Rev. A*, 69:031601, 2004.

[68] G. G. Batrouni, V. Rousseau, R. T. Scalettar, M. Rigol, A. Muramatsu, P. J. H. Denteneer, and M. Troyer. Mott domains of bosons confined on optical lattices. *Phys. Rev. Lett.*, 89(11):117203, 2002.

[69] N. Elstner and H. Monien. Dynamics and thermodynamics of the Bose-Hubbard model. *Phys. Rev. B*, 59:12184, 1999.

[70] F. D. M. Haldane. Effective harmonic-fluid approach to low-energy properties of one-dimensional quantum fluids. *Phys. Rev. Lett.*, 47:1840, 1981.

[71] D. Gangardt and G. V. Shlyapnikov. Stability and phase coherence of trapped 1d Bose gases. *Phys. Rev. Lett.*, 90(1):010401, 2003.

[72] A. Recati, P. O. Fedichev, W. Zwerger, and P. Zoller. Spin-charge separation in ultracold quantum gases. *Phys. Rev. Lett.*, 90:020401, 2003.

[73] V. Dunjko, V. Lorent, and M. Olshanii. Bosons in cigar-shaped traps: Thomas-Fermi regime, Tonks-Giradeau regime, and in between. *Phys. Rev. Lett.*, 86:5413, 2001.

[74] V. A. Kashurnikov, N. V. Prokof'ev, and B. V. Svistunov. Revealing superfluid-Mott-insulator transition in an optical lattice. *Phys. Rev. A*, 66(3):031601, 2002.

[75] W. Altman, A. Polkovnikov, E. Demler, B. Halperin, and M. D. Lukin. Superfluid-insulator transition in a moving system of interacting bosons. *cond-mat/0411047*, 2004.

[76] R. Roth and K. Burnett. Superfluidity and interference pattern of ultracold bosons in optical lattices. *Phys. Rev. A*, 67:031602, 2002.

[77] M. A. Cazalilla. Low-energy properties of a one-dimensional system of interacting bosons with boundaries. *Europhys. Lett.*, 59:793, 2002.

[78] G. Pupillo, E. Tiesinga, and C. J. Williams. Effects of inhomogeneity on the spectrum of the Mott-insulator state. *Phys. Rev. A*, 68:063604, 2003.

[79] M. Köhl, T. Stöferle, H. Moritz, C. Schori, and T. Esslinger. 1d Bose gases in an optical lattice. *Applied Physics B*, 79:1009, 2004.

[80] C. Kollath, U. Schollwöck, J. von Delft, and W. Zwerger. One-dimensional density waves of ultracold bosons in an optical lattice. *cond-mat/0411403, accepted in Phys. Rev. A*, 2005.

[81] M. R. Andrews, D. M. Kurn, H. J. Miesner, D. S. Durfee, C. G. Townsend, S. Inouye, and W. Ketterle. Propagation of sound in a Bose-Einstein condensate. *Phys. Rev. Lett.*, 79:553, 1997.

[82] M. R. Andrews, D. M. Stamper-Kurn, H.-J. Miesner, D. S. Durfee, C. G. Townsend, S. Inouye, and W. Ketterle. Erratum: Propagation of sound in a Bose-Einstein condensate. *Phys. Rev. Lett.*, 80:2967, 1998.

[83] S. Burger, K. Bongs, S. Dettmer, W. Ertmer, K. Sengstock, A. Sanpera, G. V. Shlyapnikov, and M. Lewenstein. Dark solitons in Bose-Einstein condensates. *Phys. Rev. Lett.*, 83:5198, 1999.

[84] J. Denschlag, J. E. Simsarian, D. L. Feder, C. W. Clark, L. A. Collins, J. Cubizolles, L. Deng, E. W. Hagley, K. Helmerson, W. P. Reinhardt, S. L. Rolston, B. I. Schneider, and W. D. Phillips. Generating solitons by phase engineering of a Bose-Einstein condensate. *Science*, 287:97, 2000.

[85] B. Damski. Formation of shock waves in a Bose-Einstein condensate. *Phys. Rev. A*, 69:043610, 2004.

[86] C. Menotti, M. Krämer, A. Smerzi, L. Pitaevskii, and S. Stringari. Propagation of sound in a Bose Einstein condensate in an optical lattice. *Phys. Rev. A*, 70:023609, 2004.

[87] D. Boers, C. Weiss, and M. Holthaus. Bogoliubov speed of sound for a dilute Bose-Einstein condensate in a 3d optical lattice. *Europhys. Lett.*, 67:887, 2004.

[88] A. Smerzi and A. Trombettoni. Nonlinear tight-binding approximation for Bose-Einstein condensates in a lattice. *Phys. Rev. A*, 68:023613, 2003.

[89] T. Stöferle, H. Moritz, C. Schori, M. Köhl, and T. Esslinger. Transition from a strongly interacting 1d superfluid to a Mott insulator. *Phys. Rev. Lett.*, 92:130403, 2004.

[90] T. Kinoshita, T. Wenger, and D. S. Weiss. Observation of a one-dimensional Tonks-Girardeau gas. *Science*, 305:1125, 2004.

[91] E. H. Lieb and W. Liniger. Exact analysis of an interacting Bose gas. I. the general solution and the ground state. *Phys. Rev.*, 130:1605, 1963.

[92] E. H. Lieb. Exact analysis of an interacting Bose gas. II. the excitation spectrum. *Phys. Rev.*, 130:1616, 1963.

[93] M. A. Cazalilla. One-dimensional optical lattices and impenetrable bosons. *Phys. Rev. A*, 67:053606, 2003.

[94] M. A. Cazalilla. Are the Tonks regimes in the continuum and on the lattice truly equivalent? *Phys. Rev. A*, 70:041604(R), 2004.

[95] A. D. Jackson and G. M. Kavoulakis. Lieb mode in a quasi-one dimensional Bose-Einstein condensate of atoms. *Phys. Rev. Lett.*, 89(7):070403, 2002.

[96] M. Ishikawa and H. Takayama. Solitons in a one-dimensional Bose system with the repulsive delta-function interaction. *J. Phys. Soc. Jap.*, 49:1242, 1980.

[97] N. G. Parker, N. P. Proukakis, C. F. Barenghi, and C. S. Adams. Dynamical instability of a dark soliton in a quasi-one-dimensional Bose-Einstein condensate perturbed by an optical lattice. *J. Phys. B: At. Mol. Opt. Phys.*, 37:S175, 2004.

[98] O. Zobay, S. Pötting, P. Meystre, and E. M. Wright. Creation of gap solitons in Bose-Einstein condensates. *Phys. Rev. A*, 59:643, 1999.

[99] I. Carusotto, D. Embriaco, and G. La Rocca. Nonlinear atom optics and bright-gap-soliton generation in finite optical lattices. *Phys. Rev. A*, 65:053611, 2002.

[100] L. Fallani, L. De Sarlo, J. E. Lye, M. Modugno, R. Saers, C. Fort, and M. Inguscio. Observation of dynamical instability for a Bose-Einstein condensate in a moving 1d optical lattice. *cond-mat/0404045*, 2004.

[101] J. Voit. One-dimensional Fermi liquids. *Rep. Prog. Phys.*, 58:977, 1995.

[102] T. Giamarchi. *Quantum Physics in One Dimension*. Oxford University Press, 2004.

[103] P. Segovia, D. Purdie, M. Hengsberger, and Y. Baer. Observation of spin and charge collective modes in one-dimensional metallic chains. *Nature*, 402:504, 1999.

[104] T. Lorenz, M. Hofmann, M. Grüninger, A. Freimuth, G. S. Uhrig, M. Dumm, and M. Dressel. Evidence for spin-charge separation in quasi-one-dimensional organic conductors. *Nature*, 418:614, 2002.

[105] M. Bockrath, D. H. Cobden, J. Lu, A. G. Rinzler, R. E. Smalley, L. Balents, and P. L. McEuen. Luttinger-liquid behaviour in carbon nanotubes. *Nature*, 397:598, 1999.

[106] O. M. Auslaender, H. Steinberg, A. Yacoby, Y. Tserkovnyak, B. I. Halperin, K. W. Baldwin, L. N. Pfeiffer, and K. W. West. Spin-charge separation and localization in one dimension. *Science*, 308:88, 2005.

[107] H. Moritz, T. Stöferle, K. Günter, M. Köhl, and T. Esslinger. Confinement induced molecules in a 1d Fermi gas. *cond-mat/0503202*, 2005.

[108] L. Kecke, H. Grabert, and W. Häusler. Charge and spin dynamics of interacting Fermions in a one dimensional harmonic trap. *cond-mat/0411480*, 2004.

[109] C. Kollath, U. Schollwöck, and W. Zwerger. Spin-charge separation in cold Fermi gases: a real time analysis. *cond-mat/0504299, submitted to Phys. Rev. Lett.*, 2005.

[110] E. H. Lieb and F. Y. Wu. Absence of Mott transition in an exact solution of the short-range, one-band model in one dimension. *Phys. Rev. Lett.*, 20(25):1445, 1968.

[111] H. Shiba. Magnetic susceptibility at zero temperature for the one-dimensional Hubbard model. *Phys. Rev. B*, 6(3):930, 1972.

[112] C. F. Coll. Excitation spectrum of the one-dimensional Hubbard model. *Phys. Rev. B*, 9(5):2150, 1974.

[113] H. J. Schulz. Correlation exponents and the metal-insulator transition in the one-dimensional Hubbard model. *Phys. Rev. Lett.*, 64(23):2831, 1990.

[114] H. J. Schulz. Fermi liquids and non–Fermi liquids. In E. Akkermans, editor, *Mesoscopic Quantum Physics*, volume LXI of *Les Houches*. Elsevier (Amsterdam), 1995.

[115] M. Rigol and A. Muramatsu. Fermionization in an expanding 1d gas o hard-core bosons. *Opt. Commun.* , 243:33, 2004.

[116] C. A. Regal and D. S. Jin. Measurement of positive and negatice scattering lengths in a Fermi gas of atoms. *Phys. Rev. Lett.*, 90(23):230404, 2003.

[117] D. Gobert, C. Kollath, U. Schollwöck, and G. Schütz. Real-time dynamics in spin-1/2 chains with adaptive time-dependent DMRG. *Phys. Rev. E*, 71:036102, 2005.

[118] T. Antal, Z. Racz, A. Rakos, and G. Schütz. Transport in the XX chain at zero temperature: Emergence of flat magnetization profiles. *Phys. Rev. E*, 59:4912, 1999.

[119] G. O. Berim, S. Berim, and G. G. Cabrera. Long-time tails and anomalous slowing down in the relaxation of spatially inhomogeneous excitations in quantum spin chains. *Phys. Rev. B*, 66:094401, 2001.

[120] H. J. Mikeska and A. Kolezhuk. One-dimensional magnetism. In U. Schollwöck, J. Richter, D. Farnell, and R. Bishop, editors, *Quantum magnetism*, volume 645, page 1. Springer, Lecture notes in Physics, 2004.

[121] G. Schütz. Berry's phase in a one-dimensional quantum many-body system. *Phys. Rev. E*, 49:2461, 1994.

[122] E. Lieb, T. Schultz, and D. Mattis. Antiferromagnetic chain. *Ann. Phys.*, 16:407, 1961.

[123] H. J. Mikeska, S. Miyashita, and G. H. Ristow. $s = \frac{1}{2}$ magnetic chains as domain wall systems. *J. Phys.: Condens. Matter*, 3:2985, 1991.

[124] V. Hunyadi, Z. Racz, and L. Sasvari. Dynamic scaling of fronts in the quantum XX chain. *Phys. Rev. E*, 69:066103, 2004.

[125] U. Schollwöck. Time-dependent density-matrix renormalization-group methods. *cond-mat/0502470*, 2005.

[126] F. Verstraete, M. Popp, and J. I. Cirac. Entanglement versus correlations in spin systems. *Phys. Rev. Lett.*, 92:027901, 2004.

[127] M. Zwolak and G. Vidal. Mixed-state dynamics in one-dimensional quantum lattice systems: a time-dependent superoperator renormalization algorithm. *Phys. Rev. Lett.*, 93:207205, 2004.

[128] F. F. Assaad and D. Würtz. Charge and spin structures in the one-dimensional $t - j$ model. *Phys. Rev. B*, 44:2681, 1991.

[129] H. Yoshida. Construction of higher order symplectic integrators. *Phys. Lett. A*, 150:262, 1990.

[130] M. Krech, A. Bunker, and D. P. Landau. Fast spin dynamics algorithms for classical spin systems. *Comp. Phys. Comm.*, 111:1, 1998.

[131] H. J. Metcalf and P. van der Straten. *Laser Cooling and Trapping.* Springer Verlag (Heidelberg), 1999.

[132] M. Abramowitz, I. A. Stegun, and F. Loesch. *Handbook of mathematical functions.* McGraw-Hill (USA), Teubner Germany, 1960.

Acknowledgement

First of all I would like to thank U. Schollwöck and J. von Delft for their support, for the many frank and fruitful discussions, and for their helpful suggestions.
During the past three years I have discussed on many occasions parts of this work. While it is practically impossible to list all persons I am grateful to, I would like to mention in particular:
W. Zwerger for the clarifying discussions not only about quantum optical systems, but as well on tutorial sheets in electrodynamics and thermodynamics,
W. Hofstetter for agreeing to be the co-corrector of this work and helpful discussions on quantum optical systems,
S. Fölling, A. Widera, O. Mandel, and in particular to I. Bloch and M. Greiner for showing me the experimentalists view of the fascinating playground of ultracold atoms and for their optimism about the experimental realization of theoretical proposals,
T. Esslinger, T. Stöferle, H. Moritz, M. Köhl, K. Günther for many exciting discussions, their criticism and proposals for the experimental realization of the spin-charge separation in fermionic systems,
D. Gobert for many fruitful discussions, the good collaboration, but in particular for easing my start in München, der Landeshauptstadt Bayerns,
M. Cazalilla por las discusiones y por darme la posibilidad de trabajar un mes en la DIPC en San Sebastián,
T. Giamarchi for his support, his helpful models and pictures, and for showing me that physics is magic,
G. Schütz for many helpful discussions on the dynamics of spin systems and the good collaboration,
J.J. Garcia-Ripoll, A. J. Daley, G. Vidal, I. Cirac and P. Zoller for the good collaboration on the field of quantum optics and quantum information,
E. Altman, E. Demler, M. Troyer, H.-J. Mikeska, A. Rakos, Z. Rácz, and C. Tozzo for discussions about different parts of this thesis,
my colleagues and friends in Munich and Aachen for discussions, proofreading, computer support, and contributing to the delightful working atmosphere: A. Friedrich, S. Kleff, T. Korb, I. McCulloch, R. Dahlke, T. Barthel, M. Chung, S. Bergvist, R. Helmes, M. Sindel, U. Hartmann, M. Storcz, L. Borda, F. Wilhelm, H. Gutmann, and the group of H. Schöller in Aachen,
Studienstiftung des Deutschen Volkes and DFG grant DE 730/3-1 for financial support.
Last but not least I would like to praise my family and my friends, in particular Stephi, who diverted and supported me and who waited patiently when I was 'too busy'.

List of publications related to the thesis

- *Spin-charge separation in cold Fermi-gases: a real time analysis*
  C. Kollath, U. Schollwöck, and W. Zwerger
  submitted to Phys. Rev. Lett., cond-mat/0504299

- *One-dimensional density waves of ultracold bosons in an optical lattice*
  C. Kollath, U. Schollwöck, J. von Delft, and W. Zwerger
  accepted by Phys. Rev. A, cond-mat/0411403

- *Real-time dynamics in spin-1/2 chains with adaptive time-dependent DMRG*
  D. Gobert, C. Kollath, U. Schollwöck, and G. Schütz,
  Phys. Rev. E 71, 036102 (2005)

- *Time-dependent density-matrix renormalization-group using adaptive effective Hilbert spaces*
  A. J. Daley, C. Kollath, U. Schollwöck and G. Vidal
  J. Stat. Mech.: Theor. Exp. (2004) P04005

- *Spatial correlations of trapped 1d bosons in an optical lattice*
  C. Kollath, U. Schollwöck, J. von Delft,
  and W. Zwerger
  Phys. Rev. A 69 (Rapids), 031601 (2004)
  cond-mat/0310388

- *Variational ansatz for the superfluid Mott-insulator transition in optical lattices*
  Juan Jose Garcia-Ripoll, J. I. Cirac, P. Zoller,
  C. Kollath, U. Schollwöck, and J. von Delft
  Optics Express, Vol. 12, No. 1 - January 12, 2004, p. 42
  http://www.opticsexpress.org
  cond-mat/0306162

Curriculum vitae

Corinna Susan Kollath

Institute for Theoretical Physics C
RWTH Aachen
52056 Aachen
Germany

Higher Education

since	PhD student, RWTH Aachen
Oct. 2004	Prof. U. Schollwöck and Prof. J. von Delft (University of Munich)
2002-2004	PhD student, University of Munich Prof. U. Schollwöck and Prof. J. von Delft
2001	diploma thesis *'Quasiparticles in p-wave superconductors'* in the group of Prof. M. Zirnbauer (University of Cologne)
1998-2001	studies of physics with additional subject biology University of Cologne
1997/1998	studies of physics and mathematics University of Glasgow
1995-1997	studies of physics, mathematics, and biology University of Cologne
July 1995	Abitur, Gymnasium Erftstadt-Lechenich

University Degrees

July 2001	diploma in physics with additional subject biology University of Cologne
June 1998	B.Sc. Honours in Mathematics and Physics University of Glasgow
Aug. 1997	'Vordiplom' (intermediate degree) in physics University of Cologne
Aug. 1997	'Vordiplom' (intermediate degree) in mathematics University of Cologne

Research stays

23. Feb. -	University of Geneva
6. March 2004	Collaboration with Professor T. Giamarchi Geneva (Switzerland)
4. Nov. -	DIPC (Donostia International Physics Center)
1. Dec. 2003	Collaboration with PhD M. Cazalilla San Sebastian (Spain)

Scholarships

since 2002	scholarship for PhD studies of the 'Studienstiftung des deutschen Volkes' (German National Scholarship Foundation)
1997/98	scholarship of the DAAD (German Academic Exchange Service)
1997-2001	scholarship for undergraduate studies of the 'Studienstiftung des deutschen Volkes' (German National Scholarship Foundation)